



HAL
open science

Electrical excitation of surface plasmon polaritons by inelastic tunneling electrons with resonant nanoantennas

Cheng Zhang

► **To cite this version:**

Cheng Zhang. Electrical excitation of surface plasmon polaritons by inelastic tunneling electrons with resonant nanoantennas. Optics [physics.optics]. Université Paris Saclay (COMUE), 2019. English. NNT : 2019SACLO007 . tel-02296868

HAL Id: tel-02296868

<https://pastel.hal.science/tel-02296868>

Submitted on 25 Sep 2019

HAL is a multi-disciplinary open access archive for the deposit and dissemination of scientific research documents, whether they are published or not. The documents may come from teaching and research institutions in France or abroad, or from public or private research centers.

L'archive ouverte pluridisciplinaire **HAL**, est destinée au dépôt et à la diffusion de documents scientifiques de niveau recherche, publiés ou non, émanant des établissements d'enseignement et de recherche français ou étrangers, des laboratoires publics ou privés.

Electrical Excitation of Surface Plasmon Polaritons by Inelastic Tunneling Electrons with Resonant Nanoantennas

Thèse de doctorat de l'Université Paris-Saclay
préparée à Institut d'Optique Graduate School

École doctorale n°572 Ondes et matières
Spécialité de doctorat: physique

Thèse présentée et soutenue à Palaiseau, le 24 Mai, par

Cheng ZHANG (张铖)

Composition du Jury :

Mathieu KOCIAK Directeur de recherche, Université Paris-Sud	Président
Guillaume SCHULL Chargé de recherche, Université de Strasbourg	Rapporteur
Alexandre BOUHELIER Directeur de recherche, Université de Bourgogne	Rapporteur
Elizabeth BOER-DUCHEMIN Maitre de Conférences, Université Paris-Sud	Examineur
Yannick DE WILDE Directeur de recherche, Ecole Supérieure de Physique et de Chimie Industrielles	Examineur
Christophe SAUVAN Chargé de recherche, Institut d'Optique Graduate School	Invité
Jean-Jacques GREFFET Professeur, Institut d'Optique Graduate School	Directeur de thèse





Acknowledgements

It is the right time to express my gratitude for those whom I had met for the past three years and half.

I should first thank my dear supervisor: professor Jean-Jacques Greffet. I am greatly appreciated for joining your group as a PhD student. Thank you for sharing me your brilliant ideas and the useful guidelines for my research. I am so lucky to have a chance to work with you and I really appreciate your great patience to me when sometimes I had a small progress. Another aspect I appreciate a lot is your availability, your door is always open for any discussions about my questions. Thank you so much for your tremendous help!

I would like to thank Dr. Christophe Sauvan. Thank you very much for delivering me a lot of rigorous theoretical and numerical inputs during my PhD. I greatly enjoy the discussions with you. Thank you also for your encouragements once I met some problems. Without your suggestions, I wouldn't pass through the difficulties.

Dr. Anne-lise is the next colleague that I would like to thank. Thank you for introducing me to involve the fabrication for the project and thank you for sharing me your own experiences to stimulate me to work constantly in cleanroom. Without your advices, I wouldn't learn that much from the device fabrications.

I would like to thank professor François Marquier. Thank you for giving me a lot experimental cues during the last year of PhD. It is your working passion that inspires me a lot!

I would like to give my specific thanks to Dr. Jean-Paul Hugonin. Thank you for providing me to use your magical 'reticolo' to acquire all the numerical results I need. Apart from that, I really appreciate your working efficiency!

I would like to thank the jury committee for having agreed to comment my thesis. Thank you Dr. Mathieu Kociak, Dr. Alexandre Bouhelier, Dr. Guillaume Schull, Dr. Yannick De Wilde, and Dr. Elizabeth Boer-Duchemin to be my jury members.

I would like to thank the nice people I met during the working period in the cleanroom of C2N. Thank you Jean-Rene Coudeville, Nathalie Isac, David Bouville, Antoine Martin, Abdelhanin Aassime and Fabien Bayle. Thank you for guiding me the useful techniques to fabricate my devices.

I would like to thank the research group members, even the members have changed a lot since I came to France. Thank you Henri Benisty, Philippe Ben-Abdallah, Mondher Besbes, Riccardo Messina, Marie-Christine Dheur, Nick Schilder, Cédric Blanchard, Ioana Doyen, Ivan Latella, Emilie Sakat, Benjamin Vest, Ilan Shlesinger, Léo Wojszwyk, Anton Ovcharenko, Hector Monin, Marta Reina. I enjoy and appreciate all the happy moments with you guys either scientific or daily routine!

Apart from the research block, I would like also to thank the people I met outside the lab. 感谢在 C2N 认识的小伙伴们，是你们的鼓励让枯燥的加工岁月变得有趣很多。感谢范玉龙博士、王红月博士、管楠博士、陆璐博士，祝你们都有一个美好前程！感谢贾攀博士在学术和生活上的关照帮助，祝你未来的科研生涯一帆风顺！感谢有缘同住 Fresnes 的邻居们，感谢三年以来的快乐时光。感谢姚依含、朱永雪、黄碧君、周绮泳、伟胜及其家属！

最后的感谢留给了我的家人。虽然纵隔上万公里，但每时每刻都有着千丝万缕的牵挂。感谢这个信息发达的时代让地球两端的距离显得如此的触手可及。每一通电话每一次视频都镌刻着父母的谆谆教诲。没有您们的精神支持，孩儿断然是没法完成学业的。父母在不远游，惟愿早日归国完成一个不孝游子应尽的孝道。在这里遥祝二老身体健康，心想事成！

11/03/2019
@ Palaiseau
Cheng Zhang



Content

Abstract.....	11
Chapter 1	12
Metal-insulator-metal (MIM) tunnel junction as a light source	12
1.1. Introduction	12
1.2. MIM tunnel junction.....	13
1.3. Light and surface plasmon polaritons emission in a MIM tunnel junction	14
1.3.1. Surface plasmon polaritons (SPPs).....	14
1.3.2. Inelastic tunneling and elastic tunneling.....	16
1.3.3. Current fluctuation and electric field inside the barrier of a tunnel junction	18
1.3.4. STM-based tunnel junction.....	19
1.3.5. Integrated tunnel junction.....	19
1.4. Optical antenna assisted light emitting tunnel junction (LETJ).....	21
1.4.1. Plasmonic nanoantenna	21
1.4.2. Enhanced LETJ with aid of an optical antenna	24
1.5. Conclusion.....	25
Chapter 2	28
Theoretical description of light emission by a tunnel junction in presence of a resonant nanoantenna	28
2.1. Introduction	28
2.2. Light emission by inelastic tunneling: the fluctuating current radiation approach.....	28
2.3. Light emission by inelastic tunneling: the Fermi golden rule approach	33
2.4. Discussion and conclusion.....	35
Chapter 3	38
Enhanced SPP generation in the STM configuration	38
3.1. Introduction	38
3.2. Model of the SPP generation in the STM configuration	39
3.2.1. Model of light emission by IET: effective dipole source	39
3.2.2. Generation of propagating surface plasmon	40
3.3. Enhanced SPP generation with aid of a single optical antenna.....	42
3.3.1. Cylindrical antenna	42
3.3.2. Nanocone antenna	45
3.4. Conclusion.....	47
Chapter 4	49

Design of a highly efficient SPP source based on a cylindrical nanopatch antenna	49
4.1. Introduction	49
4.2. Mode hybridization and quasi-normal mode formalism	50
4.2.1. Mode hybridization	50
4.2.2. Modal formalism for the SPP emission	52
4.2.2.1. SPP emission with a single-mode antenna	53
4.2.2.2. SPP emission with a bimode antenna	55
4.3. Calculation of the nanopatch modes and their characteristics	56
4.4. Increasing the SPP emission by tuning the refractive index of the environment	59
4.5. Source position dependent SPP generation	61
4.6. Conclusion	62
Appendix: Antenna geometry dependent mode hybridization	64
Chapter 5	69
Fabrication of a nanoantenna MIM tunnel junction	69
5.1. Introduction	69
5.2. Strip antenna MIM tunnel junction	70
5.2.1. Substrate preparation	70
5.2.2. Al bottom electrode fabrication	71
5.2.3. Al film deposition and thermal oxidation treatment	72
5.2.4. Au strip antenna (top electrode) fabrication	74
5.2.5. Au connection pads fabrication	78
5.2.6. Wire-bonding	79
5.3. Cylindrical antenna MIM junction	80
5.3.1. Planarization	81
5.3.2. ITO deposition	87
5.4. Conclusion	90
Chapter 6	92
SPP emission by inelastic tunneling with a resonant antenna	92
6.1. Introduction	92
6.2. Experiment setup	93
6.3. Electrical characteristic	95
6.4. SPP emission characterization	97
6.5. Discussion and conclusion	101
Chapter 7	106
Conclusion and outlook	106
7.1. Conclusion	106
7.2. Outlook	107

Résumé106

References113

Abstract

Surface plasmon polaritons (SPPs) plays a central role in nanophotonics because they are optical modes that can be confined in space at the 10 nm scale and in time at the 10 fs scale. Electrical excitation of surface plasmon polaritons by inelastic tunneling electrons has the potential to be fast and localized so that it offers the opportunity to develop a nanosource for on-chip nanophotonics taking advantage of the full potential of surface plasmons polaritons. However, inelastic tunneling is rather inefficient with a typical electron-to-plasmon conversion efficiency of $10^{-7}\sim 10^{-5}$. In this thesis manuscript, we present a study for enhancing surface plasmon emission by inelastic tunneling electrons with a resonant nanoantenna. It consists of theoretical and experimental investigations. First, we have developed a theoretical model to describe the light emission from a tunnel junction based on the fluctuation-dissipation theorem. Second, we have theoretically demonstrated two strategies to improve the antenna SPP efficiency thus aiming to enhance electron-to-plasmon conversion efficiency. We introduce a resonant antenna mode with a sub-nanometer gap in order to enhance the coupling between the inelastic current and the the mode. Furthermore, we introduce the hybridization in a nanopatch antenna between a gap mode and an antenna mode to launch SPPs: we theoretically predict that 30% of the power emitted by a dipole is converted into SPP (working wavelength at 800nm) with a 1nm gap thickness. Third, we have developed the fabrication procedures to realize antenna tunnel junctions based on the Al/AlOx/Au configuration. The fabricated antenna junction shows a robust functionality both regarding electrical and optical properties. The antenna junction is demonstrated to control the SPP emission spectrum, the SPP emission polarization and enhance the SPP emission efficiency by over 3 orders of magnitude. The total SPP power emitted is in the range of 10 pW, four orders of magnitude larger than the typical fW power emitted by a scanning tunneling tip junction.

Chapter 1

Metal-insulator-metal (MIM) tunnel junction as a light source

- 1.1. Introduction
- 1.2. MIM tunnel junction
- 1.3. Light and surface plasmon polaritons emission in a MIM tunnel junction
 - 1.3.1. Surface plasmon polaritons (SPPs)
 - 1.3.2. Inelastic tunneling and elastic tunneling
 - 1.3.3. Current fluctuation and electric field inside the barrier of a tunnel junction
 - 1.3.4. STM-based tunnel junction
 - 1.3.5. Integrated tunnel junction
- 1.4. An optical nanoantenna assisted light emitting tunnel junction (LETJ)
 - 1.4.1. Plasmonic nanoantenna
 - 1.4.2. Enhanced LETJ with aid of an optical antenna
- 1.5. Conclusion

1.1. Introduction

The light emission from a metal-insulator-metal tunneling junction has been investigated for a few decades. The story started in 1976, when Lambe and McCarthy demonstrated a method for the generation of broadband light source in a planar metal-insulator-metal (MIM) tunnel junction[1]. In their observation, they found a high-frequency cutoff in the emission spectrum given by eV/h where V is the applied DC voltage. A simple inelastic electron tunneling model had been employed to interpret this phenomenon. In the following decade, light emission by inelastic tunneling was observed in Scanning Tunneling Microscopy (STM) when applying large voltages[2]. Because the response time of light emission is defined by the electron tunneling time through a tunnel barrier, this process can be potentially used as a ultrafast nanosource. In the last decade, by taking advantage of advanced nanotechnology, tunnel junctions have been combined with optical nanoantennas, in order to deal with the issue of low electron-to-photon conversion efficiency (typically $10^{-7}\sim 10^{-5}$). In this chapter, we are going to review the development of

light emission by inelastic tunneling. Accompanied with the knowledge of optical antenna, it allows us to step into the development of a nanoantenna MIM tunnel junction.

1.2. MIM tunnel junction

MIM tunnel junction is an important building blocks for microelectronics and optoelectronics applications. A typical MIM junction can be formed with two piece of conducting layers which has a thin insulating layer in between. Schematically show in Fig. 1.1, a bottom metallic electrode can be deposited by evaporation on a substrate. Then, an ultrathin dielectric layer (for instance, aluminum oxide or silicon oxide) would be fabricated on the bottom electrode via oxidation[3-5], ALD (atomic layer deposition)[6] or 2D monocrystalline monolayers exfoliation[7] . Subsequently, a top metallic electrode is deposited on the barrier layer to finalize the tunnel junction. In terms of tunneling concept, by following quantum mechanics, the electrons in one of the electrodes have a finite probability to tunnel through the barrier to the electrode on the other side, thus enabling conduction. When no voltage is applied between two electrodes, electrons are exchanged across the barrier until the Fermi levels of the electrodes reach the same value. Once a bias voltage is applied, a current can flow. The current can vary drastically depending on the biased voltage, material and the dimension of the tunnel barrier. At this point, the performance of MIM tunnel junction depends critically on the quality of the insulating tunnel barrier[8].

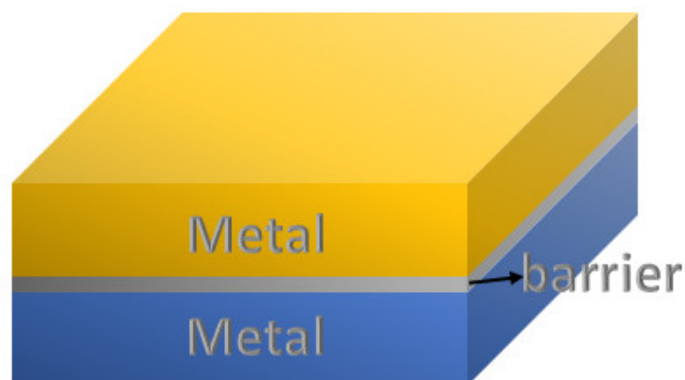


Figure 1.1 Schematic of a MIM tunnel junction

1.3. Light and surface plasmon polaritons emission in a MIM tunnel junction

1.3.1. Surface plasmon polaritons (SPPs)

Surface plasmon are coherent delocalized electron oscillations that exist at the interface between metal and dielectric. The charge motion of a surface plasmon always creates electromagnetic fields both outside and inside the metal. In a planar interface, it is called a propagating surface plasmon polariton; and in the closed surface of a nanoparticle, it is called a localized surface plasmon. As shown in Fig. 1.2, we see a schematic graph of a one-dimensional SPPs. Starting from Maxwell equations and using the continuity of the normal and transversal field components on the metal/dielectric interface, one can show that there is no transverse-electric mode[9]. While instead we have a transverse-magnetic mode for field which propagate along the x direction. Consequently, \mathbf{E}_m , \mathbf{H}_m and \mathbf{E}_d , \mathbf{H}_d represent the TM electromagnetic field in the metal and dielectric, respectively.

$$\begin{cases} \mathbf{E}_m = (E_{m,x}, 0, E_{m,z})e^{i(\mathbf{k}_m \mathbf{r} - i\omega t)}; \mathbf{H}_m = (0, H_{m,y}, 0)e^{i(\mathbf{k}_m \mathbf{r} - i\omega t)} \\ \mathbf{E}_d = (E_{d,x}, 0, E_{d,z})e^{i(\mathbf{k}_d \mathbf{r} - i\omega t)}; \mathbf{H}_d = (0, H_{d,y}, 0)e^{i(\mathbf{k}_d \mathbf{r} - i\omega t)} \end{cases} \quad (1-1)$$

The wavevector is denoted $\mathbf{k} = (k_x, 0, k_z)$.

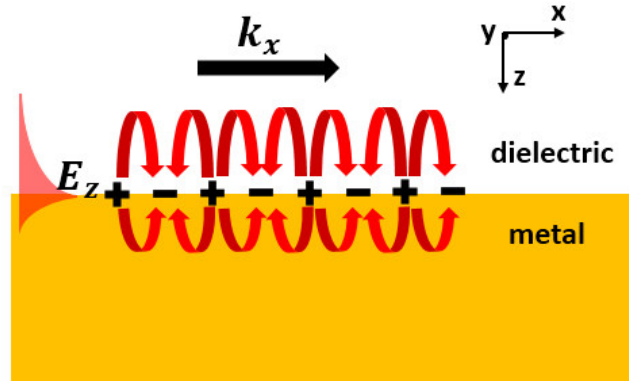


Figure 1.2. Composed character of a SPP at an interface of dielectric and metal.

Using $\nabla \cdot \mathbf{E} = 0$ and the continuity of E_x and ε_z , we find:

$$\frac{k_{m,z}}{\varepsilon_m} = -\frac{k_{d,z}}{\varepsilon_d}. \quad (1-2)$$

To ensure a bound mode at the interface, $k_{m,z}$ and $k_{d,z}$ should be imaginary. Thus, the fields decay exponentially into the respective half spaces, as symbolized in Fig. 1.2. In a word, SPP is describing an electromagnetic wave in the dielectric medium and oscillating electron plasma in the metal, where both modes have an exponentially evanescent character.

To obtain the dispersion relation of the propagating SPP. We simply derive the wave vector from the dispersion relation $k^2 = \varepsilon\omega^2/c^2$:

$$\begin{aligned} k_{m,z}^2 &= k_0^2 \varepsilon_m - k_x^2 \\ k_{d,z}^2 &= k_0^2 \varepsilon_d - k_x^2 \end{aligned} \quad (1-3)$$

where $k_0 = \omega/c$, is the vacuum wave vector of light. Inserting Eq.(1-3) into Eq.(1-2), we get the propagation constant:

$$k_x = \frac{\omega}{c} \sqrt{\frac{\varepsilon_m \varepsilon_d}{\varepsilon_m + \varepsilon_d}}. \quad (1-4)$$

Let us take an example of propagating surface plasmon at air/metal (based on an assumption of lossless Drude model, where $\varepsilon(\omega) = 1 - \omega_p^2/\omega^2$) interface, see the dispersion curve in Fig. 1.3. The red line represents the light cone in the air, and the SPP dispersion relation completely resides below the light cone.

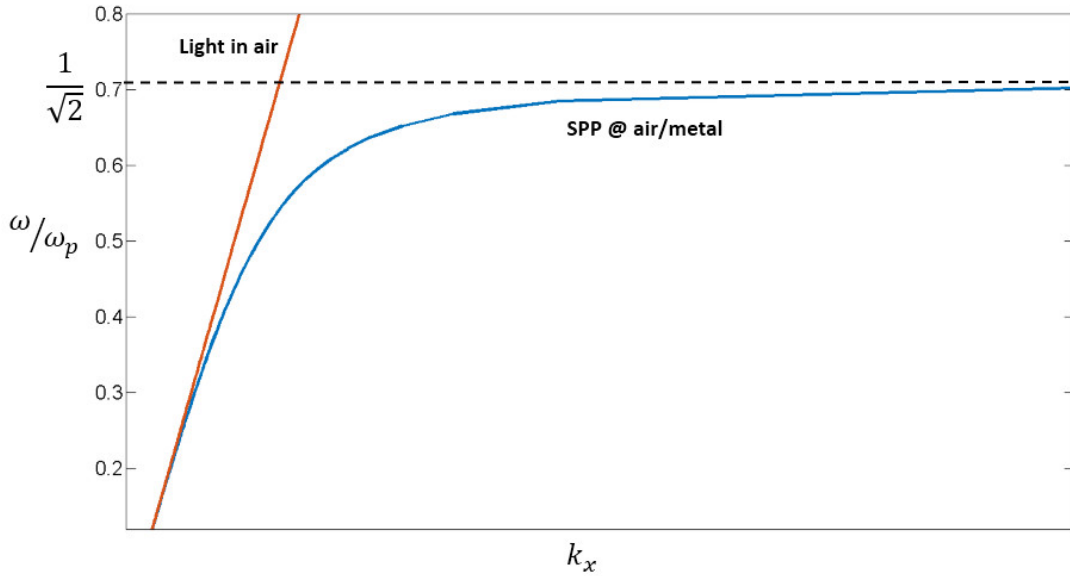


Figure 1.3. Dispersion relation of SPP on air/metal compared to light in air, the dashed line shows the cut-off frequency of the propagating SPP (ω_p is volume plasmon frequency)

In addition, one realizes that SPPs cannot be excited by direct light illumination due to energy and momentum conservation. The propagation constant wavevector corresponding to a real frequency is complex and frequency dependent. Thus, we can rewrite the form as:

$$k_x(\omega) = k_x'(\omega) + ik_x''(\omega). \quad (1-5)$$

The real part depicts the effective wavelength $\lambda_{eff} = 2\pi / k_x'$, while the imaginary part determines the propagation length $L_{spp} = 1 / 2k_x''$.

Regarding the excitation of SPPs, it can be done either optically or electrically. In terms of optical excitation, the main issue is to compensate the momentum mismatch between the photon and SPP at the same frequency. Kretschmann configuration, grating configuration and SNOM are the usual ways to excite the SPP which have been studied for a few decades[10-12].

Concerning the electrical excitation of SPP, we know the momentum of an electron is sufficient to couple directly to a SPP without any coupling medium. Hence, the electrical

excitation can be a convenient way in principle. An electron beam with a high electron energy, around a few keV can be used as it is done in SEM or Electron Energy Loss Spectroscopy (EELS) [13]. In order to have an integrated plasmonic circuit, it is more practical to use a low energy electron (a few eV) to excite SPPs. In this case, two options are possible. Either excite electrically an emitter such as a molecule or a LED which subsequently relaxes by emitting a plasmon or using a MIM tunnel junction. Only the later provides ultrafast emission without limitation by spontaneous emission time. In this manuscript I will focus on surface plasmon emission by inelastic tunneling assisted by an optical antenna.

1.3.2. Inelastic tunneling and elastic tunneling

Revisiting the tunneling phenomenon in MIM tunnel junction, a schematic drawing is shown in Fig. 1.4. The barrier height of Φ and thickness of d are formed by the forbidden gap of the insulator. Let us take a simple physical picture for the description. When a sufficiently thick oxide layer separates by two metals no tunneling happens. After we decrease the thickness of the insulator layer to the point where the eigenstates of the two electrodes overlap, tunneling becomes possible. Once a voltage (as shown in Fig. 1.4(b)) is applied between the two electrodes, the Fermi levels of the metals are offset and an electric field is induced in the insulator where a net tunneling current flows through.

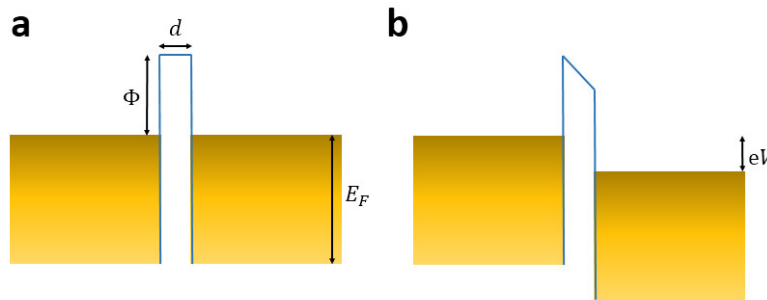


Figure 1.4. Schematic for one-dimensional representation of a tunnel junction. (a) At zero bias the Fermi levels of the two electrodes are with the same energy; the barrier is in the forbidden gap of the insulator. (b) At non zero bias, the Fermi levels of the electrode are offset by eV . The barrier tilts due to the voltage drop across it.

The quantum transition of the electron between two electrodes can be modeled using the Fermi golden rule. In the picture of elastic tunneling, as shown in Fig. 1.5(a), the tunneling electron doesn't lose energy during the whole transport. In general, the total elastic tunneling rate is defined by the overlap between the left (occupied state) electrode and the right (unoccupied state) electrode. For inelastic tunneling, the tunneling electron can excite an electromagnetic oscillator (light or SPP) and lose energy $\hbar\omega$, as shown in Fig. 1.5(b). It corresponds to the energy difference between the two electronic states.

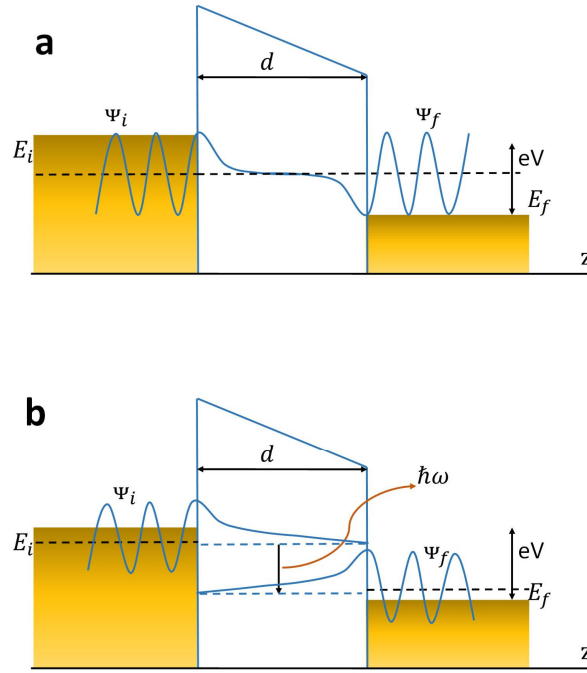


Figure 1.5. The framework of electron tunneling with a given voltage bias V ; (a) The picture of the elastic tunneling, (b) The picture of the inelastic tunneling. Note: Ψ_i and Ψ_f represent the wave function of the left and right electrode E_i and E_f are the initial and final electronic energy states.

The density of states is a key element to describe the decay rate of a quantum system. In presence of an inelastic tunneling in a MIM tunnel junction, the Hamiltonian is proportional to the local density of electromagnetic states[14]. To obtain the decay rate into surface plasmons, we need to sum over all surface plasmons. To obtain the total decay rate, we need to sum over all electromagnetic states including all the non-radiative modes. This total decay rate is simply given by using the Green tensor. Here, we clearly see that in order to avoid quenching, the electromagnetic environment of the electron has to be designed in such a way that the plasmon contribution to the local density of states dominates. This is a formidable challenge as the electron in a junction is at a distance of typically 1 nm of a metallic interface. So that the contribution of non-radiative modes to the local density of states is typically five orders of magnitude larger than the vacuum local density of states. Furthermore, in order to obtain a good efficiency, the inelastic contribution needs to be as large as possible compared to the elastic contribution. In summary, light emission by inelastic tunneling can be treated as a spontaneous emission process in a two-level system.

1.3.3. Current fluctuation and electric field inside the barrier of a tunnel junction

An alternative description of light emission by a tunnel junction is based on the fields radiated by the current fluctuations in the junction. Shot noise in electronic circuits consists of random fluctuations in a DC current. Based on the Scalapino and Rendell's work[15, 16], the power spectral density of the current fluctuations in a tunnel junction is known. The current fluctuation is given by[16]:

$$\langle I^2 \rangle(\omega) = \frac{1}{1 - \exp\left(\frac{eV}{k_B T} \left(1 - \frac{\hbar\omega}{eV}\right)\right)} eI\left(V - \frac{\hbar\omega}{e}\right) \quad (1-6)$$

where $I(V)$ is the DC characteristic of the voltage-biased tunnel junction, \hbar is reduced Planck constant, k_B is Boltzmann's constant, the ω is the frequency, and T is temperature.

Here, we have neglected the term proportional to $I\left(V + \frac{\hbar\omega}{e}\right)$ because the weighting factor

$$\frac{1}{\exp\left\{\left(eV + \hbar\omega\right) / k_B T\right\} + 1} \ll 1.$$

To extract the light emission from current noise in a MIM tunnel junction, it is important to determine the electric field inside the tunnel barrier. Then the amplitude $E(\mathbf{r}, \omega)$ of the electric field, at frequency of ω and the position of \mathbf{r} , can be written in a set of Green's functions $\mathbf{G}(\mathbf{r}, \mathbf{r}', \omega)$ [17]. Thus, we get

$$\mathbf{E}(\mathbf{r}, \omega) = i\omega\mu_0 \langle I^2 \rangle(\omega) \int d^3\mathbf{r}' \mathbf{G}(\mathbf{r}, \mathbf{r}', \omega), \quad (1-7)$$

where \mathbf{r}' is the position in the tunnel barrier and μ_0 is the vacuum permeability. Here we assume the tunnel current flow uniformly in the barrier, so that the term of the current fluctuation is only frequency dependent. At this stage, it is seen that the electric field is mainly determined by the Green function in the barrier. Thereafter, the light or SPP emission of tunnel junction turns to be a standard electromagnetic calculation task.

1.3.4. STM-based tunnel junction

The SPP emission from a scanning tunneling microscope (STM) based tunnel junction was demonstrated by P. Bharadwaj et al and T Wang et al in 2011[18, 19]. Since the photoemission from STM junction was discovered[2], it has been suggested that the tunneling electron excites a gap plasmon (generated between tip and surface) which can in turn excite a propagating SPP on the metallic surface. This SPP can leak through the metal layer into the glass substrate if the thickness is thin enough as compared to the metal skin depth. As shown in Fig. 1.6, the inelastic tunneling electron has been employed to excite a gap plasmon in the junction of a gold tip and a monocrystalline gold nanowire.

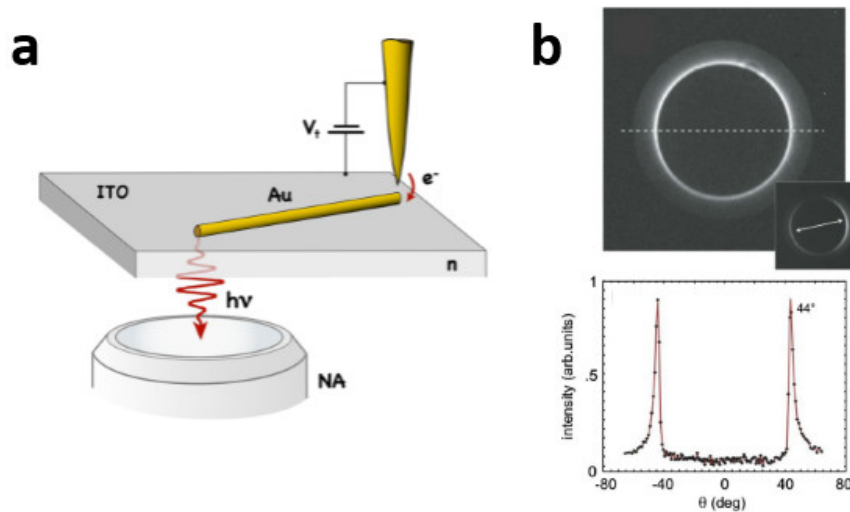


Figure 1.6 (a) Configuration of the experiment for the SPP emission within STM-nanowire junction; (b) Far-field SPP emission pattern in the back focal plane of the objective. Figures were taken from the reference[18].

The excited propagating SPP travels along the wire and scatters at the end of the wire. The technique of leakage radiation microscopy (LRM)[20] allows observing the propagating SPP in the Fourier plane image (see Fig. 1.6(b)). The electron-to-photon (plasmon) conversion efficiency was estimated to be around 10^{-5} which is a typical order of magnitude [1].

The STM has an ability to provide a nice platform to analyze light emission of simple nano object (for example, molecular layer) within sub nanometer resolution[21, 22]. However, in order to develop a large-area compatible on-chip plasmon source, a full-integrated nanodevice accompanied with MIM tunnel junctions is required.

1.3.5. Integrated tunnel junction

The first SPP source with integrated MIM tunnel junction was experimentally demonstrated by Du et al[23]. Basically in their work, a cross Al/AlO_x/Au junction was aligned via two steps of standard photolithography, schematically shown in Fig. 1.7(a). A 2nm of Aluminum oxide layer can be formed naturally during the lift-off process. Once applied a voltage bias on the junction, see the real image (Fig. 1.7(b)) and the back focal plane image (Fig. 1.7(c)), the MIM SPP, bound SPP and edge SPP can be detected properly. In terms of the electron-to-plasmon conversion efficiency, the authors claim to have measured 14%. This value is derived from a coupling between two junctions, one serves as a source and the second one as a detector. The detection is performed by applying a bias on the junction and detecting the tunnel current variation when the source is active. It is assumed that the observed modulation is only due to surface plasmons and it is assumed that the electron-to-plasmon conversion in the source is equal to the plasmon electron conversion in the detector. No clear explanation for the 14% value was given. It is unclear if other electromagnetic coupling can be ruled out. However, the data reported for leakage radiation microscopy (LRM) allow to directly estimate the SPP conversion efficiency, and it gives a value around 10^{-7} , which is a standard value among the literature.

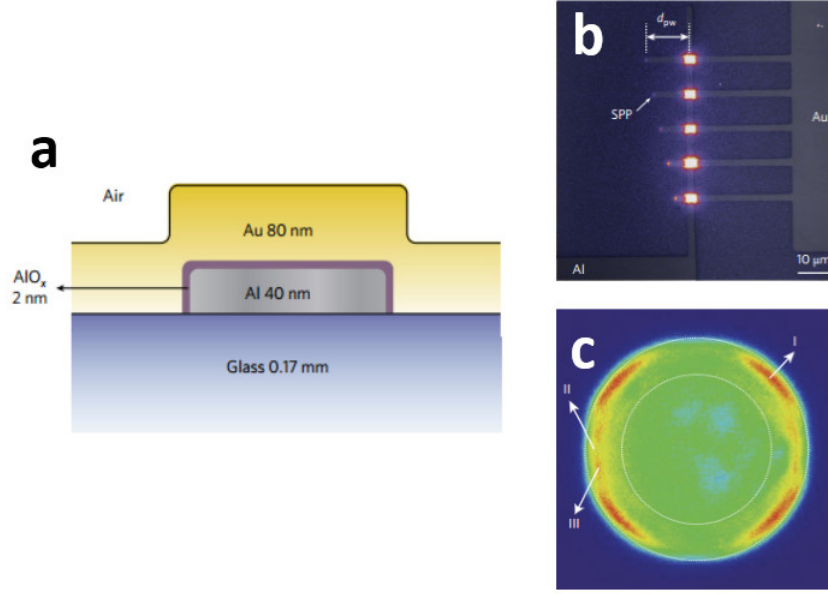


Figure 1.7 (a) Schematic of the MIM (Au/AIO_x/Al) tunnel junction; (b-c) real and back focal plane image of the SPP emission within a voltage bias on the junction. pictures were taken from the reference[23].

The efficiency of 14% is not compatible with the decay length of the mode. Indeed, the decay length of the plasmon mode in the gap is on the order of 150nm whereas the emitter size is 1.4 μ m. Hence, most of the plasmons emitted in the junction cannot exit the source without being absorbed. To derive the 150nm value, we solve the dispersion relation of the gap mode in the MIM configuration. We consider two infinite Al half-spaces separated by a 2nm thick dielectric layer (denoted as d , the material is Al₂O₃). In terms of the MIM-SPP, the dispersion relation can be simply derived as:

$$2 = i \tan(k_{d,z}d) \left(\frac{\varepsilon_d k_{m,z}}{\varepsilon_m k_{d,z}} + \frac{\varepsilon_m k_{d,z}}{\varepsilon_d k_{m,z}} \right), \quad (1-8)$$

$$k_{d,z}^2 = \varepsilon_d k_0^2 - k_x^2$$

where $k_{m(d),z}$ is the wave vector of the z-component in metal and dielectric, respectively. k_0 is the wave vector in the vacuum, $\varepsilon_{(m,d)}$ is the permittivity of the metal and the dielectric, respectively. k_x is the propagation constant of the MIM-SPP. Having taken the dielectric constant of Al and Al₂O₃ from the reference[24, 25], we calculated the effective index and the propagation length of the MIM-SPP as function of the wavelength (400nm-1200nm). The results are plotted in Fig. 1.8.

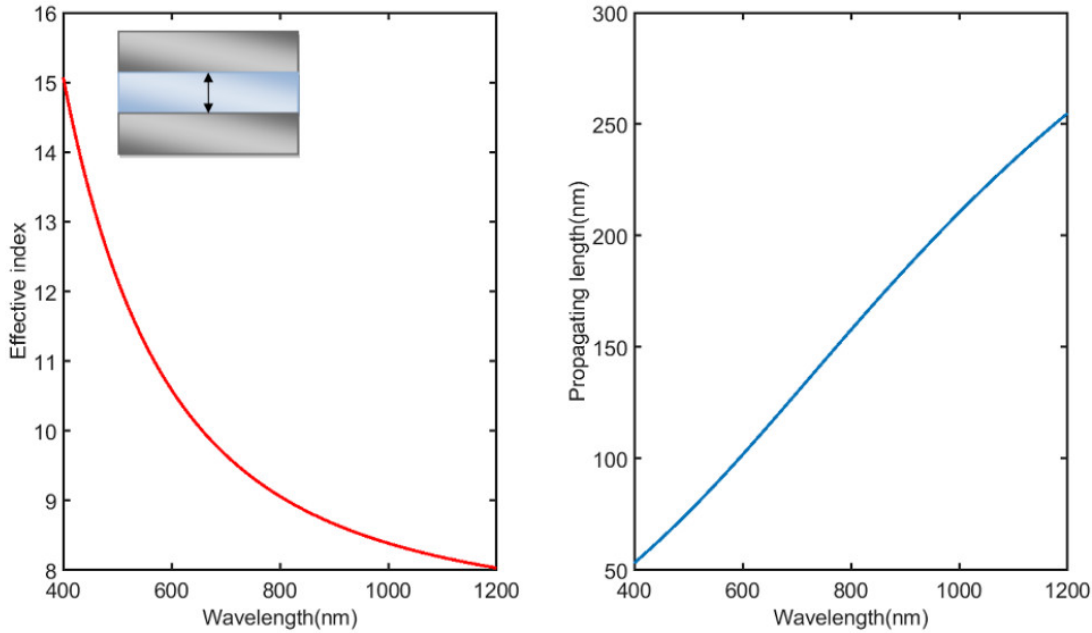


Figure 1.8 (a-b) The effective index and the propagation length of MIM-SPP within Al/AIO_x/Al configuration as function of wavelength. The inset depicts the MIM structure.

The large effective index suggests that the MIM-SPP is an extremely confined mode. The confinement additionally links to large propagation losses, and a short propagation length, below 150 nm in the visible regime (shown in Fig. 1.8b). Regarding a planar MIM junction (size above a few μm), a majority of the MIM-SPP, which is the original supplier for the bound SPP and edge SPP, excited by the tunneling current noise are absorbed before reaching the edge of the junction. Only the MIM-SPP created close to the junction edge can contribute to an ‘output’ SPP. This is thus not consistent with a 14% electron-to-plasmon conversion efficiency in ref[23].

From the previous discussion, we conclude that an efficient SPP source based on a MIM junction should not be significantly larger than the MIM-SPP mode propagation length. A further issue is the coupling between the MIM-SPP mode in the source and the emitted SPP. To this aim, a plasmonic antenna has been proposed [26].

1.4. Optical antenna assisted light emitting tunnel junction (LETJ)

1.4.1. Plasmonic nanoantenna

A plasmonic nanoantenna is a transducer between free propagating electromagnetic energy and a localized energy at nanoscale. A plasmonic nanoantenna has sustained a localized oscillation of surface charge density called localized surface plasmon (LSP). See the schematic figure of LSP in Fig 1.9; light field can interact with a particle smaller than the incident wavelength.

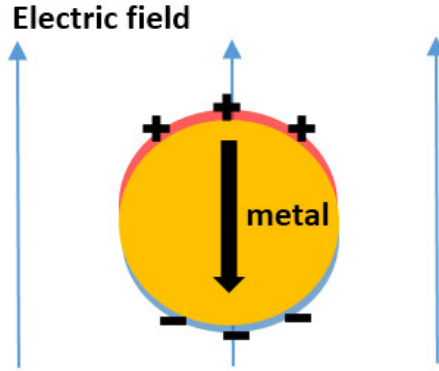


Figure 1.9 Schematic of LSP in a metallic nanosphere

The role of particle size, shape, material, and dielectric environment determine the LSP resonant wavelength[27, 28]. In principle, an optical antenna can act as a super lens since it localizes the electromagnetic field. As shown in Fig. 1.10(a), in presence of a resonant antenna, the power absorption is enhanced by a factor:

$$\frac{P_{ant}}{P_0} = \frac{|\mathbf{E}_{ant}(\mathbf{r}_0)|^2}{|\mathbf{E}_0(\mathbf{r}_0)|^2}, \quad (1-9)$$

where $\mathbf{E}_{ant}(\mathbf{r}_0)$ and $\mathbf{E}_0(\mathbf{r}_0)$ are the electric field at the receiver position with/without antenna, respectively. Meanwhile, consider an emitter has to be dissipated energy into far-field via an optical antenna, as in Fig. 1.10(b). We assume the emitter has a dipole moment \mathbf{p} , the power dissipation rate at position \mathbf{r}_0 and frequency ω_0 in an arbitrary environment can be written as:

$$\gamma = \frac{\pi\omega_0}{3\hbar\epsilon_0} |\mathbf{p}|^2 \rho_0(\mathbf{r}_0, \omega_0), \quad (1-10)$$

where $\rho_p(\mathbf{r}_0, \omega_0)$ is the partial LDOS which is given by[29]:

$$\rho_p(\mathbf{r}_0, \omega_0) = \frac{6\omega_0}{\pi c^2} \{ n_p \cdot \text{Im}[\mathbf{G}(\mathbf{r}_0, \mathbf{r}_0; \omega_0)] \cdot n_p \} \quad (1-11)$$

Now the spontaneous emission of a two-level quantum system has been completely transferred to a classical treatment based on Poynting's theorem. Compared to the reference emission without antenna, the LDOS in the vacuum can be:

$$\rho_0 = \frac{\omega_0^2}{\pi^2 c^3}, \quad (1-12)$$

where c is the light speed in vacuum. Thus, the emission enhancement factor in presence of an optical antenna will be like:

$$\frac{\gamma}{\gamma_0} = \frac{\rho_p}{\rho_0} \quad (1-13)$$

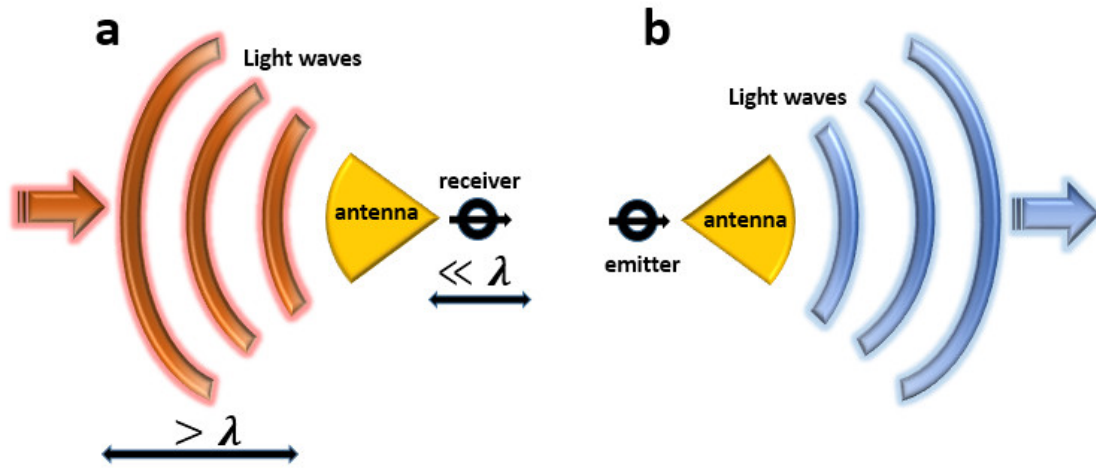


Figure 1.10. Optical antenna functional mechanism. (a) As a receiving antenna; (b) As a transmitting antenna.

A plasmonic mode has a good feature for its subwavelength mode volume, while it brings additional cavity losses due to metal intrinsic absorption. The total dissipated power includes both the radiative (γ_r) and non-radiative (γ_{nr}) part. We then define the antenna radiative efficiency:

$$\eta_{antenna} = \frac{\gamma_r}{\gamma_r + \gamma_{nr}} \quad (1-14)$$

Since we are more concerning the light emission accompanied with an optical antenna, I am giving a small example to show how antennas work.

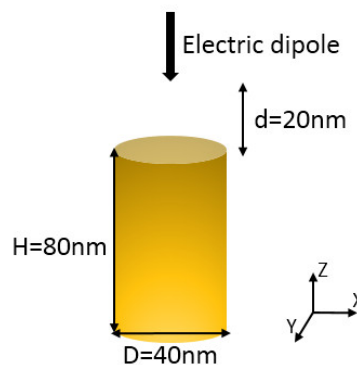


Figure 1.11 An electric dipole, with z polarized 20nm, is 20nm away on axis from a gold nanorod. The diameter and height of the nanorod are 40nm and 80nm, respectively. The environment of the gold nanorod is air.

See Fig. 1.12(a), an enhanced total emission power spectrum (blue curve) can be obtained, and two orders of magnitude of intensity is achieved at the resonance. In terms of the radiative power, at the antenna mode, there are still two order-enhanced power. Judging from Fig. 1.12(b), a dipole-like mode field distribution can be seen along the z direction of the nanorod. The field intensity at the corner of the rod is three orders magnitude higher than the reference, which demonstrates the antenna mode can assist a light emitter to gain a bigger LDOS to emit more efficiently.

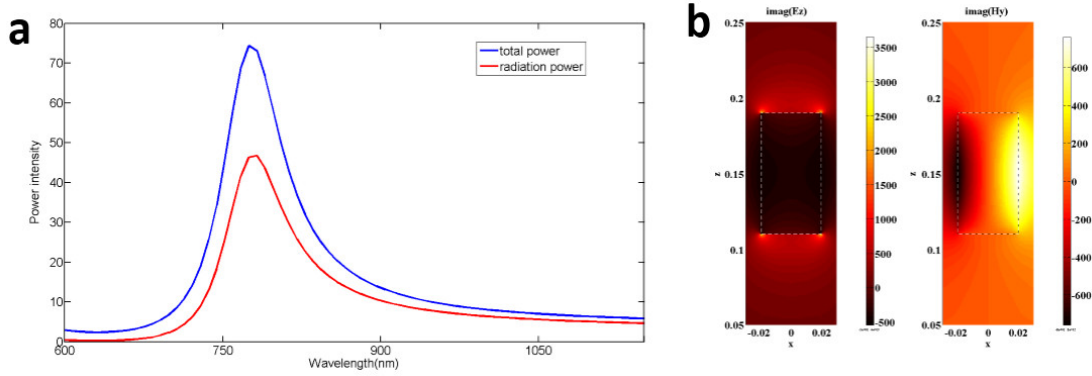


Figure 1.12 (a) Emission power spectra normalized by the dipole emission in the vacuum; the blue line and red line are represented the total emission and radiative emission, respectively. (b) The imaginary part of electromagnetic field at the wavelength of 775nm, the left one is the E_z component and right one is the H_y component.

1.4.2. Enhanced LETJ with aid of an optical antenna

Within fast development of nanotechnologies, people can have access to manipulate light at nanoscale thanks to an optical antenna[30, 31]. Using the inelastic electron tunneling in MIM structures, where electrons transfer allow exciting a LSP mode. Thus, IET is a good tool to drive the optical antenna directly with a small DC voltage (a few eV). Up to now, several groups have proved the concept of the antenna assisted LETJ[7, 26, 32]. Johannes Kern and coworker had utilized monodisperse gold nanoparticles covered with a ligand shell to introduce a double barrier-tunneling junction. In their project, the antenna were milled via focused ion beam lithography from a piece of monocrystalline gold flake. Then, an AFM was used to push the particles to the desired position in the gap to form the small gap ($\sim 1.5\text{nm}$) for tunneling, see Fig. 1.13(a). Once the junction was voltage biased properly, the junction can emit light with dipolar radiation pattern. By giving a higher voltage, they observed the blue-shift electroluminescence spectra where gives the approve of the inelastic tunneling, see Fig. 1.13(b). Additionally, they also constructed a reference structure for showing a non-resonant antenna with quantum efficiency where 2 orders of magnitude lower than the resonant antenna junction. The best-performed antenna junction can reach $\sim 3 \times 10^{-4}$ of quantum efficiency.

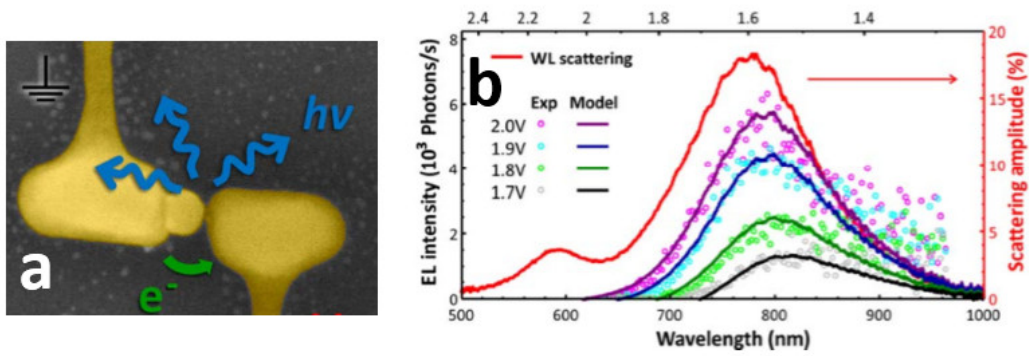


Figure 1.13 Electrically driven optical antenna. (a) SEM picture of the antenna junction; (b) Electroluminescence spectra with different biased voltage and related scattering spectrum of the antenna junction. Figures are extracted from the reference[26].

Moreover, optical antenna is also a good tool for tailoring the far-field emission pattern. Thus, combining both strong emission enhancement and emission pattern shaping, is an important future application in IETJ. Recently, S.P. Gurunaryanan and coworker had fabricated an IET driven unidirectional optical antenna[33]. They had applied electronically induced atom migration in a single antenna arm to form the gap in which allows tunneling happen. Here there is an angle introduced in the plane of the connected single arms, which has a V-shape of the coupled arms. When the inelastic tunneling activated the junction, the V-shape creates a unidirectional emission pattern, see Fig 1.14.

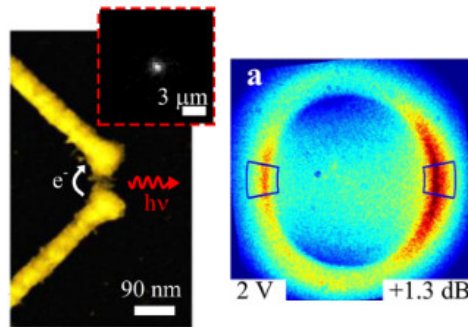


Figure 1.14 Left panel: sem feature of the V-shape antenna junction, inset figure for showing the light emission spot; right panel: full spectrum back focal plane of V-antenna revealing a directional radiation pattern. Figures were taken from the reference[33]

Towards better electron-to-photon conversion efficiency, the antenna engineering is playing a big role. Regarding the MIM configuration, a shortened MIM gap and more monocrystalline-like electrode material may benefit a less ‘quenching’ loss. In Qian et al[32], they used monocrystalline silver as the electrode material and the junction was formed by two aligned silver nanocrystals edge to edge, thus the quenching losses in the electrodes were reduced to a minimum level. This allowed them to obtain the electron-to-photon conversion efficiency up to 2%.

1.5. Conclusion

In this chapter, we have introduced the background of inelastic tunneling phenomenon in a MIM tunnel junction. Two equivalent points of view can be adopted to

explain light emission. The Fermi golden rule can be used to derive the light emission by inelastic tunneling. Alternatively, the fluctuation of the intensity in the barrier can be viewed as the origin of the radiation. Once we have an optical antenna mode, the light emission process can be enhanced thanks to the additional channel in presence of antenna. The goal of my PhD is to control the emission frequency and to improve the electron-to-plasmon (photon) conversion efficiency in MIM tunnel junction by using an optical antenna. The rest of manuscript will be organized as follow:

In chapter 2, we will describe the light emission by inelastic tunneling via two different approaches. Firstly, we treat the light emission process as a transition between an initial state and a final state. The transition rate can be calculated by the Fermi golden rule. To improve the electron-to-plasmon or photon efficiency of a tunnel junction, an efficient antenna mode is one of the promising ways by taking advantage of the radiative loss and the LDOS engineering. Secondly, the light emission process can be viewed as a fluctuating current radiation. An enhanced radiation, thus good electron-to-plasmon or photon efficiency, can be obtained by an enhanced field imposed by the coupling between the current fluctuation and a resonant antenna mode. Combining these two approaches, a smart antenna design is highly required.

In chapter 3, we will investigate the SPP emission in a STM configuration. We theoretically demonstrate that the SPP emission can be enhanced by using a nanorod or a nanocone between a STM tip and a metallic film. At this stage, we find two orders of magnitude enhancement.

In chapter 4, we will present a theoretical study of SPP emission from a MIM cylindrical nanopatch antennas with sub-nm gaps. The key message is the identification of a hybrid mode resulting from the strong coupling between a gap mode that yields a large contribution to the LDOS and an antenna mode that is able to efficiently couple to SPPs. We predict an enhanced total SPP emission thanks to the mode hybridization. Furthermore, we will show that the antenna emits as many photons than plasmons when the surrounding medium is air. However, when increasing the refractive index of the host medium, more power is emitted into plasmons and the plasmonic efficiency can be improved up to 30% with a gap of 1nm at a working wavelength around 800nm.

In chapter 5, we will realize the process developed for the fabrication of tunnel junctions with nanopatch antennas electrically connected. The tunnel junction is based on an Al/AlOx/Au configuration. We introduce two different types of antenna (a strip patch antenna and a cylindrical patch antenna). The Al bottom electrode is deposited by a standard UV photolithography. We thermally oxidize a thin Al film to generate 3 nm of AlOx layer to be used as a tunnel barrier. The top Au electrode is fabricated by a standard e-beam lithography. To make an electrical contact for applying a voltage, we fabricate in-plane connection pads for the strip antenna junction; while for the cylindrical antenna junction, we use a planarization process to fabricate an insulating spacer and then put a ‘soft’ top contact by an ITO coated PDMS stamp. We have obtained a subnanometer roughness and we manage to fabricate a patch antenna with a width on the order of 100 nm over 60 μm length with a width fluctuation smaller than 10 nm.

In chapter 6, we will report the experiments on antenna surface plasmon emission by inelastic tunneling (ASPEIT). We show that the emission spectrum can be tuned by varying the width of the antenna. An important feature of the antenna is its ability to enhance the emitted power and the efficiency of the coupling between electrons and plasmons. The emitted power of the ASPEIT is demonstrated to operate in the 10 pW regime instead of a few fW for a standard STM-based junction. The ASPEIT can control the SPP emission spectrum and polarization. In terms of efficiency, we demonstrate a more than three orders of magnitude enhancement over a planar junction by using

ASPEIT.

Chapter 2

Theoretical description of light emission by a tunnel junction in presence of a resonant nanoantenna

- 2.1. Introduction
- 2.2. Light emission by inelastic tunneling: the fluctuating current radiation approach
- 2.3. Light emission by inelastic tunneling: the Fermi golden rule approach
- 2.4. Discussion and conclusion

2.1. Introduction

Light emission by inelastic tunneling can be modeled using two different points of views. On one hand, it can be viewed as a transition between an initial state and a final state. The transition rate can be derived using Fermi golden rule. On the other hand, it can be viewed as fluctuating current. Hence, the radiation due to fluctuations can be computed. In what follows, we introduce both approaches. Our goal is to derive an explicit form of the emitted power and to use it to model the electron to photon conversion efficiency while accounting for the role of an antenna.

2.2. Light emission by inelastic tunneling: the fluctuating current radiation approach

We start by considering that light emission from a tunnel junction can be modelled as the field radiated by the current density fluctuations of the tunneling current[17, 34, 35]. The power spectral density of the current density fluctuations is derived from a model of the tunneling current[16, 35, 36].

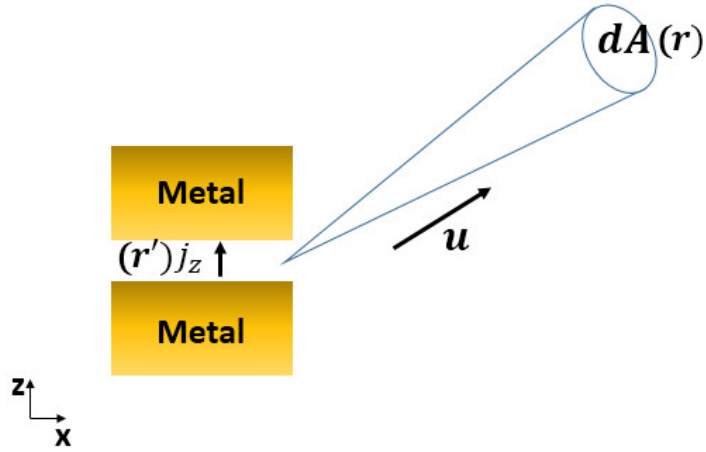


Figure 2.1 Illustration of reciprocity principle for the light emission of a tunnel junction. \mathbf{r} is a position in the far-field, \mathbf{r}' is a current element position in the tunnel barrier.

As shown in Fig 2.1, the radiation into the far-field is due to the current fluctuation of the tunneling current density in the z -direction (j_z). The power dP radiated to the far-field in the direction \mathbf{u} in a solid angle subtended by the area dA is given by:

$$dP = \langle \mathbf{E}(\mathbf{r}, t) \times \mathbf{H}(\mathbf{r}, t) \rangle \mathbf{u} \cdot dA, \quad (2-1)$$

where \mathbf{E} , \mathbf{H} are the electric and magnetic field, respectively. The brackets denote a statistical average over an ensemble of realizations of the fluctuating current. We now introduce the Fourier transform of the electromagnetic field and current density:

$$\mathbf{E}(\mathbf{r}, t) = \int \mathbf{E}(\mathbf{r}, \omega) \cdot e^{-i\omega t} \frac{d\omega}{2\pi}, \quad (2-2)$$

$$\mathbf{H}(\mathbf{r}, t) = \int \mathbf{H}(\mathbf{r}, \omega) \cdot e^{-i\omega t} \frac{d\omega}{2\pi}, \quad (2-2)$$

$$j_z(\mathbf{r}, t) = \int j_z(\mathbf{r}, \omega) \cdot e^{-i\omega t} \frac{d\omega}{2\pi}. \quad (2-3)$$

For a stationary process, the Fourier transform does not exist in the sense of a function. However, the power spectral density $S_{j_n, j_m}(\mathbf{r}, \mathbf{r}', \omega)$ can be defined and we can write:

$$\langle j_n(\mathbf{r}, \omega) j_m(\mathbf{r}', \omega') \rangle = 2\pi \delta(\omega + \omega') S_{j_n, j_m}(\mathbf{r}, \mathbf{r}', \omega). \quad (2-4)$$

Note that $j_m(\mathbf{r}', \omega') = j_m^*(\mathbf{r}', -\omega')$ as $j_m(\mathbf{r}', t)$ is a real function. The electric field at \mathbf{r} radiated by the current density in the tunnel junction[29], is given by

$$\mathbf{E}(\mathbf{r}, \omega) = i\omega\mu_0 \int d^3\mathbf{r}' \mathbf{G}(\mathbf{r}, \mathbf{r}', \omega) \mathbf{j}(\mathbf{r}', \omega), \quad (2-5)$$

where \mathbf{G} is the Green tensor of the system. To specify the polarization, we introduce the unit vector \mathbf{e}^l where $l=s$ or p so that $\mathbf{E} = E^l \mathbf{e}^l + E^p \mathbf{e}^p$. Using Einstein notation, the n -th component of the l -polarized electric field amplitude is

$$E_n^l(\mathbf{r}, \omega) = i\omega\mu_0 \int d^3\mathbf{r}' e_n^l G_{nm}(\mathbf{r}, \mathbf{r}', \omega) j_m(\mathbf{r}', \omega). \quad (2-6)$$

Based on (2-1), the radiated power in l -polarization is

$$dP^l = \int \frac{d\omega}{2\pi} \int \frac{d\omega'}{2\pi} e^{-i(\omega+\omega')t} \langle \mathbf{E}^l(\mathbf{r}, \omega) \times \mathbf{H}^l(\mathbf{r}, \omega') \rangle \cdot \mathbf{u} dA. \quad (2-7)$$

By using $\mathbf{H}^l(\mathbf{r}, \omega) = \frac{\mathbf{B}^l(\mathbf{r}, \omega)}{\mu_0}$ and $\mathbf{B}^l(\mathbf{r}, \omega) = \frac{\mathbf{k}}{\omega} \times \mathbf{E}^l(\mathbf{r}, \omega) = \frac{n}{c} \mathbf{u} \times \mathbf{E}^l(\mathbf{r}, \omega)$

we get:

$$dP^l = n\varepsilon_0 c \int \frac{d\omega}{2\pi} \int \frac{d\omega'}{2\pi} e^{-i(\omega+\omega')t} \langle \mathbf{E}^l(\mathbf{r}, \omega) \cdot \mathbf{E}^l(\mathbf{r}, \omega') \rangle dA. \quad (2-8)$$

Using (2-4) and (2-6), we find:

$$dP^l = n\varepsilon_0 c \int \frac{d\omega}{2\pi} \mu_0^2 \omega^2 \int d^3\mathbf{r}' e_n^l G_{np}(\mathbf{r}, \mathbf{r}', \omega) \int d^3\mathbf{r}'' e_n^l G_{nq}^*(\mathbf{r}, \mathbf{r}'', \omega) S_{jp,jq}(\mathbf{r}', \mathbf{r}'', \omega) dA. \quad (2-9)$$

Here, we only consider the z -component of the current density in the junction, so that $p=q=z$:

$$dP^l = n\mu_0 c \int \frac{d\omega}{2\pi} \left(\frac{\omega^2}{c^2} \right) \int d^3\mathbf{r}' e_n^l G_{nz}(\mathbf{r}, \mathbf{r}', \omega) \int d^3\mathbf{r}'' e_n^l G_{nz}^*(\mathbf{r}, \mathbf{r}'', \omega) S_{jz,jz}(\mathbf{r}', \mathbf{r}'', \omega) dA. \quad (2-10)$$

To proceed, we use a simplified form of the two points correlation function:

$$S_{jz,jz}(\mathbf{r}, \mathbf{r}', \omega) = \frac{\langle I^2 \rangle(\omega)}{\Sigma} \delta(\mathbf{r} - \mathbf{r}'), \quad (2-11)$$

where $\langle I^2 \rangle(\omega)$ is the intensity power spectral density and Σ represents the area of the junction. This approximation is based on the fact that the current density in different electronic modes are uncorrelated and that a typical mode occupies an area given by λ_F^2/π , where λ_F is the Fermi wavelength on the order of a few angstroms. We Insert (2-11) into Eq. (2-10), and introduce the solid angle $dA = r^2 d\Omega$ and the vacuum impedance $Z_0 = \mu_0 c$. Moreover, we note that, since the gap is deeply subwavelength, the field does not vary rapidly along z in the gap so that the integration over z and z' yields a t^2 dependence where t is the barrier thickness of the tunnel junction. Thus we obtain:

$$dP^l = Z_0 n \int d\omega \left(\frac{t^2 \omega^2}{c^2} \right) \langle I^2 \rangle(\omega) \int \frac{d^2\mathbf{r}'_{\parallel}}{\Sigma} r^2 |e_n^l G_{nz}(\mathbf{r}, \mathbf{r}'_{\parallel}, 0, \omega)|^2 d\Omega, \quad (2-12)$$

where $\mathbf{r}'_{\parallel} = (x', y', 0)$. Now we show that the term $r^2 |G_{nz}(\mathbf{r}, \mathbf{r}'_{\parallel}, 0, \omega)|^2$ can be related to the field enhancement factor in the junction by using the reciprocity theorem[29]. To proceed, we consider a dipole source at $\mathbf{r} = r\mathbf{u}$ in the far field with a dipole moment $p_{inc} \cdot \mathbf{e}^l$.

Using equation (2-6), we see that this dipole generates a field in the junction at \mathbf{r}' :

$$E_z^l(\mathbf{r}', \omega) = \omega^2 \mu_0 G_{zn}(\mathbf{r}', \mathbf{r}, \omega) p_{inc} e_n^l. \quad (2-13)$$

The same dipole in vacuum generates a field, whose amplitude is given by:

$$E_{inc} = \mu_0 \omega^2 \frac{e^{ikr}}{4\pi r} p_{inc}, \quad (2-14)$$

By taking the ratio of the field in the gap (2-13) and the incident field (2-14) illuminating the junction, we define the field enhancement factor:

$$K^l(\mathbf{r}', \mathbf{u}, \omega) = \left| \frac{E_z^l(\mathbf{r}', \mathbf{u}, \omega)}{E_{inc}(\mathbf{r}', \mathbf{u}, \omega)} \right| = 4\pi r \left| G_{zn}(\mathbf{r}', \mathbf{r}, \omega) e_n^l \right|. \quad (2-15)$$

The reciprocity theorem gives:

$$G_{zn}(\mathbf{r}', \mathbf{r}, \omega) e_n^l = e_n^l G_{nz}(\mathbf{r}, \mathbf{r}', \omega). \quad (2-16)$$

Using (2-13), (2-14) and (2-16), we obtain:

$$K^l(\mathbf{r}', \mathbf{u}, \omega) = \left| \frac{E_z}{E_{inc}} \right| = 4\pi r \left| e_n^l G_{nz}(\mathbf{r}, \mathbf{r}', \omega) \right|. \quad (2-17)$$

Inserting (2-17) into (2-12), we have

$$dP^l = Z_0 n \int \frac{d\omega}{2\pi} \left(\frac{\omega^2 t^2}{c^2} \right) \int_{\Sigma} \frac{d^2 \mathbf{r}'}{\Sigma} \frac{|K^l(\mathbf{r}', \mathbf{u}, \omega)|^2}{16\pi^2} \langle I^2 \rangle(\omega) d\Omega. \quad (2-18)$$

Finally, the power can be cast in the form:

$$\frac{dP^l}{d\Omega} = Z_0 n \int \frac{d\omega}{8\pi} \left(\frac{t}{\lambda} \right)^2 \overline{|K^l(\mathbf{u}, \omega)|^2} \langle I^2 \rangle(\omega), \quad (2-19)$$

where we take $\overline{|K^l(\mathbf{u}, \omega)|^2}$ to be the averaged field enhancement factor over the whole junction barrier. We now introduce the differential radiation impedance ($R^l(\mathbf{u}, \omega)$) of a tunnel junction with unit Ωsr^{-1} , which accounts for the coupling between the tunneling current and the power spectral density of the power radiated per solid angle. Based on this, (2-19) can be written as:

$$\frac{dP^l}{d\Omega} = \int d\omega R^l(\mathbf{u}, \omega) \langle I^2 \rangle(\omega), \quad (2-20)$$

where $R^l(\mathbf{u}, \omega) = \frac{Z_0 n}{8\pi} \left(\frac{t}{\lambda}\right)^2 \overline{|K^l(\mathbf{u}, \omega)|^2}$. The physical content of this expression is very simple. We remind that a dipolar wire with length t and monochromatic current with intensity I radiates a power $RI^2 = \frac{\pi}{3} Z_0 \left(\frac{t}{\lambda}\right)^2 I^2$. It follows that the junction behaves as an emitting electric dipole. The key difference is the enhancement factor provided by the antenna. This enhancement factor becomes significant if the plasmonic mode is excited, namely for a specific angle of incidence and for specific frequencies.

We now simplify the expression of the power emitted by taking into account the fact that the antenna selects a bandwidth centered at a particular frequency. If we consider a specific bandwidth with a central frequency of ω_0 , which can correspond to a resonant antenna, it can be cast as:

$$\begin{aligned} \frac{dP^l}{d\Omega} &= R^l(\mathbf{u}, \omega_0) \langle I^2 \rangle(\omega_0) \int d\omega \frac{R^l(\mathbf{u}, \omega) \langle I^2 \rangle(\omega)}{R^l(\mathbf{u}, \omega_0) \langle I^2 \rangle(\omega_0)}, \\ &= R^l(\mathbf{u}, \omega_0) \langle I^2 \rangle(\omega_0) \Delta\omega \end{aligned} \quad (2-21)$$

where $\Delta\omega = \int d\omega \frac{R^l(\mathbf{u}, \omega) \langle I^2 \rangle(\omega)}{R^l(\mathbf{u}, \omega_0) \langle I^2 \rangle(\omega_0)}$ denotes the bandwidth of the antenna mode.

For a standard junction, our implementation of current fluctuation is based on the model from the reference[16, 36, 37]:

$$\langle I^2 \rangle(\omega) = \frac{1}{1 - \exp\left(\frac{eV}{k_B T} \left(1 - \frac{\hbar\omega}{eV}\right)\right)} eI\left(V - \frac{\hbar\omega}{e}\right), \quad (2-22)$$

where $I(V)$ is the dc characteristic of the voltage-biased tunnel junction, e is the electron charge, \hbar is the reduced Planck's constant, k_B is Boltzmann's constant, and T is temperature. Here, we have neglected the term proportional to $I\left(V + \frac{\hbar\omega}{e}\right)$ because the

weighting factor $\frac{1}{\exp\{(eV + \hbar\omega)/k_B T\} + 1} \ll 1$. In terms of the electron-to-photon conversion efficiency, based on (2-21), we approximately write the efficiency:

$$\eta_{e-p} = \frac{N_{photon}}{N_{electron}} = \frac{dP^l}{\hbar\omega_0} \frac{e}{I(V)} = 2\pi \frac{R^l(\mathbf{u}, \omega_0) \langle I^2 \rangle(\omega_0) \Delta\omega \Delta\Omega}{\hbar\omega_0} \frac{e}{I(V)}. \quad (2-23)$$

Introducing the quantum of resistance $R_k = h/e^2$, we have:

$$\eta_{e-p}(\omega_0) = \left[\frac{Z_0}{R_k} \right] \frac{\Delta\omega}{\omega_0} \frac{n}{4} \left(\frac{t}{\lambda_0}\right)^2 \overline{|K^l(\mathbf{u}, \omega_0)|^2} \frac{\langle I^2 \rangle(\omega_0)}{eI(V)} \Delta\Omega. \quad (2-24)$$

In addition, based on the tunnel current model from Scalapino and co-workers[16], the noise spectral density at finite frequency is the Eq. (2-22), which is a non-linear function of frequency and voltage. Furthermore, a simplified form is also widely used in literature[7, 17, 35, 38, 39], which simply can be derived as:

$$\langle I^2 \rangle(\omega) = \frac{1}{1 - \exp\left(-\frac{eV}{k_B T} \left(1 - \frac{\hbar\omega}{eV}\right)\right)} eI_0 \left(1 - \frac{\hbar\omega}{eV}\right), \quad (2-25)$$

where I_0 is the tunnel current under a bias voltage of V . In order to clarify the difference between these two versions, we take an example for a comparison. We choose a standard planar MIM junction with a tunnel barrier thickness of 3nm and a junction area of $250\mu\text{m}^2$. The I-V characteristic is based on an analytical form from the Simmons's model[40, 41]. The current spectral density is depicted in Fig. 2.2. We show three different bias voltages from 1.2V to 2V for the model 1 given by Eq. (2-25) (denoted m1, dashed line) and the model 2 given by Eq. (2-22) (denoted m2, solid line) at room temperature.

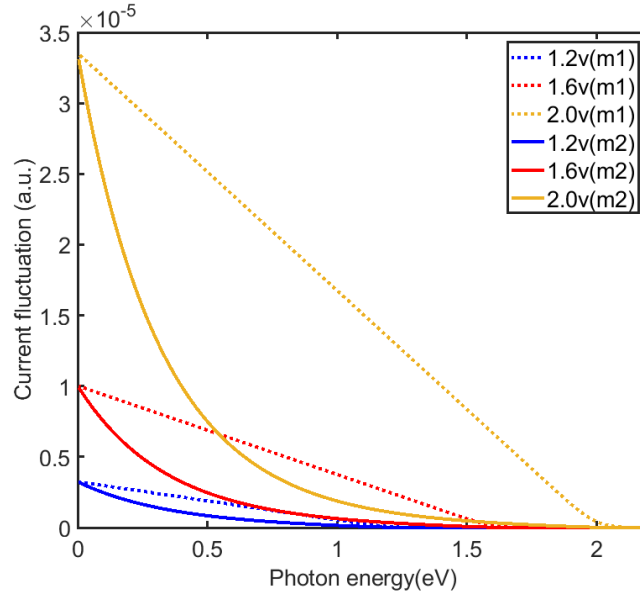


Figure 2.2 Tunneling current noise spectral density by varying three different voltages from 1.2V to 2V, the dashed line stands for the model 1 (denoted m1) and the solid line stands for the model 2 (denoted m2).

It is seen that at a lower frequency, there is a small difference between these two models, while towards a higher frequency, the difference is increased. The model 1 clearly overestimates the current fluctuations.

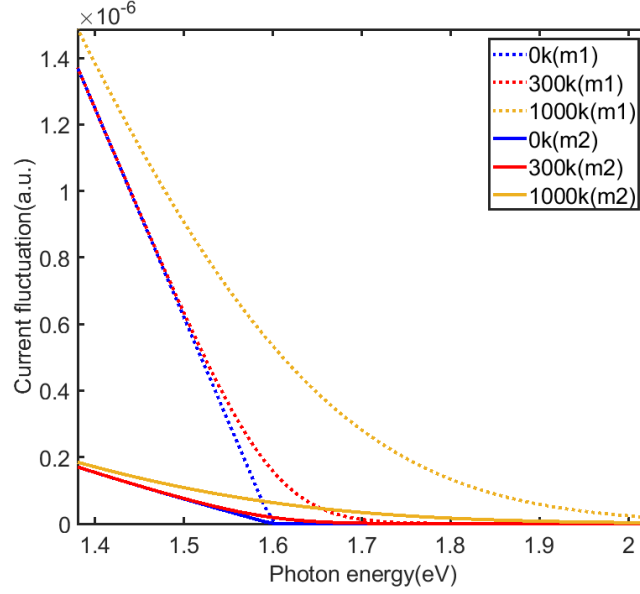


Figure 2.3 Tunneling current noise spectral density by varying three different temperatures from 0K to 1000K. The bias voltage is 1.6V, the dashed line stands for the model 1 (m1) and the solid line stands for the model 2 (m2).

In parallel, we also investigate the influence for the current noise with a finite temperature. We plot in Fig. 2.3, the two models for three different temperatures from 0K to 1000K under a bias voltage of 1.6V. It is seen that the model 1 has again a larger spectral noise density than the model 2. Moreover, at higher temperature, the spectrum cut-off at high frequency is smoothed.

2.3. Light emission by inelastic tunneling: the Fermi golden rule approach

As mentioned in Chapter 1, the light emission by inelastic tunneling electrons can be treated as a two-step procedures: firstly, tunneling electrons get through a tunneling barrier inelastically and have to be coupled with electromagnetic modes; secondly, these modes may either decay radiatively (enabling light emission) or non-radiatively.

Based on Fermi golden rule, the elastic and the inelastic tunneling rates[39] can be derived. They can be cast in the form:

$$\begin{aligned} \Gamma_{el} &= \frac{2\pi}{\hbar} |t|^2 \int_{\varepsilon_F - eV}^{\varepsilon_F} d\varepsilon \rho_b(\varepsilon) \rho_a(\varepsilon) \\ &\approx \frac{2\pi}{\hbar} |t|^2 \rho_b(\varepsilon_F) \rho_a(\varepsilon_F) eV \end{aligned} \quad (2-26)$$

$$\begin{aligned} \Gamma_{inel} &= \frac{2\pi}{\hbar} |t|^2 \int_{\varepsilon_F - eV + \hbar\omega}^{\varepsilon_F} d\varepsilon \rho_i(\varepsilon + eV) \rho_f(\varepsilon) \\ &\approx \frac{2\pi}{\hbar} |t|^2 \rho_i(\varepsilon_F) \rho_f(\varepsilon_F) (eV - \hbar\omega) \end{aligned} \quad (2-27)$$

where t and t' represent the transfer matrix elements for elastic and inelastic tunneling, respectively. ρ_i and ρ_f are the electronic density of states of the initial state and the final

state. V is the applied voltage, $\hbar\omega$ is the photon energy. Here we assume the electronic density of states varies very slowly with the energy ε in the interval $\varepsilon_F - eV < \varepsilon < \varepsilon_F$. ε_F is the Fermi energy.

To proceed, the probability for an electron to tunnel inelastically is given by:

$$\Gamma_{e-p} = \frac{\Gamma_{inel}}{\Gamma_{inel} + \Gamma_{el}} \approx \frac{\Gamma_{inel}}{\Gamma_{el}} = \left| \frac{t'}{t} \right|^2 \left(1 - \frac{\hbar\omega}{eV} \right). \quad (2-28)$$

The emitted power dP (corresponding to a given emission direction \mathbf{u} and a given polarization state l) can be written as:

$$\begin{aligned} dP^l(\mathbf{u}, \omega) &= \hbar\omega \frac{I}{e} \Gamma_{e-p}(\omega, V) \eta_{ant}^l(\mathbf{u}, \omega) \\ &= \hbar\omega \left| \frac{t'}{t} \right|^2 \frac{I}{e} \left(1 - \frac{\hbar\omega}{eV} \right) \eta_{ant}^l(\mathbf{u}, \omega), \end{aligned} \quad (2-29)$$

where I is the tunnel current through a junction and e is the electron charge. η_{ant}^l is the antenna efficiency which can be defined as:

$$\eta_{ant}^l(\mathbf{u}, \omega) = \frac{P_{rad}^l(\mathbf{u}, \omega)}{\int d\Omega P_{rad}^l(\mathbf{u}, \omega) + P_{nr}^l(\omega)}, \quad (2-30)$$

where P_{rad} and P_{nr} are the radiative power and the non-radiative power, respectively. Concerning the electron-to-plasmon conversion efficiency (for a given emission angle and a given frequency), we simply write

$$\eta_{e-p}^l(\mathbf{u}, \omega) = \left| \frac{t'}{t} \right|^2 \left(1 - \frac{\hbar\omega}{eV} \right) \eta_{ant}^l(\mathbf{u}, \omega). \quad (2-31)$$

Based on Eq. (2-31), the external quantum efficiency of a light emitting tunnel junction has a link with the inelastic tunneling and the elastic tunneling rates as well as the antenna efficiency. It is seen that a higher external light emission efficiency of a tunnel junction is largely determined by the antenna efficiency.

2.4. Discussion and conclusion

In section 2.2 and 2.3, we have introduced two models for light emission in a tunnel junction. The first picture is based on fields radiated by tunneling current fluctuations. With that point of view, the electron to photon conversion efficiency can be enhanced by increasing the local field in the junction characterized by the enhancement factor K . The second illustration is based on the Fermi golden rule by inelastic tunneling electrons. In that point of view, the electron decays by exciting either non-radiative mode or a gap plasmon mode. The contribution to the local density of states of the gap plasmon is thus the primary factor for the design of an efficient emitter. The efficiency appears as the

result of a competition between the contributions to the density of states of the gap plasmon mode on one hand, the non-radiative modes on the other hand.

These two different pictures are not a priori equivalent. To establish a connection between these two visions, we briefly show that the enhancement factor is proportional to the gap plasmon mode contribution to the radiative local density of state.

We start by considering an energy budget in stationary regime of a single antenna illuminated by a plane wave with incident field amplitude E_{inc}^l . By definition of the absorption cross section σ^l of the antenna, the absorbed power is given by

$$P^l = \frac{1}{2} \varepsilon_0 c |E_{inc}^l|^2 \sigma^l(\mathbf{u}, \omega). \quad (2-32)$$

This absorbed power is equal to the power dissipated by the antenna mode, which can be cast in the form:

$$P^l = \kappa V \varepsilon_0 \frac{|\mathbf{E}^l|^2}{2}, \quad (2-33)$$

where κ is the decay rate of the mode energy, V is the mode volume, and \mathbf{E} is the electric field in the resonant antenna. By equating these two quantities, we derive the enhancement factor:

$$|K^l(\mathbf{u}, \omega)|^2 = \frac{c \sigma^l(\mathbf{u}, \omega)}{\kappa V}. \quad (2-34)$$

We now use the relation between the absorption cross-section and the gain $G^l(\mathbf{u}, \omega)$ of the resonant antenna which characterizes the directivity of the emission angular pattern[42].

$$\sigma^l(\mathbf{u}, \omega) = \frac{\lambda^2}{4\pi} G^l(\mathbf{u}, \omega). \quad (2-35)$$

Inserting (2-35) into (2-34), and introducing the antenna quality factor $Q = \frac{\omega}{\kappa}$, we get

$$|K^l(\mathbf{u}, \omega)|^2 = \left[\frac{3}{4\pi^2} \frac{\lambda^3}{V} Q \right] \frac{G^l(\mathbf{u}, \omega)}{6} = F_p \frac{G^l(\mathbf{u}, \omega)}{6}, \quad (2-36)$$

where F_p is the Purcell factor. It is seen that the field enhancement factor corresponding to a specific emission angle at a defined frequency is linked to the radiative LDOS by considering the same emission direction and the same frequency.

In the description of the section 2.3, the magnitude of the matrix element for the inelastic tunneling, in a form of spectral variation, can be expressed in terms of the normalized LDOS (the Purcell factor) [7], so we have:

$$\left| \frac{t'}{t} \right|^2 \propto F_p. \quad (2-37)$$

Essentially, the antenna efficiency η_{ant}^l is linked to the gain factor which can be derived as:

$$\eta_{ant}^l(\mathbf{u}, \omega) = 4\pi G^l(\mathbf{u}, \omega). \quad (2-38)$$

Thus the emitted power is proportional to:

$$dP^l(\mathbf{u}, \omega) \propto 4\pi \hbar \omega \frac{I}{e} F_p G^l(\mathbf{u}, \omega) \left(1 - \frac{\hbar \omega}{eV}\right). \quad (2-39)$$

It is seen that the emitted power is proportional to the radiative LDOS. In a word, it shows the same physics picture as described by Eq. (2-36).

In summary, we have used two different presentations to describe the light emission in a tunnel junction. Based on the fluctuation dissipation theorem, a large field enhancement $|K|^2$ can predict a better out-coupling light emission. Based on the view of the Fermi golden rule for inelastic tunneling electrons, a higher antenna efficiency suggests having a stronger light emission. In general, a resonant nanoantenna is the key element to fulfill these propositions.

Chapter 3

Enhanced SPP generation in the STM configuration

3.1. Introduction

3.2. Model of the SPP generation in the STM configuration

3.2.1. Model of light emission by IET: effective dipole source

3.2.2. Generation of propagating surface plasmon

3.3. Enhanced SPP generation with aid of a single optical antenna

3.3.1. Cylindrical antenna

3.3.2. Nanocone antenna

3.4. Conclusion

3.1. Introduction

The MIM junction formed between a STM tip and a metallic surface has been demonstrated to provide a versatile platform for probing molecules [43, 44], and generating photon emission[45] via inelastic tunneling electrons. It is noteworthy to see an enhanced light emission (10^{-4} - 10^{-3} photons/electron instead of 10^{-6} - 10^{-5}) from the junction between an STM tip and rough polycrystalline silver film[2, 46] as compared to a planar junction. This is attributed to the presence of a localized gap plasmon mode between the tip and the surface. As we have seen, light emission can be considered as an inelastic process taking place in the barrier or as radiation due to fluctuating currents in the barrier. Hence, a simple model consists in introducing a dipole source in the barrier as shown in Fig. 3.1. In such a situation, three main decay channels exist. First, photons can be emitted in the far field. Secondly, SPPs can be generated; they propagate along the air/metal interface. Finally, most of the energy lost by the tunneling electrons is locally dissipated in the STM tip and the metallic surface. This detrimental procedure is similar to the so-called quenching experienced by a fluorescent molecule close to a metal[47]. In the case of inelastic tunneling, the barrier is around 1~3nm so that quenching plays a significant role.

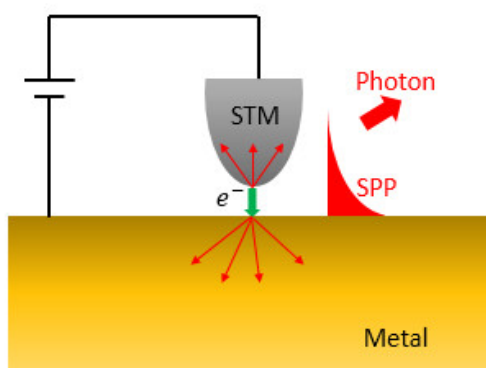


Figure 3.1. The schematic of the energy dissipation in a biased STM-based tunnel junction. Note the red arrows are showing the decay channel of quenching.

Thus, to have a better efficiency of photon or SPP emission for a tunnel junction, it is crucial to beat quenching. The purpose of this chapter is to discuss the design of a nanoantenna with the aim of reducing quenching and enhancing SPP emission by engineering the contribution of the gap modes to the local density of states.

3.2. Model of the SPP generation in the STM configuration

3.2.1. Model of light emission by IET: effective dipole source

Once STM-based junction is voltage biased, a tunneling electron tunnels from the last atom of the tip to the surface of the metallic film. Consequently, the active area is assumed to have the same order of magnitude than the area of a single tunneling channel, which is approximately λ_F^2 where λ_F is the Fermi wavelength. Furthermore, the electric field does not vary appreciably along the normal of the surface. Thus, it is reasonable to consider that the fluctuating current can be modeled by an electric dipole aligned along the electrons flow direction[35].

According to ref[35], the STM tip can be modelled as a nanosphere, as shown in Fig. 3.2, and the gap between the sphere and the metal is set at 2nm. A dipole is put in the middle of the gap and vertically polarized on the axis of the revolution symmetry of the system.

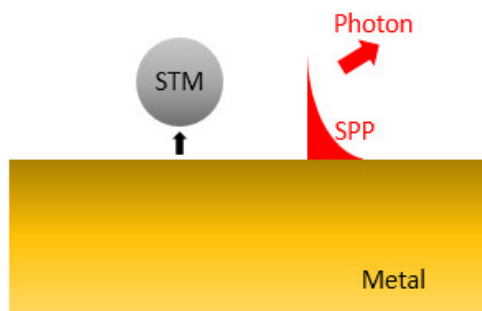


Figure 3.2 Simplified calculation model for light emitting tunnel junction (LETJ) based on the STM configuration. The metal of the film is gold and the conducting material of the STM tip is tungsten.

In Chapter 2, we have pointed out that a better antenna efficiency can create a better SPP emission procedure. Thus, in the following sections, we will mainly concentrate on the antenna designs.

3.2.2. Generation of propagating surface plasmon

Our goal is to compute the emitted propagating SPP power by a vertically polarized point source in the gap between a tungsten sphere and a gold film, as shown in Fig.3.3. We use an aperiodic Fourier modal method (a-FMM) developed in our group in order to compute emission by dipole sources in the presence of body-of-revolution structures [48]. From the calculation of the electromagnetic field, we extract:

- (1) the total power emitted by the source P_T ,
- (2) the non-radiative power P_{nr} (power dissipated in the metal),
- (3) the radiative power P_r (power radiated in the far-field),
- (4) the amplitude A_{spp} of the SPP that propagates horizontally along the gold/air interface.

Energy conservation implies that $P_T = P_{nr} + P_r$. The radiative power P_r and the SPP amplitude A_{spp} are calculated from the near field thanks to a near-to-far field transformation valid both for plane waves and guided modes[49]. Outside the antenna (e.g., outside the sealed box labeled S in Fig. 3.3) and using cylindrical coordinates, the electric field emitted by a point source can be expanded as

$$\mathbf{E}(r, z) = A_{spp} \mathbf{E}_{spp}^+(r, z) + \sum_{\sigma} A_{\sigma} \mathbf{E}_{\sigma}^+(r, z), \quad (3-1)$$

where the last term corresponds to a summation over the continuum of radiation modes of the planar gold/air system. The first term is the part of interest; it corresponds to the field of an outgoing SPP with an amplitude A_{spp} . Note that the fields are independent of the azimuthal angle θ because of the source position and polarization. A vertically polarized dipole located off-axis produces a θ -dependent field and an expansion similar to Eq. (3-1) holds with an additional summation over the azimuthal number m . The SPP amplitude in Eq. (3-1) is calculated by using the mode orthogonality [50],

$$A_{spp} = \frac{1}{N_{spp}} \iint (\mathbf{E}_{spp}^- \times \mathbf{H} - \mathbf{E} \times \mathbf{H}_{spp}^-) \cdot \mathbf{u}_r r d\theta dz = \langle \Phi | \Phi_{spp} \rangle, \quad (3-2)$$

where $\Phi = (\mathbf{E}, \mathbf{H})$ is the total electromagnetic field emitted by the source and $\Phi_{spp} = (\mathbf{E}_{spp}^-, \mathbf{H}_{spp}^-)$ is the field of the ingoing SPP. The normalization coefficient is $N_{spp} = 4i(\varepsilon_d^2 - \varepsilon_m^2)/(\omega\varepsilon_0 k_{spp} \varepsilon_d^{3/2} \varepsilon_m^{3/2})$, with k_{spp} the SPP propagation constant. Since it relies on the orthogonality of the modes supported by the planar system, the integral in Eq. (3-2) is independent of the radial position r and can be calculated over any cylindrical surface outside the antenna.

This formalism allows calculating quantitatively the fraction of light that is emitted into SPPs. It is worth noting that it can be used with any numerical method that is able to compute the total field (\mathbf{E}, \mathbf{H}) emitted by a dipole source. More details on the theoretical formalism can be found in refs[38, 49]. It is important to note that we consider a real metal with a finite conductivity, the modes are not orthogonal in the sense of the Poynting vector, as is usually the case in lossless waveguides. In such an absorbing system, the modes obey

the general unconjugated form of orthogonality [50]. Therefore, the total power (total Poynting vector) carried out by the different modes cannot be expressed as a sum over the Poynting vectors of each mode; interference terms between the different modes appear in the expression of the total power. In the context of SPP propagation along metal surfaces, these interferences have a non-negligible impact, as experimentally demonstrated in[51]. The main practical consequence is that the concept of power carried out by a SPP is less meaningful than in a usual lossless waveguide. However, it is still possible to define the power carried out by SPPs as the Poynting vector associated to the fraction of the total field corresponding to SPPs [first term in Eq. (3-1)]. This modal Poynting vector, integrated over the azimuthal angle θ , is proportional to $\frac{4}{|k_{spp}|} |A_{spp}|^2 \exp(-2\text{Im}(k_{spp})r)$, where the exponentially-decreasing factor corresponds to the SPP attenuation along the interface. Therefore, the quantity $\frac{4}{|k_{spp}|} |A_{spp}|^2$ is a meaningful figure of merit for quantifying the amount of SPP propagating along the metal surface. Finally, we define the power emitted into SPPs as

$$P_{spp} = \frac{4}{|k_{spp}|} |A_{spp}|^2 . \quad (3-3)$$

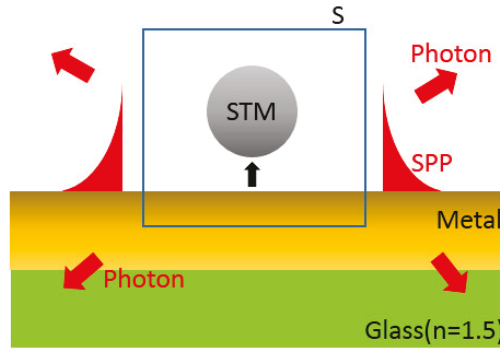


Figure 3.3. Schematic of the calculation principle. We first calculate the total field emitted by the dipole source on the closed box labeled S. In a second step, a near-to-far field transformation provides both the radiative power and the SPP power. We note the gap is air, and the substrate is glass with the refractive index of 1.5.

One final remark: it is important to keep in mind that P_{spp} cannot be used in an energy balance. The sole energy conservation relation that is valid in this problem is $P_T = P_{nr} + P_r$, where the radiative power includes both the power radiated in air and the power leaked into the dielectric substrate (we consider a finite thin metallic film). Therefore, the power P_{spp} carried out by the SPP contains both a radiative part (leakage into the substrate) and a non-radiative part (absorption along the metal surface as the SPP propagates) that cannot be easily separated.

3.3. Enhanced SPP generation with aid of a single optical antenna

3.3.1. Cylindrical antenna

We propose to put a nanorod antenna between the STM tip and the metallic film (thickness=50nm) as shown in Fig. 3.4. The idea is to benefit from an additional emission channel that can compete with the quenching contribution.

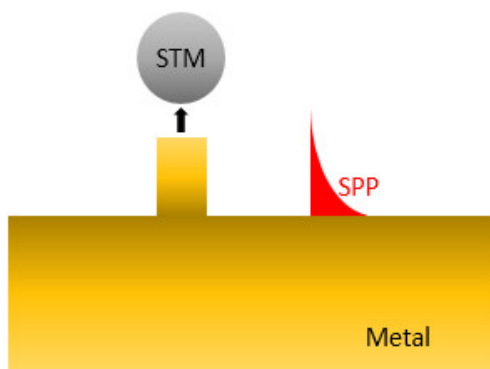


Figure 3.4 Schematic of SPP excitation with aid of a nanocylinder. A vertically polarized dipole source is placed on axis in the center of the gap between a tungsten sphere (model of a STM tip) and a gold nanorod.

To clarify the contribution from an antenna, we need to determine the reference case where no antenna is included. The normalized spectra of total power (LDOS) and the SPP power along the Au/air interface are presented in Fig. 3.5 by varying the diameter of the tungsten sphere. The dielectric function of tungsten is taken from Palik[52], the Au is given by a Drude-Lorentz mode that fits the data tabulated in the ref [53] over the [500-1500] nm spectral range. It is seen that the total LDOS is 5 orders of magnitude bigger than the LDOS in vacuum, and no big difference between different diameters of the tungsten sphere can be obtained. It should be emphasized that this extremely large LDOS corresponds mainly to quenching, i.e., absorption in the metal film and the tungsten sphere localized in a nanoscale volume close to the source. We notice an increase of the LDOS for $\lambda > 700\text{nm}$, which is due to the absorption in the tungsten sphere[38]. In the SPP emission diagram (Fig. 3.5b), a resonant contribution arises from a localized gap plasmon in the case of a bigger tungsten sphere. Thanks to the gap plasmon, the SPP power can be enhanced by one order of magnitude. Thereafter, we prefer to use a smaller tungsten sphere to avoid any resonant plasmonic responses from the tungsten sphere in the spectral range of interest. In the following calculations, we chose to use a 20nm tungsten sphere.

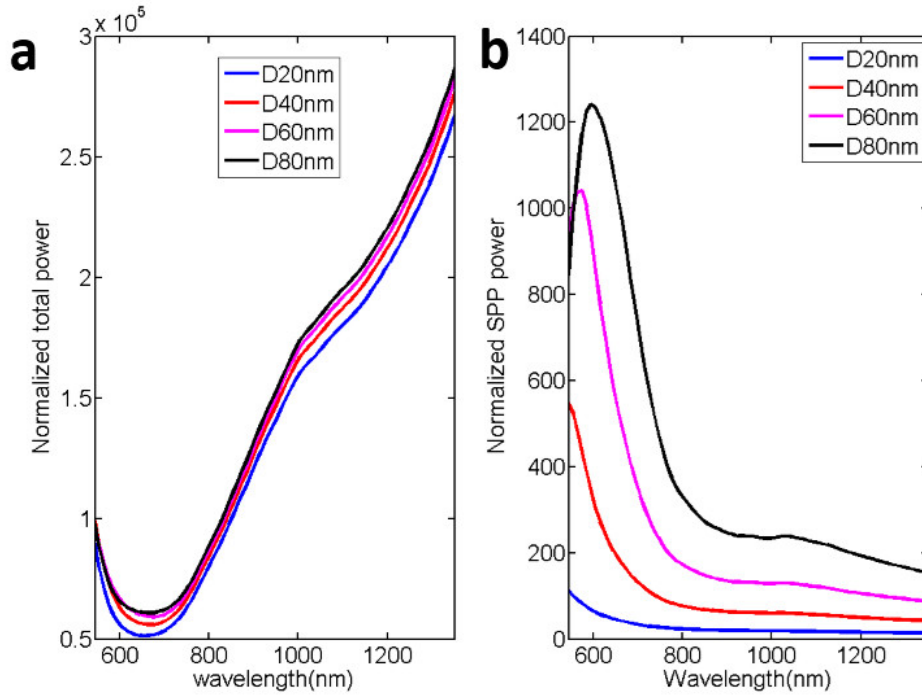


Figure 3.5. (a) LDOS (normalized by the vacuum LDOS) spectra for 4 different diameters of the tungsten sphere, from 20 nm to 80 nm; (b) SPP power (normalized by the vacuum LDOS) for the same diameters of the tungsten sphere.

We now move to study the SPP emission in the presence of an antenna. In Fig. 3.6, a normalized LDOS spectrum is shown for a cylindrical antenna (diameter 39nm and height 72nm) and for a reference case without antenna. We see a small shoulder around 800nm attributed to the antenna mode. It means that, even if the mode contribution to the LDOS is smaller than the quenching, it is not negligible. Therefore, the antenna provides an additional decay channel that can compete with quenching. Consequently, in Fig. 3.6(b), the SPP power at the antenna resonance ($\lambda=800$ nm) is two orders of magnitude larger than the reference. Moreover, the SPP emission spectrum has been deeply tailored by the presence of the antenna and exhibits a narrow peak.

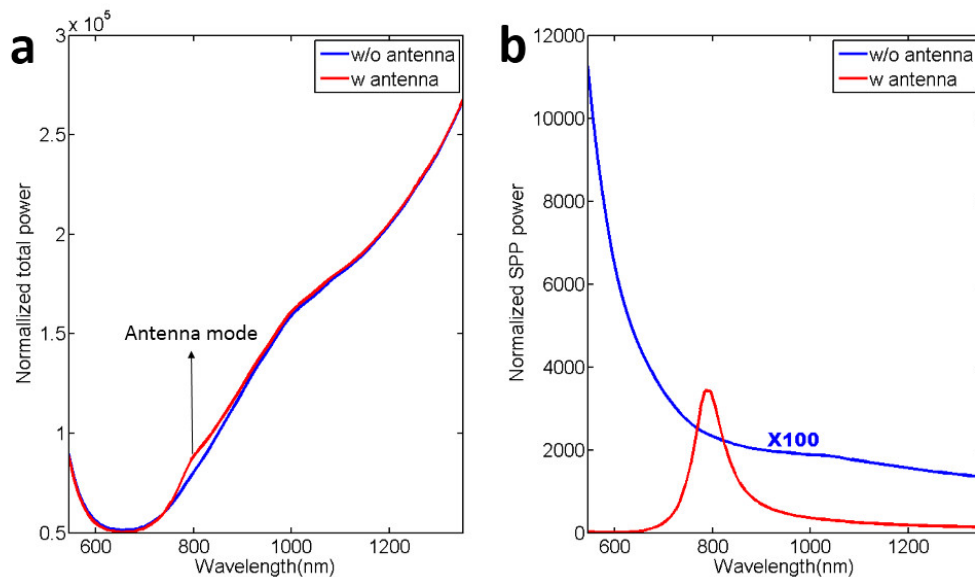


Figure 3.6. (a) Normalized LDOS spectra regarding the case with (red line) and without (blue line) a

nanoantenna; (b) Normalized SPP power spectra with and without antenna. The SPP power without antenna (blue curve) has been multiplied by a factor of 100.

In order to clarify the enhancement mechanism, we plot the electromagnetic field distribution driven by the point source. In Fig. 3.7(a), apart from a strong hot spot where placed in the close vicinity of the source (quenching), the cylinder itself has been lighted, which corresponds to the excitation of the dipole-like mode of the antenna. In contrast, in Fig. 3.7(b), only the hot spot associated to the quenching appears between the tip and the metallic surface.

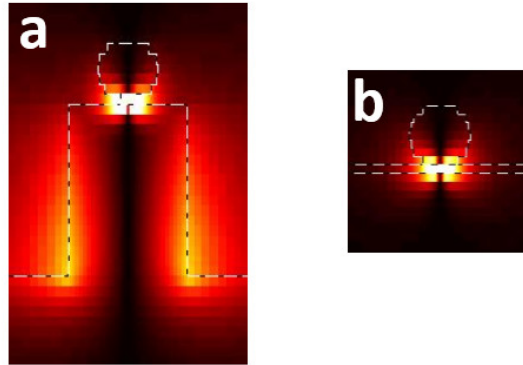


Figure 3.7 (a) Magnetic-field distribution H_y emitted by a dipole source located between a tungsten sphere and a gold nanorod (height =72nm,diameter =39nm) at wavelength of 800nm; (b) Same without the gold nanorod.

We define the SPP excitation efficiency as:

$$\eta_{spp} = \frac{P_{spp}}{P_T}. \quad (3-4)$$

Here we should emphasize that this SPP excitation efficiency is in terms of the antenna SPP emission efficiency. It should not be confused with the electron to plasmon conversion efficiency of a tunnel junction. In Fig. 3.8, we show the SPP excitation efficiency spectra between the cases with an antenna and the reference. Concerning the antenna resonance, we have over two orders of magnitude enhancement, the antenna efficiency can reach up to 4%.

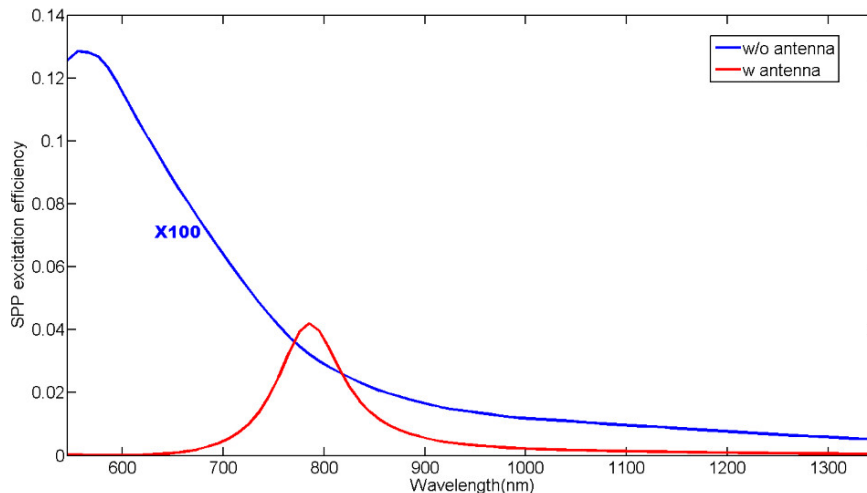


Figure 3.8 SPP excitation efficiency defined by Eq.(3-6). The red curve corresponds to the case with the nanorod antenna (height =57nm, diameter =39nm) and the blue curve shows the result without nanoantenna (The blue curve has been multiplied by a factor of 100).

Finally, we show in Fig. 3.9 the SPP emission spectrum. It can be tuned by varying the aspect ratio of the nanocylinder. We have fixed the diameter of the cylinder at 39nm and used five different heights. In Fig. 3.9a, a redshifted spectrum can be obtained with an increased height of cylinder which agrees well with the behavior of a nanorod resonance frequency as function of the diameter-over-height ratio [54]. In Fig. 3.9b, in the view of SPP excitation efficiency, the efficiencies at the resonance are around 4%, which demonstrates a robust strategy towards a good SPP nanosource.

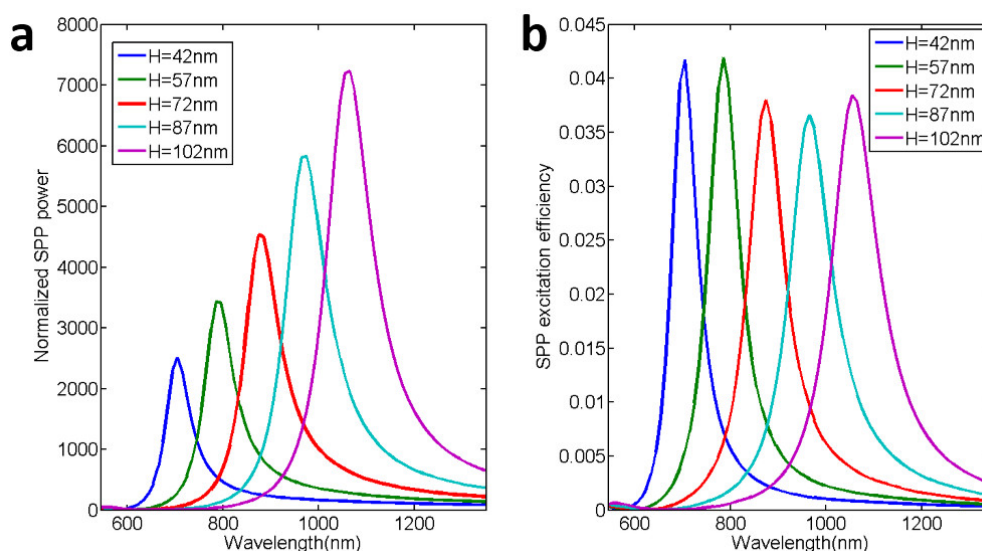


Figure 3.9 (a) SPP power spectra can be controlled by tuning the height of the cylinder (varying from 42 nm to 102 nm) with a fixed diameter (39nm); (b) Corresponding SPP excitation efficiency spectra.

3.3.2. Nanocone antenna

Spontaneous emission by a MIM gap configuration has been fruitfully studied in the past decade. Compared to a gap with a strong facet reflectivity, a tapered nanogap has been proposed to have a lower localized absorption which induces a more efficient radiation[55], as schematically shown in Fig. 3.10.

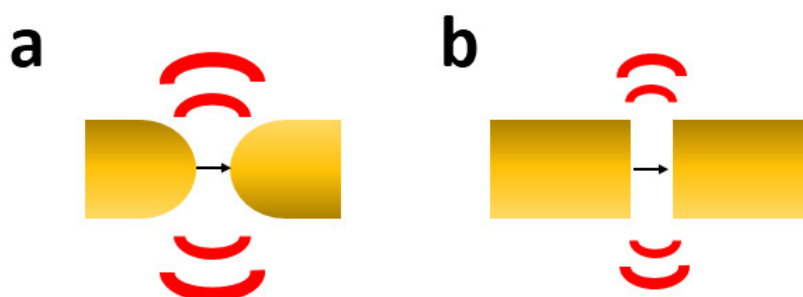


Figure 3.10 Schematic of two different designs of a MIM nanogap with a polarized dipole source in the gap center (a) tapered shape; (b) constant facet shape.

Based on this suggestion, a nanocone antenna below a STM tip can be a good candidate. Good fluorescence enhancement have been reported in references[56, 57]. By simply replacing the cylinder antenna by a nanocone in the STM configuration, a bigger charge

density can be obtained in principle. Thus, the LDOS from the antenna mode can be further increased. To conduct the calculation properly for a nanocone configuration with the cylindrical a-FMM, we make an approximation on the geometry. Instead of a perfect nanocone, we use a staircase approximation of the cone profile with seven superposed cylinders with the same height but with a decreasing diameter. The related slope angle θ , as defined in Fig. 3.11, is conserved.

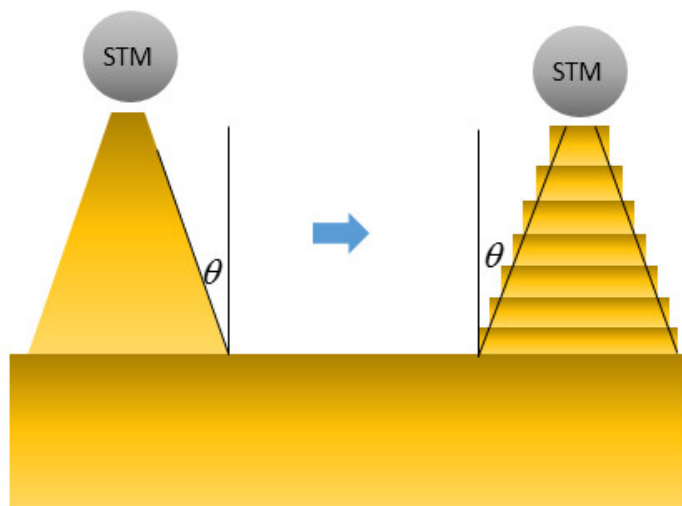


Figure 3.11. The left side show a perfect shape of a nanocone antenna and the right side shows the approximated shape used for the calculations, θ is the slope angle of the nanocone

Thereafter, we evaluate the SPP emission with a nanocone antenna. In Fig. 3.12, we study the impact of a variation of the slope angle θ from 5° to 15° . We have fixed the bottom diameter of the nanocone at 39nm and the height at 57nm. It is seen in Fig. 3.12(a) that the resonant frequency does not depend on the slope angle. By contrast, the generated SPP intensity is increased by a factor of 3 when increasing the angle. Consequently, the SPP excitation efficiency at the resonance, in Fig. 3.12(b), can be boosted up to 16%. In a word, a better enhancement factor can be obtained by using a sharper nanocone. However, in view of fabrication procedure and experiment handling, a sharper cone could add more difficulties. Actually, an angle of 15° is a suitable number to be considered in the future realizations.

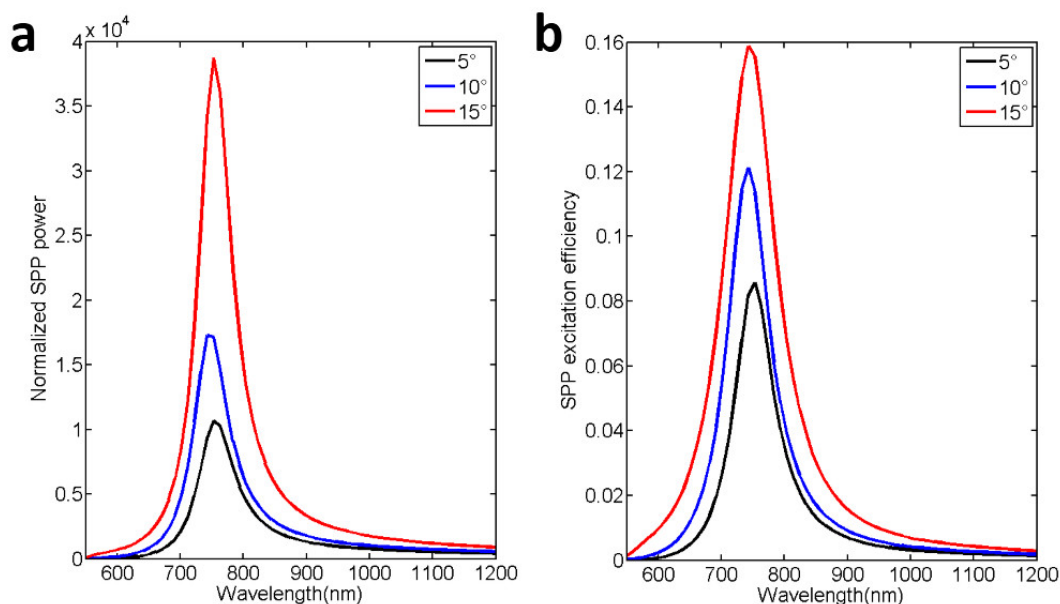


Figure 3.12. (a) Normalized SPP power spectra with 3 different slope angles; (b) Corresponding SPP excitation efficiency spectra.

We now explore the impact of the cone width by varying the bottom diameter and with a slope angle of 15°. As shown in Fig. 3.13(a), a larger diameter produces a blue shift. It is seen in Fig. 3.13(b) that the SPP intensity at the antenna resonance decreases more than one order of magnitude. This is not surprising as the area of the upper disk increases thereby reducing the charge density and therefore the field. Of course, this conclusion strongly depends on the model used in the numerical calculation to represent the cone.

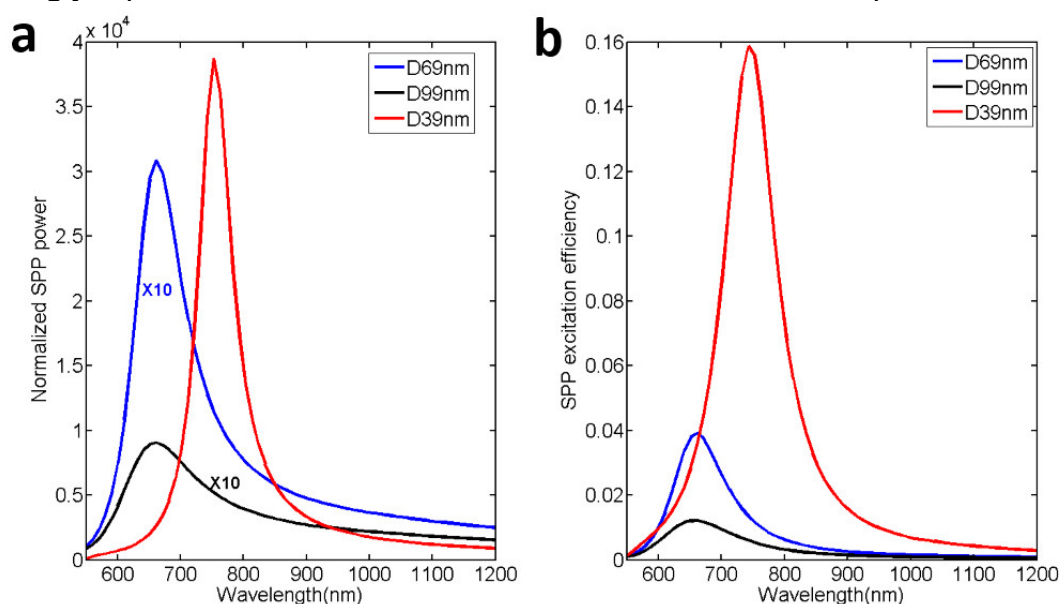


Figure 3.13. (a) Normalized SPP power with 3 different bottom diameters of nanocone; (b) Related SPP excitation efficiency spectra.

Consequently, there is no surprise to see the SPP excitation efficiency suffering a drop (down to 1%) with the diameter of 99nm. In summary, the SPP efficiency using a single nanocone antenna depends critically on the cone geometry.

3.4. Conclusion

In this chapter, we have theoretically demonstrated that an enhanced SPP emission can be produced by putting a metallic nanorod or nanocone between a STM tip and a metallic film. The key idea is to take advantage of an antenna mode with a large Purcell factor to insert an additional decay channel thanks to the antenna. Quantitatively saying, two orders of magnitude SPP emission enhancement can be obtained by using a gold nanorod and almost three orders of magnitude SPP emission enhancement by using a gold nanocone. Since an integrated nanosource is tending to be more practical, it is more interesting to have a fruitful design to reach a better efficiency in a configuration compatible with on-chip integration. In the following chapters, I will focus on an integrated MIM configuration.

Chapter 4

Design of a highly efficient SPP source based on a cylindrical nanopatch antenna

4.1. Introduction

4.2. Mode hybridization and quasi-normal mode formalism

4.2.1. Mode hybridization

4.2.2. Modal formalism for the SPP emission

4.2.2.1. SPP emission with a single-mode antenna

4.2.2.2. SPP emission with a bimode antenna

4.3. Calculation of the nanopatch modes and their characteristics

4.4. Increasing the SPP emission by tuning the refractive index of the environment

4.5. Source position dependent SPP emission

4.6. Conclusion

Appendix: Antenna geometry dependent mode hybridization

4.1. Introduction

In the last chapter, we have discussed a way to improve the SPP generation in a STM configuration by using a single plasmonic antenna mode. This mode has two roles: i) it adds an additional decay channel which can compete with the non-radiative modes (quenching), ii) the antenna mode excites efficiently the SPPs. Hence, emission can be enhanced by two orders of magnitude. However, a STM tip is needed. We now move towards the design of an integrated electrical source. A patch antenna has already been used for tailoring spontaneous emission at nanoscale [58-60]. Intuitively, we can use a nanopatch antenna to launch a SPP by inelastic tunneling electrons. The goal is to improve the antenna efficiency and the emitted power. Thus it requires a strategy to beat quenching in a nanometer size gap. It has been successfully demonstrated that a good photon efficiency can be obtained with a gap around 8~10nm[60, 61]. However, once the gap is on the order of 1~2nm, the high order non-radiative modes (quenching) are usually considered to be dominant. In this chapter, we present a theoretical study of SPPs emission from MIM nanopatch antennas with sub-nm gaps. The specificity of this chapter is to use

quasinormal modes (namely, modes with a complex eigenfrequency accounting for the radiative and non radiative losses). We consider antennas supporting two modes, one serves to increase the local density of states in the barrier gap, the other one is used to efficiently radiate SPPs. A fine control of the coupling between two different modes of the patch antenna allows increasing the SPP emission. We use a rigorous modal formalism to investigate the physical mechanism behind this enhancement[62]. For geometrical parameters where one mode with a large Purcell factor is coupled to a second mode with a good ability to radiate SPPs, the total SPP emission can be largely enhanced. Since our objective is light emission from inelastic electron tunneling, we focus on very small dielectric gaps of 1-2nm. However, it is important to note that, even if it plays a more significant role for thin gaps, the hybridization takes place whatever the thickness of the dielectric gap.

4.2. Mode hybridization and quasi-normal mode formalism

4.2.1. Mode hybridization

We consider a cylindrical patch antenna (Au/dielectric/Au[63]) as shown in Fig. 4.1, the diameter is fixed at 39nm, the thickness of the dielectric spacer is 1nm, the refractive index is 1.45 and the metallic film thickness is 50nm. The system lies over a glass substrate with a refractive index 1.5. The vertically polarized point source is an electrical dipole oriented along the z-axis inserted in the middle of the barrier.

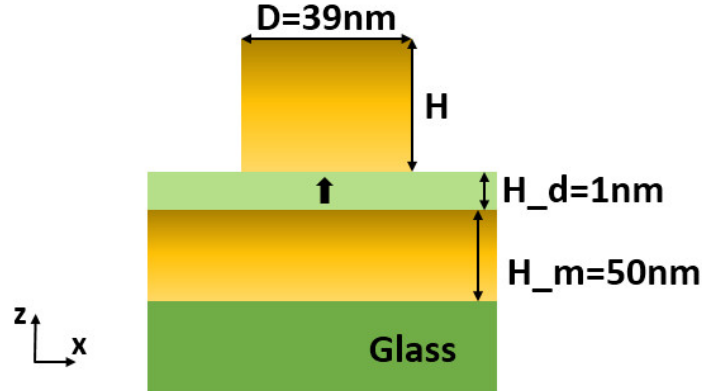


Figure 4.1 Schematic of a cylindrical patch antenna in the X-Z view plane.

We calculate the total emitted power P_T and the power emitted into SPPs P_{spp} as a function of the emitter frequency and the antenna height H . The SPP power is calculated with the procedure described in Chapter 3. The results are plotted in Fig. 4.2. Fig. 4.2(a) shows the SPP power in log-scale and Fig. 4.2(b) shows the SPP efficiency η_{spp} . The SPP power spectrum exhibits two clear resonances; one resonance at $\lambda = 800$ nm that does not vary with the antenna height and a second resonance that redshifts significantly as the antenna height is increased.

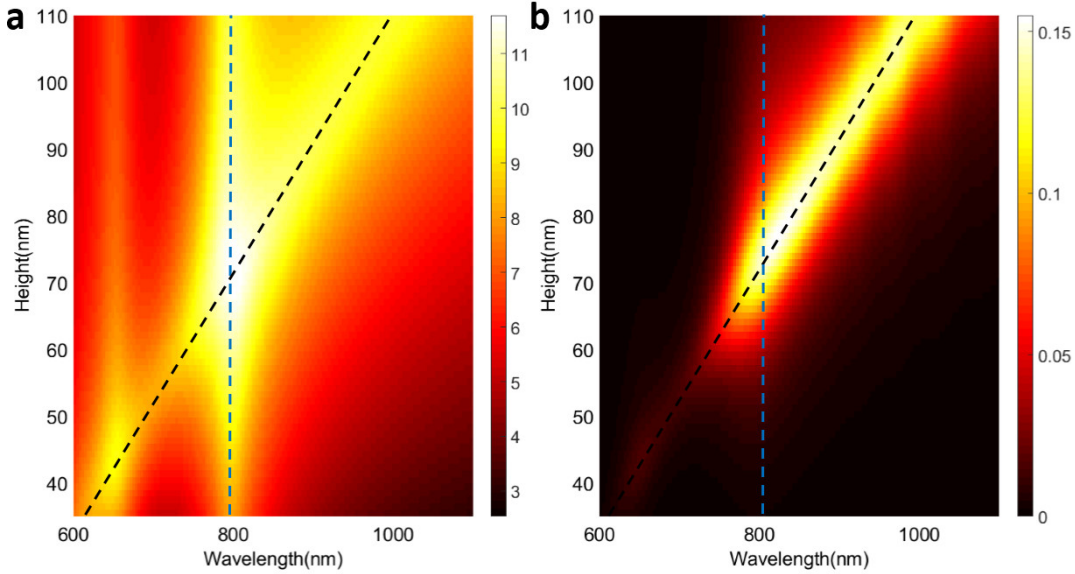


Figure 4.2. (a) Normalized emitted SPP power as a function of the cylinder height and the wavelength. (b) SPP excitation efficiency as a function of the cylinder height and the wavelength. Note that the dashed lines are guides to the eye that follow the resonances.

Both resonances cross at $\lambda = 800$ nm and $H = 72$ nm. Moreover, at the crossing point, the power emitted into SPPs is enhanced by more than one order of magnitude compared to the position where two modes do not overlap. This enhancement is not due to an overall increase of the power emitted by the source. It corresponds to an increase of the SPP efficiency of the antenna, as shown in Fig. 4.2 (b). These two figures evidence that there exist optimum geometries for the nanopatch antenna that optimize the SPP efficiency. As shown by Fig. 4.2(a), the optimum arises from the coupling between two different modes of the antenna. In order to fully understand why the mode hybridization provides an enhancement of the SPP efficiency, we have developed a modal formalism of the SPP emission. Before describing the modal formalism, let us first briefly describe the modes of a cylindrical nanopatch and more particularly the two modes involved in the coupling of Fig. 4.2.

A cylindrical nanopatch antenna supports different eigenmodes. Because of the symmetry of revolution, each mode can be characterized by an azimuthal number m (the electromagnetic field varies as $e^{im\theta}$, with θ the usual angle of cylindrical coordinates). In addition, the eigenmodes of such a nanoparticle-on-mirror system can be sorted in two different families[64]. On the one hand, the gold nanorod alone (far from the mirror) sustains localized plasmonic modes. As the nanorod is brought close to the gold layer, these modes couple to their mirror images. Following the notation used in Ref[64], we refer to the modes resulting from that coupling as *longitudinal antenna modes* and we denote them with the label L_{mn} , with m the azimuthal number and n the mode order. On the other hand, the thin dielectric gap surrounded by metal acts as a transverse channel that supports so-called gap SPPs[65]. Because of reflection at the cylinder edges, the gap SPPs propagate back and forth below the patch and build standing waves when the accumulated phase during one round trip matches 2π [66–68]. We refer to these modes as *transverse gap modes*[64] and we denote them with the label S_{mn} , with m the azimuthal number and n the mode order. In that case, the order n corresponds to the number of nodes (below the patch) of the vertical electric field component.

Mode hybridization in the cylindrical nanopatch is driven by the following selection rule: only modes with the same azimuthal number can couple. Moreover, only modes with

$m=0$ can be excited by a vertically polarized dipole located on the cylinder axis. The antenna height H is the good parameter to discriminate both families of modes. Indeed, the eigenfrequency of the antenna modes strongly varies with the antenna height H whereas the gap modes are almost independent of a variation of H . On the contrary, the diameter D impacts both kinds of resonances. The modes involved in the coupling shown in Fig. 3.3 are the antenna mode L_{01} and the second-order gap mode S_{02} . The fundamental gap mode S_{11} is not excited by the on-axis dipole since its azimuthal number is $m=1$. Its resonance wavelength is $\lambda = 1040$ nm. As illustrated in Fig. 4.3(b), the antenna mode L_{01} sustains a dipole-like charge distribution. The gap mode S_{02} and the gap mode S_{11} hold capacitor-like charge distributions, see Figs.4.3(c)-(d). Fig. 4.3(a) schematically shows the hybridization mechanism between an antenna mode and a gap mode that share the same azimuthal number.

Now that we know which modes are involved in the hybridization that yields the SPP efficiency enhancement, let us describe the modal formalism that we have used to quantify the phenomenon.

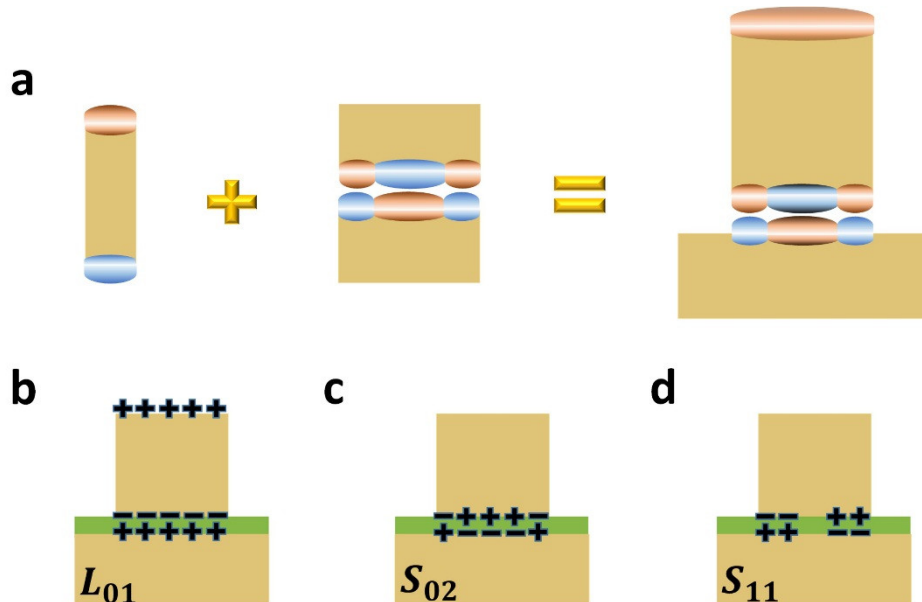


Figure 4.3. (a) Schematic for the formation of the hybrid mode; (b-d) Charge distribution of the L_{01} mode, the S_{02} mode and the S_{11} mode, respectively.

4.2.2. Modal formalism for the SPP emission

Due to non-negligible energy dissipation by absorption and radiation, the eigenmodes of a plasmonic nanoresonator are quasinormal modes (QNMs)[62, 69]. By introducing the QNMs of the system and calculating their excitation coefficients, we can define modal physical quantities such as the Purcell factor, the β -factor, or the modal SPP efficiency. Then, we derive a simple closed-form expression of the total SPP efficiency of the antenna as a function of the modal quantities. This closed-form expression provides (i) design rules to improve the SPP efficiency and (ii) an in-depth interpretation of the SPP efficiency enhancement observed in Fig. 4.2.

Hereafter, we use the modal formalism developed in[62] for photon emission and

extend it to SPP emission. Before deriving the equations in the case of a bimodal system, we first consider the simpler case of a monomode system. If our nanopatch antenna is obviously bimode in the vicinity of the coupling region, it is a single-mode resonator for antenna heights far from the optimum value $H_{opt}=72\text{nm}$. Note also that the single-mode formalism applies to the nanorod antenna studied in Chapter 3.

4.2.2.1. SPP emission with a single-mode antenna

The total electric field \mathbf{E}_T emitted by the dipole source can be expanded as a sum over the QNMs of the system[62, 69]. In a spectral range close to a single-mode resonance, we can separate the mode responsible for the resonance (labeled m) from all the others in the modal expansion

$$\mathbf{E}_T(\mathbf{r}, \omega) = \alpha_m(\omega)\mathbf{E}_m(\mathbf{r}) + \sum_q \alpha_q(\omega)\mathbf{E}_q(\mathbf{r}). \quad (4-1)$$

The excitation coefficients α_q depend only on the mode q and the emitting dipole \mathbf{p} located at \mathbf{r}_0 . They are given by $\alpha_q(\omega) = -\omega\mathbf{p} \cdot \mathbf{E}_q(\mathbf{r}_0) / (\omega - \tilde{\omega}_q)$. Each mode is characterized by a field profile $\mathbf{E}_q(\mathbf{r})$, which is frequency-independent, and a complex eigenfrequency $\tilde{\omega}_q = \omega_q - i\frac{\omega_q}{2Q_q}$. The real part of $\tilde{\omega}_q$ gives the resonance frequency and the imaginary part is related to energy dissipation through the quality factor Q_q .

The total power emitted by the source can also be separated in two contributions[62, 69],

$$P_T(\omega) = P_m(\omega) + P_q(\omega), \quad (4-2)$$

where P_m is the power emitted in the mode of interest and P_q is the power emitted in all the other QNMs. In the case of a plasmonic nanoresonator, it has been shown that the contribution of the higher-order QNMs corresponds mainly to a non-radiative power that is absorbed in the metal in a nanoscale volume close to the source[70]. We associate this contribution to quenching. The total power emitted by the dipole source close to a plasmonic antenna is thus a balance between quenching and the excitation of the antenna mode. Note that, at resonance, the power emitted into the mode defines the Purcell factor,

$$F_p = \frac{P_m(\omega_m)}{P_0} = \frac{3}{4\pi^2} \left(\frac{\lambda_m}{n_d} \right)^3 \text{Re} \left(\frac{Q_m}{V_m} \right), \quad (4-3)$$

with P_0 the power emitted by the same dipole in a bulk material of refractive index n_d , the index of the dielectric material surrounding the emitter. For a QNM, because of energy dissipation, the mode volume V_m is a complex quantity[62, 69]. We define also the β -factor, which gives the fraction of the total emission that goes into the mode,

$$\beta = \frac{P_m}{P_T} = \frac{P_m}{P_m + P_q}. \quad (4-4)$$

We use here the usual definition of the β -factor used in cavity quantum electrodynamics.

However, there is a crucial difference between a photonic microcavity and a plasmonic nanocavity. In the first case, the fraction of the emission that is not funneled into the mode is of the same order as the bulk emission and P_q/P_0 is usually assumed to be equal to unity[71, 72]. In contrast, in the case of a plasmonic cavity, P_q corresponds to quenching and, if the source is located at sub-10-nm distances from the metal, $P_q/P_0 \gg 1$. *In other words, the β -factor is extremely small except if the Purcell factor is large enough to compete with quenching.*

Let us now define the modal SPP power and the modal SPP efficiency, which allows quantifying the ability of a given mode to radiate SPPs. Since Eqs. (3-1) and (4-1) are linear, the total SPP amplitude is the sum of all SPP amplitudes provided by each mode. The modal SPP amplitude A_{spp}^m , i.e., the fraction of the SPP amplitude that is solely due to mode m , is given by

$$A_{spp}^m = \alpha_m(\omega) \langle \Phi_m | \Phi_{spp} \rangle, \quad (4-5)$$

with the bracket notation introduced in Eq. (3-2). From the modal SPP amplitude, we can define the SPP power that is due to mode m as[38]:

$$P_{spp}^m = \frac{4}{|k_{spp}|} |A_{spp}^m|^2, \quad (4-6)$$

and the modal SPP efficiency as

$$\eta_{spp}^m = \frac{P_{spp}^m}{P_m}. \quad (4-7)$$

We now make an important assumption. Since the higher-order modes are highly confined around the antenna and the overlap integral in Eq. (4-5) is calculated outside the antenna, we assume that only the mode m responsible for the resonance contributes to SPP emission. In other words, $A_{spp}^q \approx 0$ for $q \neq m$ and we neglect them. Therefore, we have the following approximate relation

$$P_{spp} \approx P_{spp}^m. \quad (4-8)$$

With this approximation, the antenna SPP efficiency can be easily expressed as a function of the modal SPP efficiency and the β -factor of mode m ,

$$\eta_{spp} = \frac{P_{spp}}{P_T} \approx \frac{P_{spp}^m}{P_T} = \beta \eta_{spp}^m. \quad (4-9)$$

Equation (4-9) is a central result. It evidences that the SPP efficiency of a single-mode antenna close to resonance is simply the product of the β -factor (the probability of excitation of the antenna mode) and the modal SPP efficiency (the probability that the mode radiates SPPs). The physical meaning of this equation is clear. The dipole source has

two emission channels, the mode and the quenching. Since the quenching is purely non-radiative, the sole possibility to efficiently emit SPP is to use a mode with two properties: i) a large Purcell factor that can compete with quenching and ii) a good modal SPP efficiency.

4.2.2.2. SPP emission with a bimode antenna

In the case of a resonant antenna that supports two modes in the spectral range of interest, we develop the same reasoning as in the previous section, except that the total field and the total emitted power are separated in three contributions,

$$P_T(\omega) = P_1(\omega) + P_2(\omega) + P_q(\omega), \quad (4-10)$$

with P_1 the power emitted into mode 1, P_2 the power emitted into mode 2, and P_q the quenching (contribution of all the higher-order QNMs). We then define two different β -factors, $\beta_1=P_1/P_T$ and $\beta_2=P_2/P_T$. We assume that the SPP generation is solely due to modes 1 and 2 (we neglect the contribution of higher-order QNMs) and we define A_{spp}^1 and A_{spp}^2 according to Eq. (4-5). The total SPP power is then given by

$$P_{spp} \approx P_{spp}^1 + P_{spp}^2 + P_{12}. \quad (4-11)$$

P_{12} is a cross term due to both modes,

$$P_{12} = 2 \operatorname{Re}(A_{spp}^1 A_{spp}^{2*}). \quad (4-12)$$

The cross power P_{12} results from the interference between both modes. The existence of this term is a consequence of absorption. The absorbed power in the metal depends on the induced currents in the metal which are due to both modes. When adding the fields of the two modes, they may interfere constructively or destructively. If the fields interfere destructively (respectively constructively), the total field is reduced and the Joule effect is reduced (respectively enhanced). Hence, the cross power can be either negative or positive. We will see that the interference term is not negligible and plays an important role when both modes are hybridized. Finally, the total SPP efficiency can be written as

$$\eta_{spp} = \frac{P_{spp}}{P_T} \approx \beta_1 \eta_{spp}^1 + \beta_2 \eta_{spp}^2 + \frac{P_{12}}{P_T}. \quad (4-13)$$

In summary, the modal formalism emphasizes three important parameters.

- (1) The β -factor, which is the fraction of the total emission that is funneled into a given mode.
- (2) The modal SPP efficiency η_{spp}^m , which characterizes the ability of a given mode to radiate SPPs.
- (3) If the resonant antenna supports several modes in the spectral range of interest, the

interference between the modes must be considered. The interference phenomenon is especially important when the modes spectrally overlap, as it is the case when they are coupled, see Fig. 4.2.

4.3. Calculation of the nanopatch modes and their characteristics

In order to understand the increase of SPP emission observed in Fig. 4.2, we have calculated the antenna mode L_{01} and the gap mode S_{02} as well as their important characteristics, Purcell factors, β -factors, and modal SPP efficiencies η_{spp}^m . Since the fundamental gap mode S_{11} has been used in the literature for photon emission, especially with nanocube-on-mirror systems [61, 73], we have also calculated this mode, which can only be excited with an off-axis source.

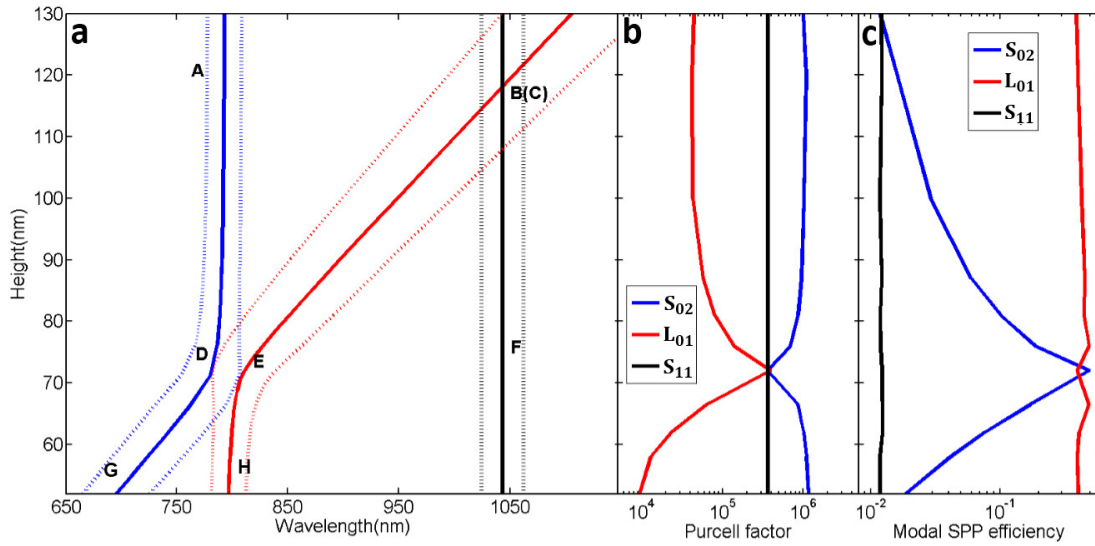


Figure 4.4, (a) The resonant wavelengths of the different modes are tracked in solid lines by varying the height of the cylinder. The distance between the dashed lines along the solid line are showing the mode linewidths; it is seen that the antenna mode has a large spectral width due to radiative losses which increase with the antenna height H . (b-c) Purcell factor and modal SPP efficiency at the resonant wavelength as a function of the cylinder height for the antenna mode L_{01} , the gap mode S_{02} and the gap mode S_{11} .

Figure 4.4 gathers our main results for a fixed diameter of the nanocylinder ($D = 39\text{nm}$) and a fixed thickness of the dielectric gap ($h_d = 1\text{nm}$). We have calculated the three modes the antenna mode L_{01} , the gap mode S_{02} , and the gap mode S_{11} as a function of the cylinder height H . Figure 4.4(a) shows the variation of the real part of the eigenfrequencies (solid curves) together with the variation of the mode linewidths (dashed curves). As the cylinder height is increased, the antenna mode L_{01} is largely redshifted while the frequencies of the gap mode S_{02} and the gap mode S_{11} remain almost unchanged. For such a small gap, the coupling between the antenna mode L_{01} and the gap mode S_{02} results in an anti-crossing of the resonance frequencies for a cylinder height $H = 72\text{ nm}$. On the other hand, a crossing can be observed between the antenna mode L_{01} and the gap mode S_{11} . This behavior, that is due to different mode azimuthal numbers,[64] occurs around $\lambda = 1040\text{ nm}$ with a cylinder height $H = 120\text{ nm}$. The branches labeled A-E-H, B-D-G and C-F represent respectively the gap mode S_{02} , the antenna mode L_{01} and the gap mode S_{11} .

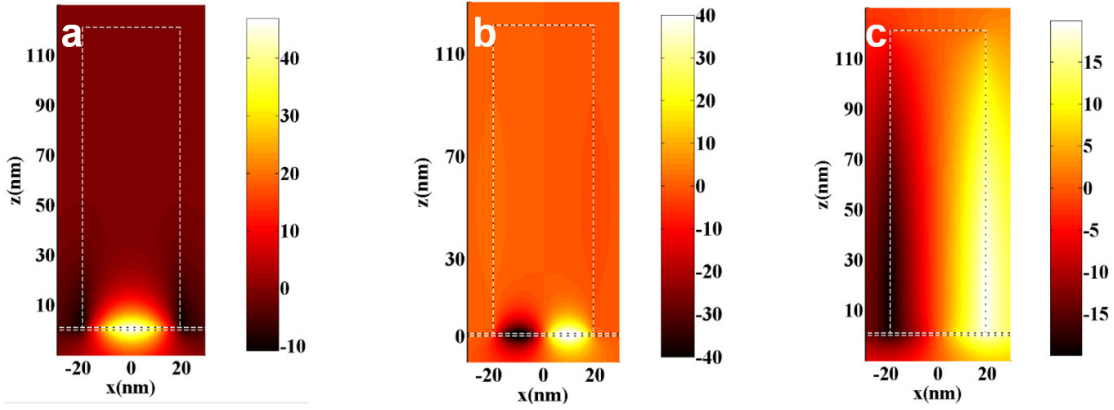


Figure. 4.5 (a-c). Field distributions $\text{Im}(H_y)$ (x - z plane) $H=120$ nm. (a) The gap mode S_{11} . (b) The gap mode S_{02} with mode volume of $(7.0842 \times 10^{-6} - 2.7028 \times 10^{-7}i) \left(\frac{\lambda}{n}\right)^3$. (c) The antenna mode L_{01} with mode volume of $(6.736 \times 10^{-5} + 9.4794 \times 10^{-6}i) \left(\frac{\lambda}{n}\right)^3$.

We now show the field distribution for the two particular heights corresponding to the anticrossing at $H=72$ nm and the crossing at 120nm. We plot in Fig. 4.5(b) and Fig. 4.5(c), the magnetic field distributions (y component, H_y) of the gap mode S_{02} and the antenna mode L_{01} for $H=120$ nm. As expected, the fields are confined either in the gap or in the antenna. No coupling is observed between these two modes in agreement with the fact that there is no anticrossing. In addition, the gap mode S_{11} also presents a gap mode profile, see Fig. 4.5(a).

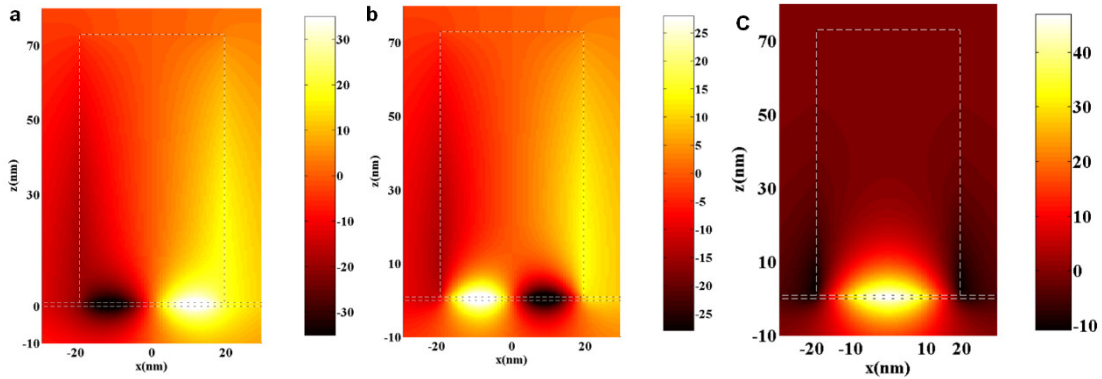


Figure. 4.6 Magnetic field ($\text{Im}(H_y)$, x - z plane) distribution. $H=72$ nm. (a) The antenna mode L_{01} mode with the mode volume of $(9.3368 \times 10^{-6} - 6.6549 \times 10^{-6}i) \left(\frac{\lambda}{n}\right)^3$. (b) The gap mode S_{02} with the mode volume of $(7.0842 \times 10^{-6} - 2.7028 \times 10^{-7}i) \left(\frac{\lambda}{n}\right)^3$. (c) The gap mode S_{11} .

We now plot the magnetic field for the height $H=72$ nm where we have observed an anticrossing between the modes S_{02} and of L_{01} . It is seen in Fig. 4.6(a-b) that both magnetic-field distributions of the gap mode S_{02} and of the antenna mode L_{01} become a mixture between a gap mode and an antenna mode. Note also that the field profile of the gap mode S_{11} remain the same as in Fig. 4.5(a).

The figures have shown that the gap modes are confined so that their mode volumes are expected to be smaller than for the antenna modes. This suggests that the Purcell factor of the gap mode is large. Furthermore, the radiative losses of the antenna mode are expected to be larger than for the gap mode so that the Q factor is lower. In summary, the gap modes are expected to have a large Purcell factor. We show in Fig. 4.4b that indeed, the

Purcell factor is larger for gap modes than for antenna modes. The key observation in Fig. 4.4(b) is that at $H = 72\text{nm}$, the hybrid mode retains a large Purcell factor ensuring that it can be efficiently coupled to the emitter.

We now turn to the SPP modal efficiency and we seek a large efficiency. Fig. 4.4(c) shows the modal SPP efficiencies as a function of the antenna height H . We observe that the antenna mode L_{01} has a high modal efficiency around 40% for all values of H . By contrast, the gap mode S_{11} has a low efficiency on the order of 1%. However, the gap mode S_{02} benefits from the hybridization and its efficiency reaches essentially the antenna mode efficiency around 40%.

In summary, at $H=72\text{nm}$, the hybridized mode retains the best properties of both gap mode and antenna mode: a large Purcell factor and a large modal efficiency.

Finally, we discuss the role of the parameter β introduced in section 4.2. This quantity which is the fraction of power emitted into a given mode, can be related to the mode Purcell factor $F_p = P_m/P_0$. It can be shown that:

$$\beta = \frac{F_p}{F_p + P_q / P_0} \quad (4-14)$$

It is seen that if the Purcell factor is larger than the quenching rate, the β -factor approaches 1. We plot the quantity β in Fig. 4.7 on the resonance as the height H varies.

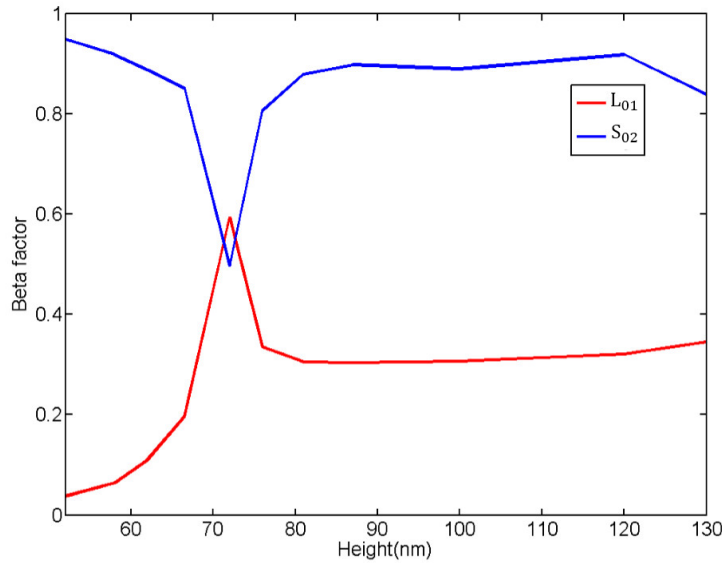


Figure. 4.7. β -factors at resonance calculated as a function of the antenna height for the antenna mode L_{01} and the gap mode S_{02} . Note at the optimal height, the resonant wavelength of the antenna mode L_{01} and the gap mode S_{02} are not exactly the same wavelength even they are very close.

Finally, to clarify the balance between the contribution of the hybrid modes and the quenching, we represent the β -factor of each mode in Fig. 4.7 as a function of the antenna height. The β -factor of the gap mode S_{02} is around 0.9 except close to $H=72\text{nm}$. It means that, thanks to its extremely large Purcell factor of the order of 10^6 , the gap mode S_{02} dominates over the quenching. On the other hand, the β -factor of the antenna mode L_{01} is around 0.3 except close to 72nm. It means that, even if the Purcell factor is large (of the order of 4×10^4), it is ‘only’ of the same order of magnitude as the quenching.

The previous discussion has been based on the analysis of the fields using the expansion over modes described in Eq. (4-1). Despite the reduce number of modes used, the model can be very accurate as is now shown. We report in Fig.4.8 the total power emitted by the

source (Fig. 4.8a) and the SPP power emitted by the source (Fig. 4.8b). We compare two models: the modal technique and an exact numerical calculation. It is seen that the agreement is very good confirming that the analysis based on the interplay between modes is a valid picture.

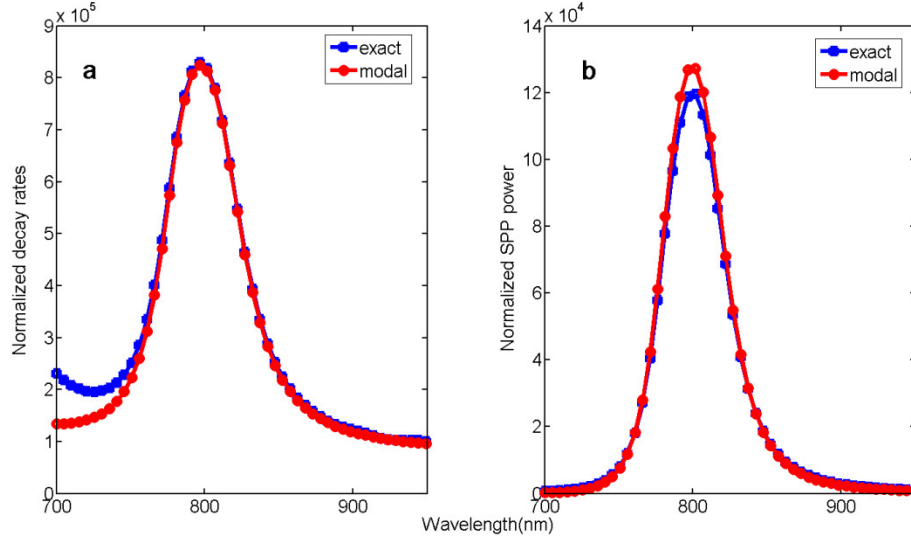


Figure. 4.8. Comparison between the bimode formalism and exact numerical calculations based on the aperiodic Fourier model method with an antenna height of 72nm. (a) Normalized total power predicted by the modal formalism (red dots line) and the calculated exactly with the full Green tensor (blue dots line); (b) Normalized SPP power predicted by the modal formalism (red dots line) and the exact calculation (blue dots line).

In summary, we have seen that a hybrid mode can take advantage of the large Purcell factor due to the confinement of the gap mode and of the large modal efficiency due to the antenna mode.

4.4. Increasing the SPP emission by tuning the refractive index of the environment

It is known that optical properties of plasmonic structures can be modified by coating them with transparent layers [74]. Here we explore how to modify the SPP generation by tuning the refractive index of the host medium of the patch antenna. We have computed photon emission efficiencies and SPP emission efficiencies as a function of the refractive index of the host medium. The results obtained with the hybrid mode are plotted in Fig. 4.9. The power emitted into the far-field normalized by the total emitted power is represented by crosses. The SPP efficiencies are represented by dots. We have considered two cases: an antenna with a gap thickness of 1 nm and a diameter of 39nm, and antenna with a gap thickness of 1.5nm and a diameter of 56nm. All the SPP efficiencies and photon efficiencies are computed from the resonant peak of its corresponding hybrid mode in Fig. 4.10. It is clearly seen that SPP efficiency increases when the nano-patch is embedded in a medium with a larger refractive index. By contrast, the photon emission efficiency decreases. For example, with a gap of 1.5nm, the SPP efficiency at resonance is around 37% in a host medium with a refractive index of 2.8, whereas its photon emission efficiency drops down to 5%. Hence, increasing the refractive index is a remarkable parameter to control the ratio between photon emission and SPP emission. In summary, for

an air-metal interface, the power emitted in air is roughly equal to the power emitted into SPPs. However, when emitting into a medium with refractive index of 1.5, the fraction emitted into plasmons increase significantly.

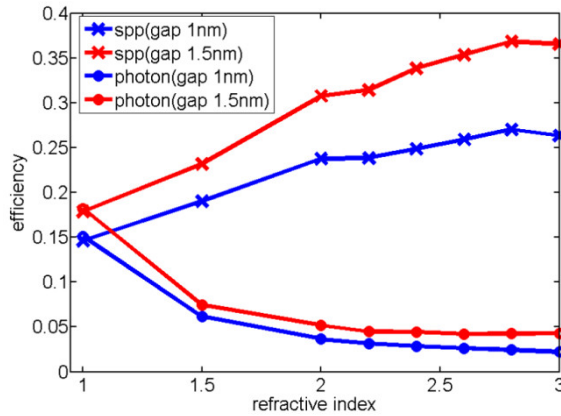


Figure. 4.9 Impact of the refractive index of the host medium on the SPP efficiencies (crosses) and photon emission efficiencies (dots). The values of the efficiencies are selected from the resonant peak of the hybridized mode, see Fig. 4.10. The blue curve corresponds to the gap thickness of 1nm and the red one corresponds to the gap of 1.5nm.

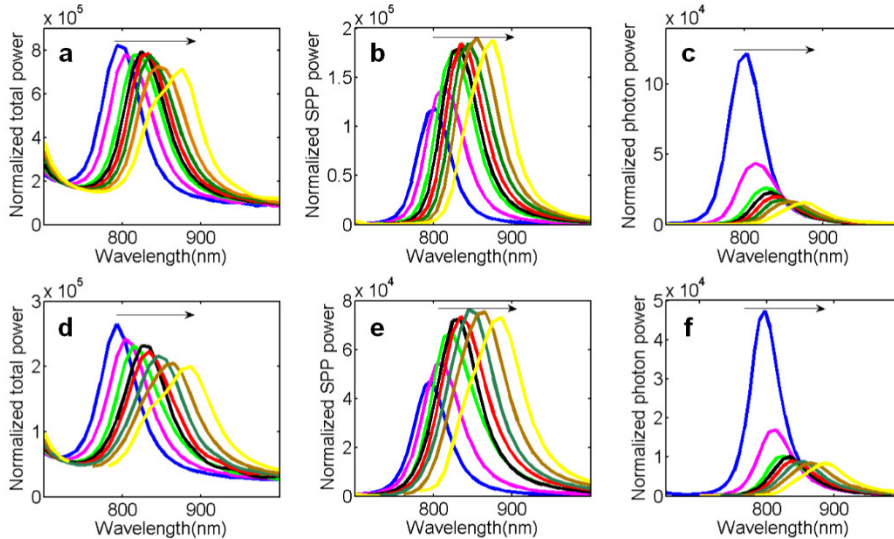


Figure. 4.10. Total power spectra, SPP emission spectra, and the photon power spectra for increasing values of the refractive index of the host medium (the increment direction follows the arrow direction). (a-c) For a gap thickness of 1nm and a diameter of 39nm. (d-f) For a gap thickness of 1.5nm and a diameter of 56nm. Each curve is plotted for the optimal antenna height (for the gap 1nm, the cylinder height decreases from 72nm to 12nm corresponding to a increased refractive index of host medium from 1 to 3; for the gap 1.5nm, the cylinder height decreases from 82nm to 13nm corresponding to a increased refractive index of host medium from 1 to 3) i.e., at the optimal coupling between the gap mode S_{02} and the antenna mode L_{01} .

We plot in Fig. 4.10 the total power, the SPP power and the photon power as a function of frequency for different refractive index. The purpose of this graph is to illustrate the spectral changes in the emission due to the modification of the refractive index. As the refractive index increases, the spectrum redshifts. As seen before, the SPP power increases whereas the photon power decreases.

Finally, we explore the non-radiative efficiency spectra (defined by the non-radiative power over the total power). We show in Fig. 4.11 how it changes as the refractive index of the host medium changes. Here again, we consider the optimal hybrid-coupling mode. It is seen that a larger refractive index environment increases the non-radiative absorption.

This is fully consistent with the decrease of the photon efficiency. In a word, increasing the refractive index surrounding environment, allows increasing the efficiency of the SPP generation.

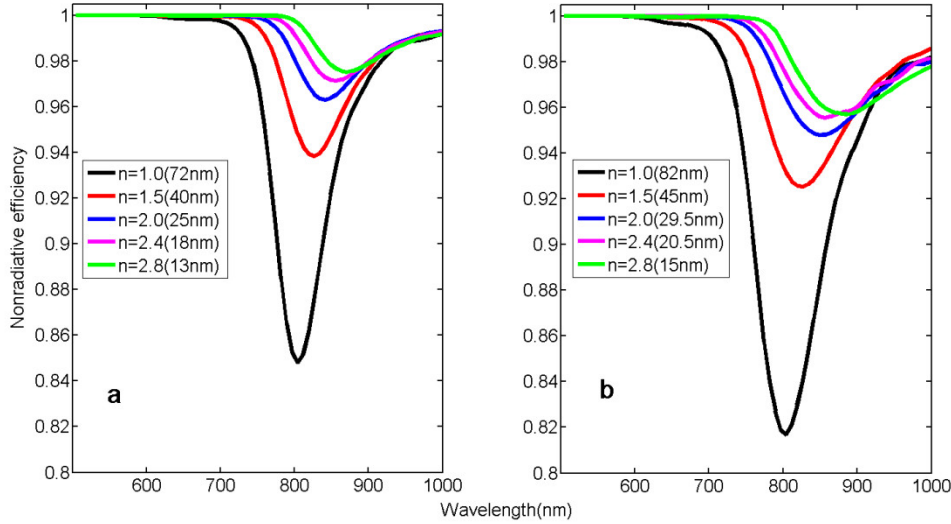


Figure 4.11. The nonradiative efficiency spectra are shown for different values of the refractive index of the host medium from 1 to 2.8. (a) The spectra of optimal structures with a gap of 1nm and an antenna diameter of 39nm; (b) The spectra of optimal structures with a gap of 1.5nm and an antenna diameter of 56nm.

4.5. Source position dependent SPP generation

In previous sections, we have discussed the mode hybridization for the SPP generation where a point source is inserted in the center of the gap on axis. In practice, the point source can be anywhere inside the gap. Thus it is interesting to investigate the SPP generation by varying the source position inside the gap. In order to make an estimation of the influence of the position off-center, we consider three cases with a distance to the center equal to $R/4$, $R/2$, $3R/4$ where R is the radius of the cylinder.

We start by calculating the LDOS spectra for the different positions ($D=39\text{nm}$, $H=72\text{nm}$ and $\text{gap}=1\text{nm}$). We observe in Fig. 4.12 a peak at 1040nm which was not observed for a source in the center. It corresponds to the gap mode S_{II} . It is seen that this mode takes a larger value close to the edge. By contrast, the hybrid mode at 800nm is maximum in the center and decays when approaching the edge.

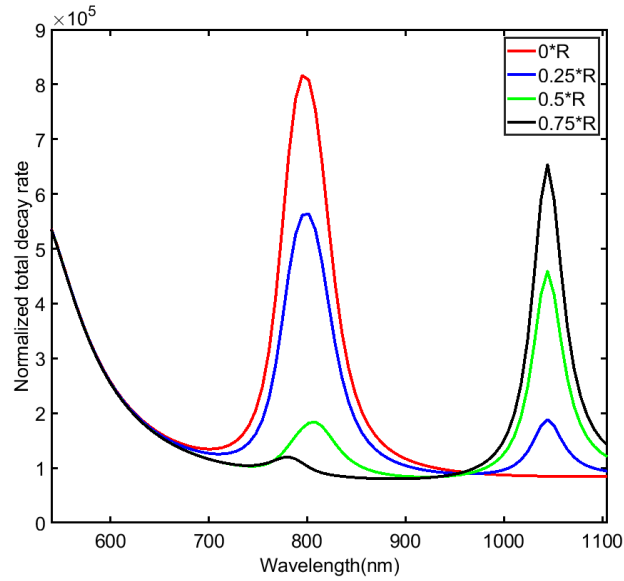


Figure. 4.12 Spectrum of the normalized total emitted power for different positions of the dipole source from the center to the edge.

We now study the SPP emission spectrum shown in Fig. 4.13. The quantity plotted is the total power emitted in the SPP divided by the total power by a dipole in vacuum. It is seen that the power emitted by the hybrid mode decreases when the source approaches the edge of cylinder, and the SPP intensity of the gap mode S_{II} slowly increases. This is in agreement with the trends observed in the LDOS. A remarkable feature is the difference of power emitted by the hybrid mode and the gap mode S_{II} . This is a clear indication of the importance of the hybridization with the antenna mode to couple to the SPP.

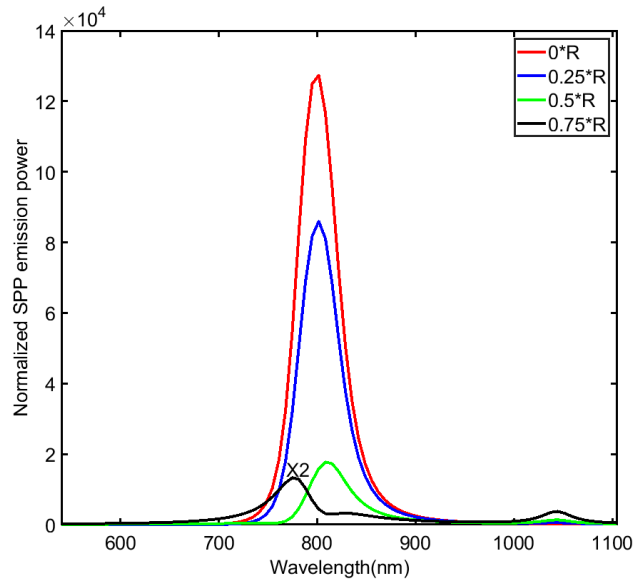


Figure 4.13 Spectrum of the normalized SPP power spectra for different positions of the dipole source from the center to the edge. Note that the black curve has been multiplied by a factor of 2.

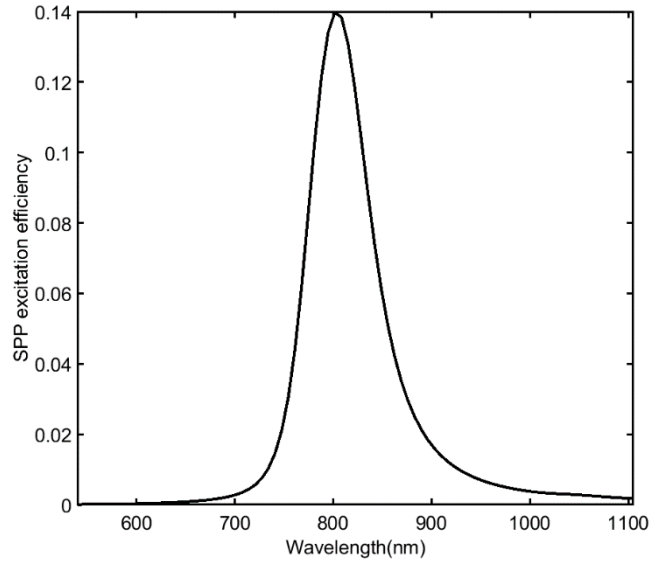


Figure 4.14. Averaged SPP efficiency spectrum.

Finally, we show in Fig. 4.14, the SPP efficiency spectrum averaged over four different source positions. It shows that the hybrid-coupling mode provides the leading contribution. The peak SPP efficiency is near 14%, over one order of magnitude larger than what is observed at 1040nm for the gap mode S_{II} .

In summary, mode hybridization appears to be a promising procedure to enhance SPP emission.

4.6. Conclusion

In this chapter, we have presented a theoretical study of surface plasmon polaritons (SPPs) emission from MIM nanopatch antennas with sub-nm gaps. The originality of our approach is to use a formalism introduced in ref.[62] to analyse the contribution of the different modes of the antenna. The key result of this chapter is the identification of a hybrid mode resulting from the strong coupling between a gap mode that yields a large contribution to the LDOS and an antenna mode that is able to efficiently couple to SPPs. We found that the total SPP emission can be largely enhanced. This hybridization effect takes place whatever the thickness of the dielectric gap. The optimal geometry at a working wavelength of 800 nm (nanocylinder diameter 39 nm and height 72 nm, dielectric gap thickness of 1 nm) provides i) over two orders of magnitude enhancement for the SPP emission and ii) a SPP efficiency of 15%. Furthermore, we have shown that the antenna emits as many photons than plasmons when the surrounding medium is air. However, when increasing the refractive index of the surrounding medium, more power is emitted into plasmons and the plasmonic efficiency can be improved up to 30% with a gap of 1nm at working wavelength around 800nm.

Appendix:

Antenna geometry dependent mode hybridization

We investigate the impact of the cylinder diameter and the gap thickness on the mode hybridization and the SPP emission enhancement. First, let us study the modification of the coupling strength between the antenna mode L_{01} and the gap mode S_{02} by varying the cylinder diameter and using a fixed gap thickness of 1.5nm.

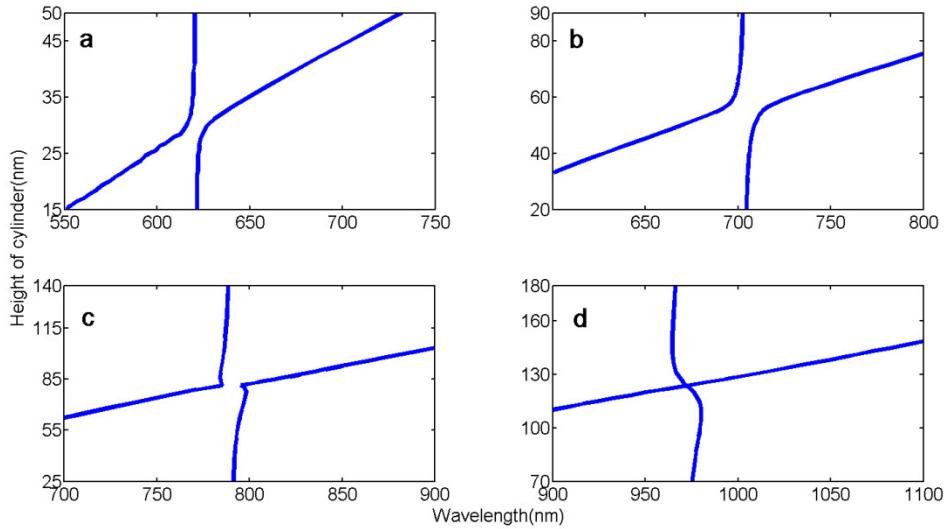


Figure A.1. Impact of the cylinder diameter on the coupling between the antenna mode L_{01} and the gap mode S_{02} . The real part of the eigenfrequencies are represented as a function of the cylinder height. Each figure corresponds to a different cylinder diameter of 25nm (a), 40nm (b), 56nm (c) and 90nm.

The variation with the cylinder height of the resonant wavelengths corresponding to the antenna mode L_{01} and the gap mode S_{02} are illustrated in Fig. A.1 for different values of the cylinder diameter. By choosing a diameter of 25nm, 40nm, 56nm and 90nm, it allows tuning the gap mode S_{02} from 615nm, 710nm, 790nm to 970nm. Varying the antenna height leads to an anti-crossing of the resonance frequencies in the first three cases and to a crossing in the case of the largest diameter. A splitting of 33meV, 51meV and 25meV is obtained from the figure (a) to the figure (c). Because the coupling strength depends on the cavity loss and the mode volume, it is interesting to point that a lower quality factor of the gap mode S_{02} (corresponding to a higher resonance frequency, as shown in Fig. A.2(a-c)) and a bigger mode volume (corresponding to a bigger diameter) lead to a smaller coupling strength. Thus, it explains the optimal mode splitting in Fig. A.1(b). In Fig. A.2(d), the branch of the gap mode S_{02} and the branch of the antenna mode L_{01} are no more crossing at the optimal coupling position, which suggests a lower coupling strength.

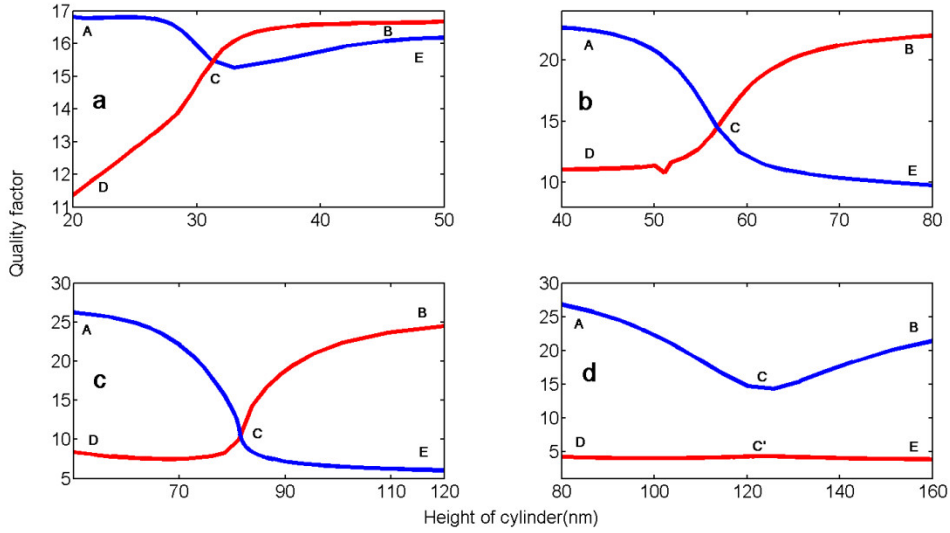


Figure A.2. Quality factors of the L_{01} and S_{02} modes as a function of the cylinder height with a fixed gap thickness of 1.5nm. Each figure corresponds to a different cylinder diameter of 25nm (a), 40nm (b), 56nm (c) and 90nm (d). (a-c) The curve A-C-B and the curve D-C-E are show the evolution of the S_{02} mode and the L_{01} mode, respectively. (d) The curve A-C-B represents the S_{02} mode and the curve D-C'-E represents the L_{01} mode.

In parallel, we plot the total SPP efficiency spectra in Fig. A.3. We compare the spectrum of the optimal geometry to the spectrum of a reference geometry with the same resonance frequency (S_{02} mode alone far away to the coupling region). It is seen that a bigger coupling strength can produce a larger SPP efficiency enhancement: the enhancement factors are 170, 290, 180 and 70, respectively. The corresponding working wavelengths are 615nm, 710nm, 790nm and 900nm, respectively.

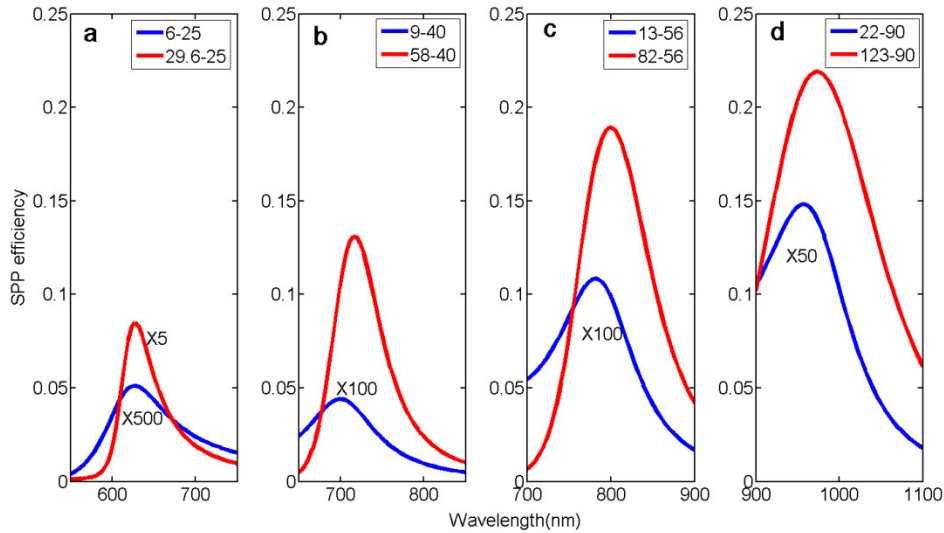


Figure A.3. SPP efficiency spectra of the optimal geometry for different values of the cylinder diameter and a fixed gap thickness of 1.5nm. The optimal geometry (red curve) is compared to a reference (blue curve) geometry with the same resonance frequency (S_{02} mode alone far away to the coupling region). (a) The optimal geometry (spectrum multiplied by a factor of 5) is $H = 29.5$ nm and $D = 25$ nm and the reference (spectrum multiplied by a factor of 500) is $H = 6$ nm and $D = 25$ nm; (b) The optimal geometry is $H = 58$ nm and $D = 40$ nm and the reference (spectrum multiplied by a factor of 100) is $H = 9$ nm and $D = 40$ nm; (c) The optimal geometry is $H = 82$ nm and $D = 56$ nm and the reference (spectrum multiplied by a factor of 100) is $H = 13$ nm and $D = 56$ nm; (d) The optimal geometry is $H = 123$ nm and $D = 90$ nm, and the reference (spectrum

multiplied by a factor of 50) is $H = 22\text{nm}$ and $D = 90\text{nm}$. Note that the aspect ratio height/diameter for the references is always around 0.23.

In Fig. A.4 and A.5, we study the impact of the gap thickness on the mode hybridization and the SPP emission enhancement; the gap thickness is varied from 1nm to 10nm. In order to avoid a variation of the different parameters with the wavelength due to the dispersion of the metal permittivity, we have chosen to work with a resonance of the gap mode S_{02} fixed at 800nm. Therefore, each value of the gap thickness corresponds to a different cylinder diameter to ensure such a fixed S_{02} resonance at 800nm. The red curves in Fig. A.4 show the SPP efficiency spectrum for the optimal height of each pair (gap thickness - diameter). The values of the corresponding geometrical parameters are given in the legends. The optimal antennas are compared to a reference geometry with a fixed cylinder height of 20nm. Such a small cylinder height ensures that the gap mode S_{02} is totally decoupled from the antenna mode L_{01} .

As shown in Fig. A.4(a), for a gap thickness of 1nm, the SPP efficiency from the optimal geometry (red line, $D = 39\text{nm}$ and $H = 72\text{nm}$) is around 15%, which is 200 times bigger than the reference (blue line, $D = 39\text{nm}$ and $H = 20\text{nm}$). Moreover, as shown in Fig. A.5(a), the SPP power emitted by the optimal antenna is 130 times higher than the reference. Since the total emission is reduced due to the mode hybridization, it is easy to understand that the enhancement of the SPP efficiency is slightly larger than the enhancement of the SPP intensity. With a gap of 2nm in Fig. A.4(b), the SPP efficiency of the optimal geometry ($H = 90\text{nm}$, $D = 74\text{nm}$) is a 50 times enhancement in contrast to the reference, while the SPP power is 30 times larger (see Fig. A.5(b)). Furthermore, as shown in Fig. A.4(c-d), concerning larger gaps of 5nm and 10nm, the enhancement factors of the SPP efficiency are 10 and 4, respectively. In these two cases, the SPP power enhancement factors are 4 and 1.2 (see Fig. A.5(c-d)).

In summary, a more significant mode hybridization effect takes place under a smaller gap in the patch antenna.

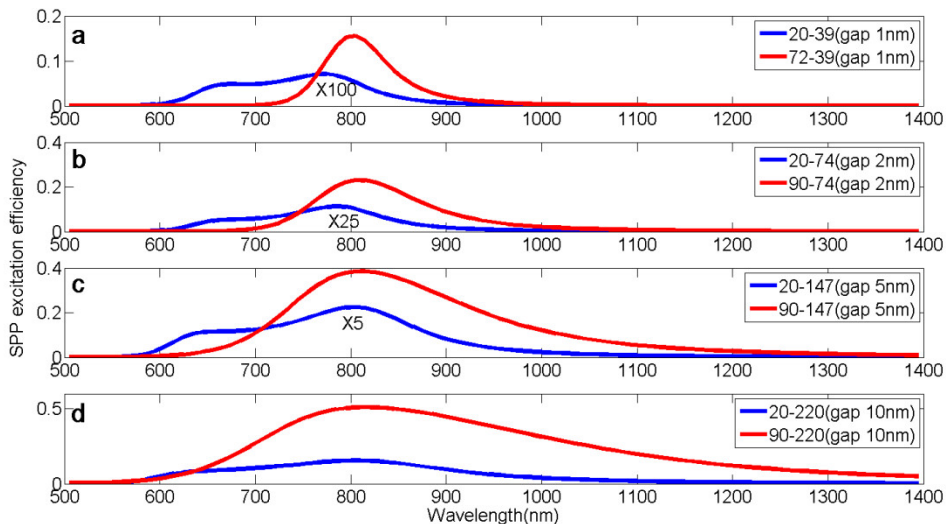


Figure A.4. SPP efficiency spectra (red curve) of the optimal structure that resonates at 800nm for different values of the gap thickness, 1nm, 2nm, 5nm, and 10nm, respectively. The optimal antennas are compared to a reference geometry ($H = 20\text{nm}$, blue curves) that corresponds to the gap mode S_{02} decoupled from the antenna mode L_{01} . (a) Gap thickness of 1nm. The optimal geometry is $D = 39\text{nm}$ and $H = 72\text{nm}$ and the reference (spectrum multiplied by a factor of 100) is $D = 39\text{nm}$ and $H = 20\text{nm}$. (b) Gap thickness of 2nm. The optimal geometry is $D = 74\text{nm}$ and $H = 90\text{nm}$ and the reference (spectrum multiplied by a factor of 25)

is $D = 74\text{nm}$ and $H = 20\text{nm}$. (c) Gap thickness of 5nm . The optimal geometry is $D = 147\text{nm}$ and $H = 90\text{nm}$ and the reference (spectrum multiplied by a factor of 5) is $D = 147\text{nm}$ and $H = 20\text{nm}$. (d) Gap thickness of 10nm . The optimal geometry is $D = 220\text{nm}$ and $H = 90\text{nm}$ and the reference is $D = 220\text{nm}$ and $H = 20\text{nm}$.

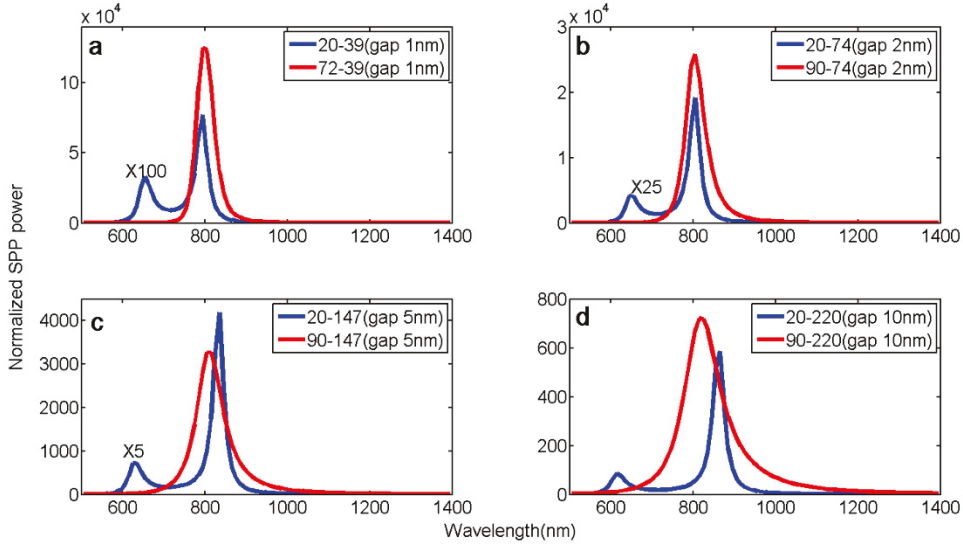


Figure A.5. Normalized SPP power spectra (red curves) of the optimal structures that resonates at 800nm for different values of the gap thickness, 1nm , 2nm , 5nm , and 10nm , respectively. The optimal antennas are compared to a reference geometry ($H = 20\text{nm}$, blue curves) that corresponds to the gap mode S_{02} decoupled from the antenna mode L_{01} . The values of the different geometrical parameters are the same as in Fig. A.4.

Additional notes:

The dielectric function of gold we use in chapter 3 and chapter 4 is given by a Drude-Lorentz mode that fits the data tabulated in the ref [53] over the $[0.5-1.5] \mu\text{m}$ spectral range. Note that the fitting formula for the Au permittivity as function of wavelength ($\lambda \mu\text{m}$) is given by:

$$\varepsilon_m(\omega) = \varepsilon_\infty - \frac{\omega_p^2}{\omega^2 + i\omega\gamma_D} - \frac{A_L}{\omega^2 - \omega_L^2 + i\omega\gamma_L} \quad (\text{A-1})$$

with $\omega = 2\pi c/\lambda$ the angular frequency, $\varepsilon_\infty = 6$, $\omega_p = 1.317 \times 10^{16} \text{ rad.s}^{-1}$ the plasma frequency, $\gamma_D = 6.216 \times 10^{13} \text{ rad.s}^{-1}$ the damping of the free electrons gas, $\omega_L = 4.572 \times 10^{15} \text{ rad.s}^{-1}$ the resonance frequency of the oscillator used in the Lorentz model, $\gamma_L = 1.332 \times 10^{15} \text{ rad.s}^{-1}$ the oscillator damping, and $A_L = 1.5\omega_L^2$ the oscillator strength.

Chapter 5

Fabrication of a nanoantenna MIM tunnel junction

5.1. Introduction

5.2. Strip antenna MIM tunnel junction

5.2.1. Substrate preparation

5.2.2. Al bottom electrode fabrication

5.2.3. Al thin film deposition and thermal oxidation treatment

5.2.4. Au strip antennas (top electrode) fabrication

5.2.5. Au connection pads fabrication

5.2.6. Wire bonding

5.3. Cylindrical antenna MIM junction

5.3.1. Planarization

5.3.2. ITO deposition for the top contact

5.4. Conclusion

5.1. Introduction

In this chapter, we are going to describe the fabrication of a tunnel junction assisted by a nanoantenna. Based on the design rule in chapter 3, a nanopatch antenna is a good candidate for the SPP emission by inelastic tunneling. To proceed, we fabricate two kinds of tunnel junctions, one has to be equipped with a strip patch antenna and the other one has a cylindrical patch antenna. Regarding the materials for a tunneling barrier we try a few attempts including self-assembly-monolayers (SAM) and Alumina. In terms of SAM layer, a couple of tunnel junctions have been developed based on this[75, 76]. However, it is difficult to sustain a homogenous molecular layer with a junction area above 100nm^2 . We have tried 1,9-NDT SAM layer to be used as a tunnel barrier in an Au/SAM/Au configuration. We found big majorities of junction have been shorted due to an inhomogenous molecular layer. In terms of alumina, which has been proved to be a durable material for making a large-area tunnel barrier. Consequently, we schematically show the devices in Fig. 5.1 (strip antenna configuration) and Fig. 5.2.(cylindrical antenna

configuration). The idea is to couple a fluctuating tunnel current with a resonant gap mode which can be efficiently transmitted to a propagating SPP on a dielectric/Al interface. Regarding the strip patch antenna junction, we propose to launch a plane SPP wave which is perpendicular to the strip antenna. For the cylindrical patch antenna junction, we propose to excite a cylindrical SPP wave. In order to increase the light emission power, we fabricate an array of strip antenna and cylinder antenna.

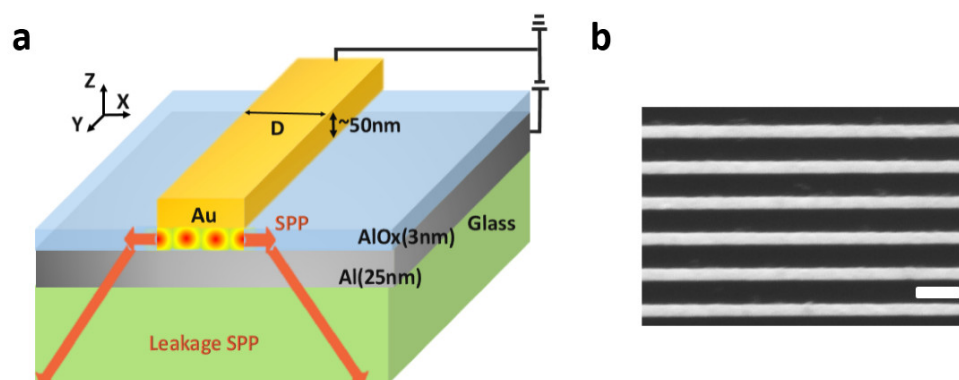


Figure. 5.1 (a) Schematic of the strip antenna tunnel junction. (b) A SEM image for showing a periodical patch antenna, note : the scale bar is 500nm.

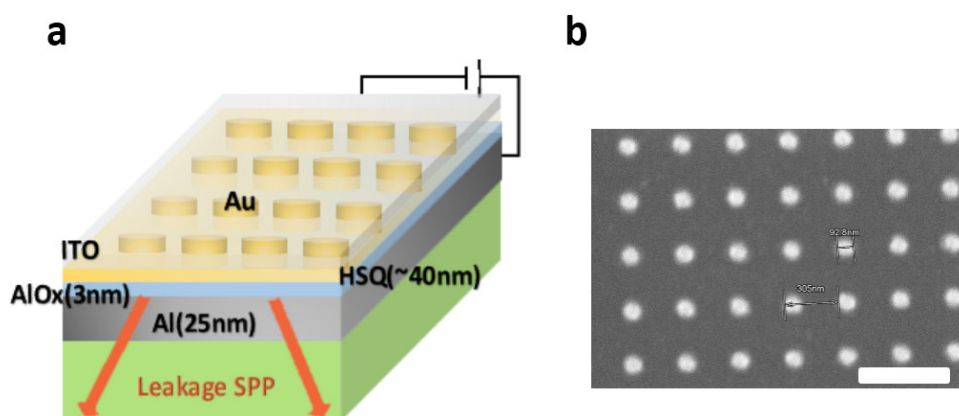


Figure. 5.2. (a) Schematic of the cylindrical antenna tunnel junction. (b) a SEM image for showing a cylinder antenna array, note the diameter of the cylinder is around 90nm and the period is around 300nm. The scale bare is 500nm.

5.2. Strip antenna MIM tunnel junction

5.2.1. Substrate preparation

In order to match our sample holder, the dimension of the glass substrate is fixed at $2.2\text{cm} \times 1.4\text{cm}$. The original glass substrate (VWR coverslips) has a dimension of $2.2\text{cm} \times 2.2\text{cm}$ with a thickness of 0.15mm. A micro diamond scribe (MR-200) is used to cut the substrate. Then, the cleaning procedure for the glass substrate is as follows:

1. We put the glass substrate into acetone and isopropanol (IPA) with an ultrasonic bath (power 100W) for 30 minutes and 30 minutes, respectively.

2. A nitrogen flow is used to dry the substrate.
3. We use 10 minutes of oxygen plasma to clean the substrate; the RF power is 300W and the gas pressure is 0.08mbar

5.2.2. Al bottom electrode fabrication

The MJB4 mask aligner is used for the photolithography. It is capable of handling several exposure modes. Considering a big feature size of the bottom electrode, the smallest feature size is $100\mu\text{m}$, so a soft contact mode is used. In this exposure mode, the MJB4 can achieve a resolution of $2\mu\text{m}$ at UV (400nm), which suits our needs. In Fig. 5.3, we show the standard steps of the UV photolithography.

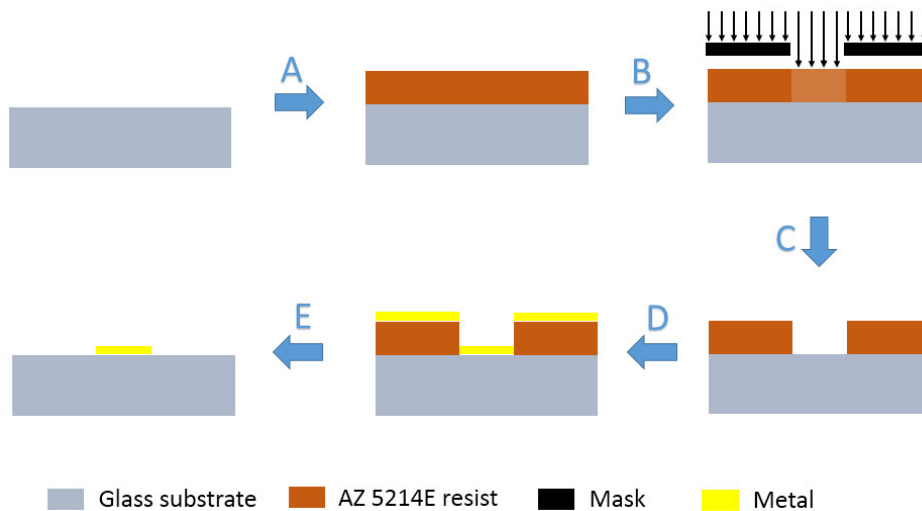


Figure 5.3. Schematic of the usual step for a UV optical lithography

Step A: Photoresist (AZ5214E) is spin-coated on a glass substrate with a spin rate of 4000rpm in 30s. Then, a prebaking on a hotplate, with 110°C and 2 minutes, is needed to harden the resist.

Step B: A positive mask is used for the UV exposure. A simple face mask aligner (MJB4) is employed to properly align the mask on the sample. We use a UV optical power of $2\text{W}/\text{cm}^2$ and an exposure time of 8s.

Step C: We develop the resist in a mixed developer (AZ400k : water =1:4) around 20s at room temperature. Then, we rinse the sample in deionized water for 30s. To ensure a good quality of the development, we use 1~2 minutes of O_2 plasma cleaning (120W RF power and gas pressure of 0.08mBar).

Step D: We do the metallic deposition via an e-beam evaporator (MEB Plassys); more details will be given for different materials.

Step E: Lift-off process is used in acetone at room temperature for 0.5h. Then we rinse the sample in IPA and DI water successively.

We should note that there is no good image contrast of Al microstructures in a SEM observation, thus it is difficult to align a mask in the following e-beam writing procedure. In order to solve this issue, it is necessary to fabricate a pair of Au marks to address the position of the Al electrodes. The rectangular Au marks pair is schematically shown in Fig. 5.4. The dimension of each rectangular is $150\mu\text{m}\times 550\mu\text{m}$ and the distance between them is 6mm.

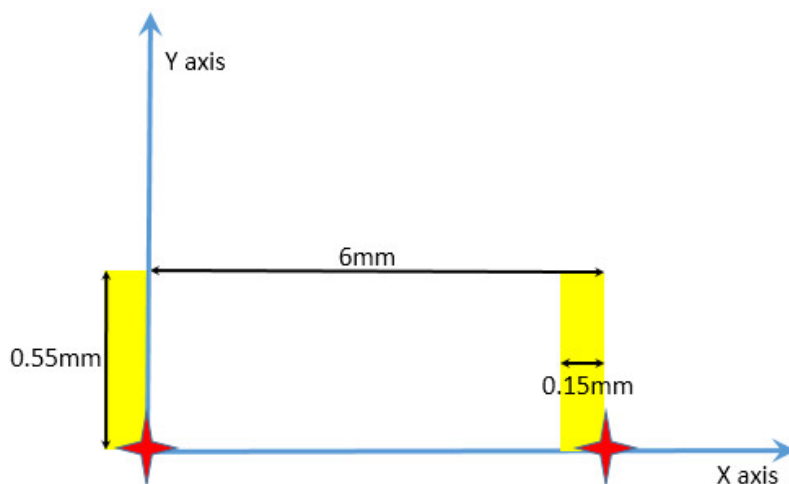


Figure 5.4 Au rectangular marks pair. The red stars are defining the coordinate system with the origin point and the X-axis for the e-beam writing.

All the steps for making the Au marks are based on the UV optical lithography. Regarding the metallic deposition, we deposit 1nm Cr and 50nm Au successively by using an evaporation rate at 0.05nm/s and 0.15nm/s, respectively. The vacuum pressure is under 1×10^{-6} torr. An optical microscopy image of one Au mark is shown in Fig. 5.5.

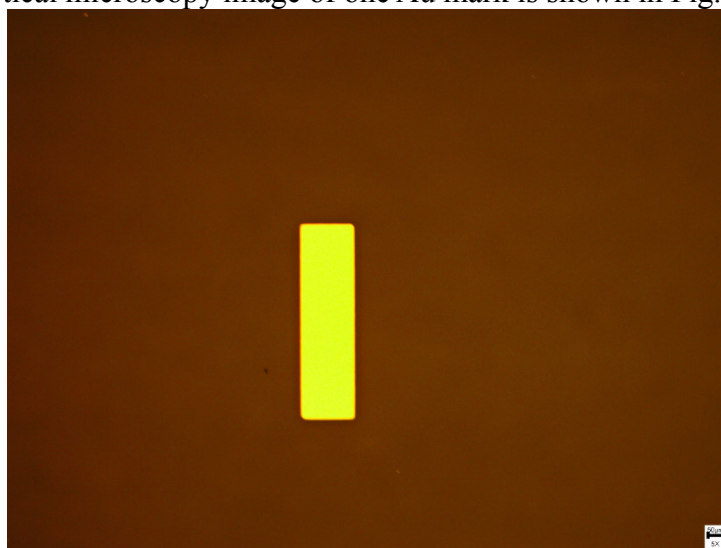


Figure. 5.5 An optical image of one Au mark, the scale bar is 50 μ m.

A second UV lithography is performed to fabricate the Al electrode. The mask of the Al electrode is shown in Fig. 5.6. it consists of 6 strips (width=100 μ m, length = 7mm) with a period of 1.5mm. Two pads, at each strip end with a dimension of 0.5mm \times 0.5mm, are used for the electrical connection. Because the recipe of the Al deposition can modify the AlOx layer formation, we prefer to discuss them together in the next section.

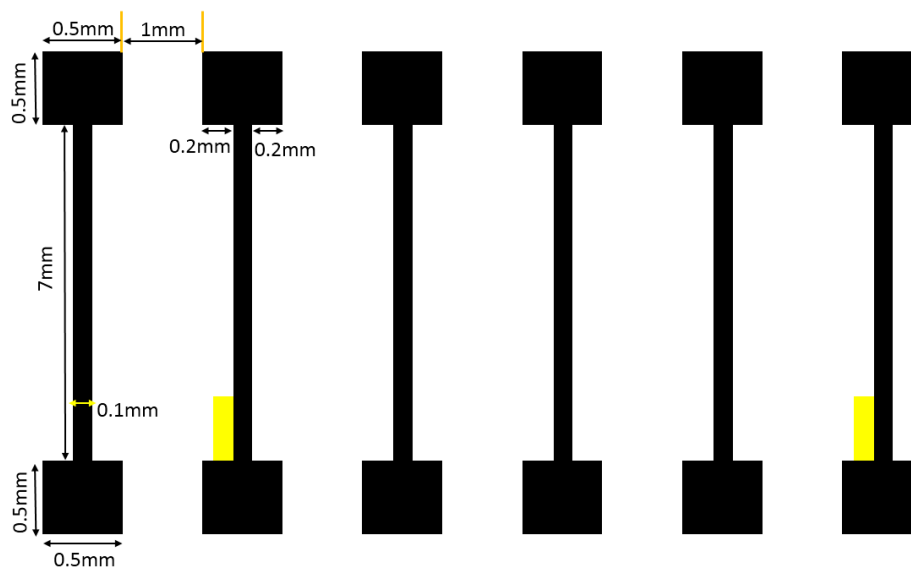


Figure. 5.6 A draw for the Al electrode (black components). The yellow rectangles are the Au marks.

5.2.3. Al film deposition and thermal oxidation treatment

Aluminium films are the most commonly used surface coatings for a wide range of applications in photonics technology[77]. The ultrathin oxide layer formed rapidly on the surface of an Al film can be used as the tunnel barrier for a MIM tunnel junction [78]. To fabricate the AlOx based MIM tunnel junction, the key is to have a good quality of thin evaporated aluminium film. Understanding the grain size distribution and the surface roughness of the Al films can help to fabricate a homogenous tunnel barrier. Apart from a durable tunneling barrier, a good quality of plasmonic cavity with a relatively thin Al film is also required. The electrical and thermal conductivities can be reduced significantly with an ultrathin metallic film, for example $<5\text{nm}$ [79]. At this point, a thicker metallic film supposes to have a smaller electronic resistance that could reduce the joule heat from the electrode. In our case, we find one whole Al electrode with a thickness of 25nm can normally reach a resistance around 250Ω . Compared to a $1\text{M}\Omega$ of tunnel resistance, it is negligible. Now we turn to study how the evaporation rate affects the Al surface roughness and surface morphology. We have fabricated several samples with different evaporation rates from 0.06nm/s to 0.5nm/s . With a small evaporation (rate around $0.05\text{nm/s}\sim 0.1\text{nm/s}$), shown in Fig 5.7(a), the surface roughness can be estimated around 2nm, and the surface profile is hilly. With a higher rate ($0.25\text{nm/s}\sim 0.3\text{nm/s}$ and $0.45\text{nm/s}\sim 0.5\text{nm/s}$), shown in Fig 5.7(b-c), the surface roughness is well controlled and the roughness is below 1nm. However, for the rate of 0.5nm/s , the surface profile suffers a more inhomogeneous grain distribution. To ensure a flat Al surface, we chose the evaporation rate at $0.25\text{nm/s}\sim 0.3\text{nm/s}$.

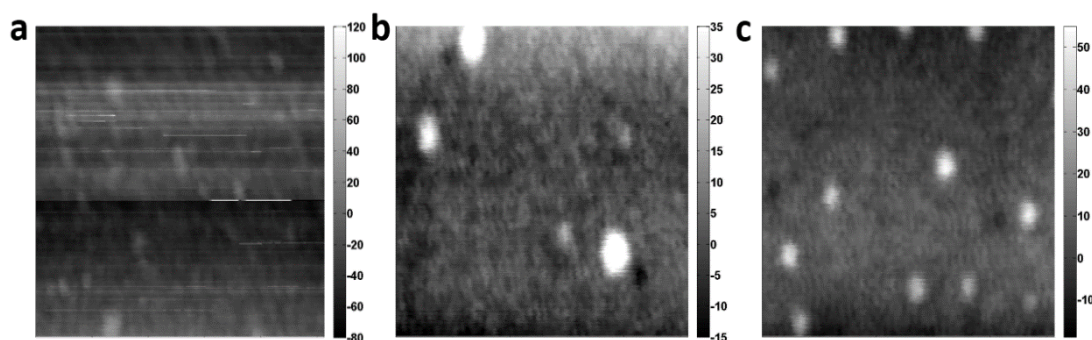


Figure 5.7 AFM images for the surface of Al film within $1\mu\text{m}^2$ at different evaporation rates (a) $0.05\text{nm/s}\sim 0.1\text{nm/s}$; (b) $0.25\text{nm/s}\sim 0.3\text{nm/s}$; (c) $0.45\text{nm/s}\sim 0.5\text{nm/s}$. Note: the color bar unit is Angstrom.

Operating an Al/AlO_x/Au junction at room temperature for long time is difficult as a dielectric breakdown might happen due to a pre-existing pinhole (defects) in the barriers. It is found experimentally that the lifetime depends on the operating temperature and applied voltage. In fact, we find a planar junction ($10\mu\text{m}\times 100\mu\text{m}$) would have a shortcut under a tunneling current density of 10^5 A/m^2 (with a voltage bias of 1.8v). Thus, conservatively, we target a maximum current density around 10^5 A/m^2 for a junction operating at ambient temperature. To this purpose, a barrier thickness around 2~3nm is needed. So, we designed a procedure to generate a 3nm of AlO_x layer. We perform a thermal oxidation by putting the sample (with the Al electrode immediately after the lift-off) in a furnace under atmosphere environment. The temperature is set at 200°C , the oxidation time is set about 3 hours.

5.2.4. Au strip antenna (top electrode) fabrication

A draw of the strip antennas assisted Al/AlO_x/Au junction can be seen in Fig 5.8. A connection wire perpendicular to the array connects the strip array. We see the active region is only filled by the antenna wires, thus it allows us to understand how an antenna works by inelastic electrons tunneling. The length of the strip is $60\mu\text{m}$, and the period of the array varies from 300nm to 800nm.

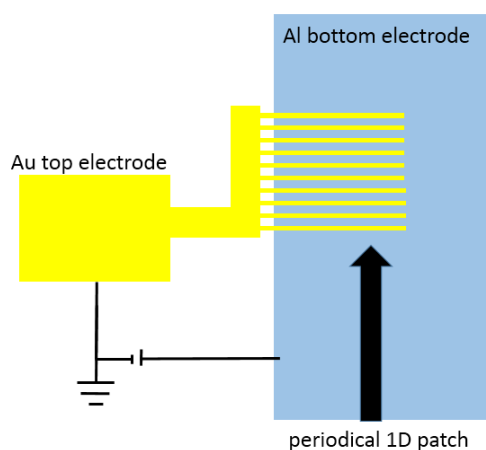


Figure 5.8 Schematic of the periodical strip antenna Al/AlO_x/Au junction

As mentioned in Fig 5.4, a pair of Au marks can help us to make a correct alignment for the e-beam writing. We need to point out that due to a resolution limit of a photolithography, the dimension difference of a mark can vary by $\pm 2\mu\text{m}$. This error may produce a misalignment for the e-beam writing. In order to avoid an overlapping between

the Au connection pad and the Al electrode, we keep a space of $15\mu\text{m}$ between them for holding the misalignment tolerance.

We use ZEP 520A as the e-beam resist. Compared to a common resist, like PMMA, ZEP has a better pattern contrast and fewer doses to clear. Thus, it allows us to have a better straight shape of antenna. Moreover, ZEP can be used as a good protective layer to prevent a further oxidation for the Al electrode. We spin-coat the resist by using a 4000rpm for 60s and do a prebaking on a hotplate with 170°C for 3 minutes. A conductive electronic layer is then spin-coated at 4000 rpm for 30s.

Usually, generating a high-resolution electron beam, for the manufacturing of small structure with dimension at sub-100nm scale, is relatively straightforward. However, moving the beam around the patterning field is not trivial.

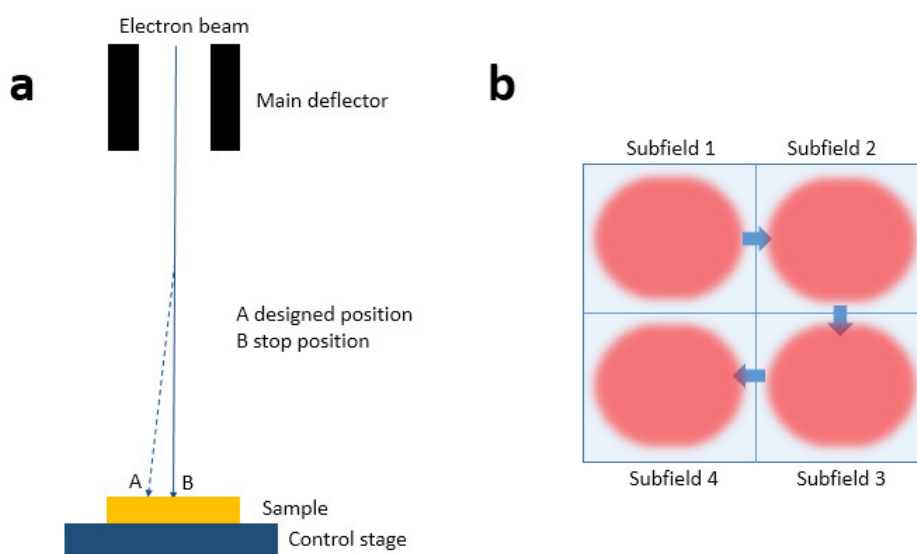


Figure 5.9 (a) e-beam writing principle for working with a defined pattern mask; (b) Schematic of the dose distributions in a writing process within a set of subfields, and the blue arrows show the stage movement direction.

In principle, e-beam tools have a certain maximum area where it can write for a fixed stage position. Regarding the NB4 lithography system, we have $20\mu\text{m}\times 20\mu\text{m}$ to be as a subfield for defining a basic writing block. As shown in Fig. 5.9(a), the electron beam can be positioned by the deflection electronics and electron beam deflector elements. Note that this is a digital deflection system, in which the beam positioning is determined by a digital value from a controlled computer (where associated to the e-beam pattern we use), which is subsequently converted to an analog signal. With a digital signal, the beam positioning has a finite number of possible discrete values where brings the formation of a drawing pattern. As shown in Fig. 5.9(b), an e-beam writing field is the amount of area that the electron beam can scan across (the blue marks show a scan movement). In a practical writing process, the writing dose distribution of one specific subfield is not that homogenous (we assume to use the same dose level in one subfield). The dose is almost uniform in the subfield center while it decreases a bit towards the subfield edges. Because our antenna array has a writing area at least $20\mu\text{m}\times 60\mu\text{m}$, the nanomask will inevitably get across the border of a subfield. In order to study how dose level affects the array pattern, we test a dose variation from 4.2 up to 7.5 (1 dose equals $1\text{C}/\text{m}^2$) with a resist thickness of 350nm. The lift-off results are shown in Fig. 5.10. It is seen that at a lowest dose in figure (a), a large part of strips have been removed. While for the case with a

bigger dose level, like figure (b) to (d), it allows compensating the dose level near the subfield border, thus the pattern is more homogenous.

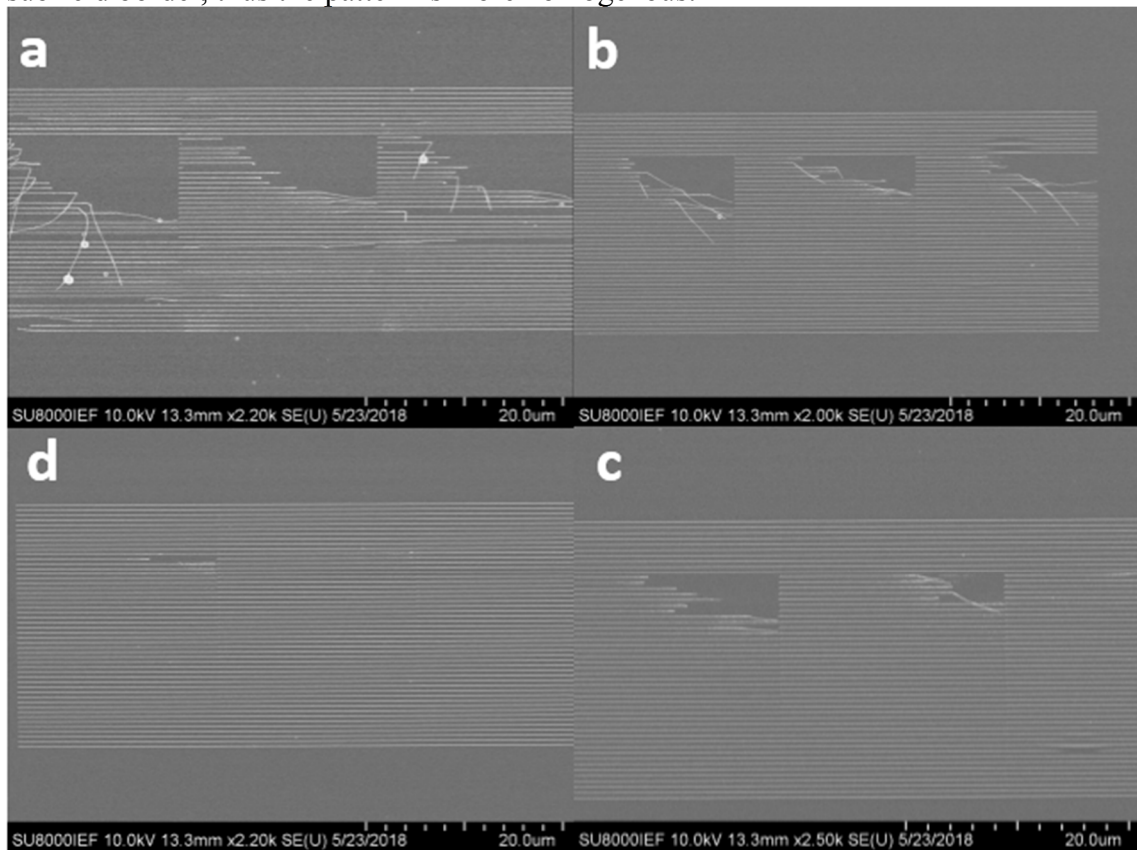


Figure 5.10 Different dose level for fabricate strip arrays with a period of 500nm. (a)-(d) show the results with a dose of 4.2, 5.1, 6.0 and 7.5, respectively.

To fabricate correct dimensions of nanostructures, a suitable dose level is critically needed. Basically, a dose is related to the exposure current and exposure time on a defined surface, see the equation below:

$$D = (I * t) / A, \quad (4-1)$$

where I is the current, t is the exposure time and A is the exposure surface.

By using a constant current for making an exposure, a bigger dose can take a longer time. Thus, it takes more chances to generate e-beam forward and back scattering in the resist. If the scattering is strong enough, it can make some extra exposures and broaden the pattern dimension. It is obviously seen that an increased dose can kill the subfield effect, while the width of the strip produces a bigger feature size. In Fig. 5.11 (a-d), we can see the width has been enlarged from 65nm to 115nm with a growing dose. Therefore, it is rather difficult to erase the subfield effect by only playing with a bigger dose.

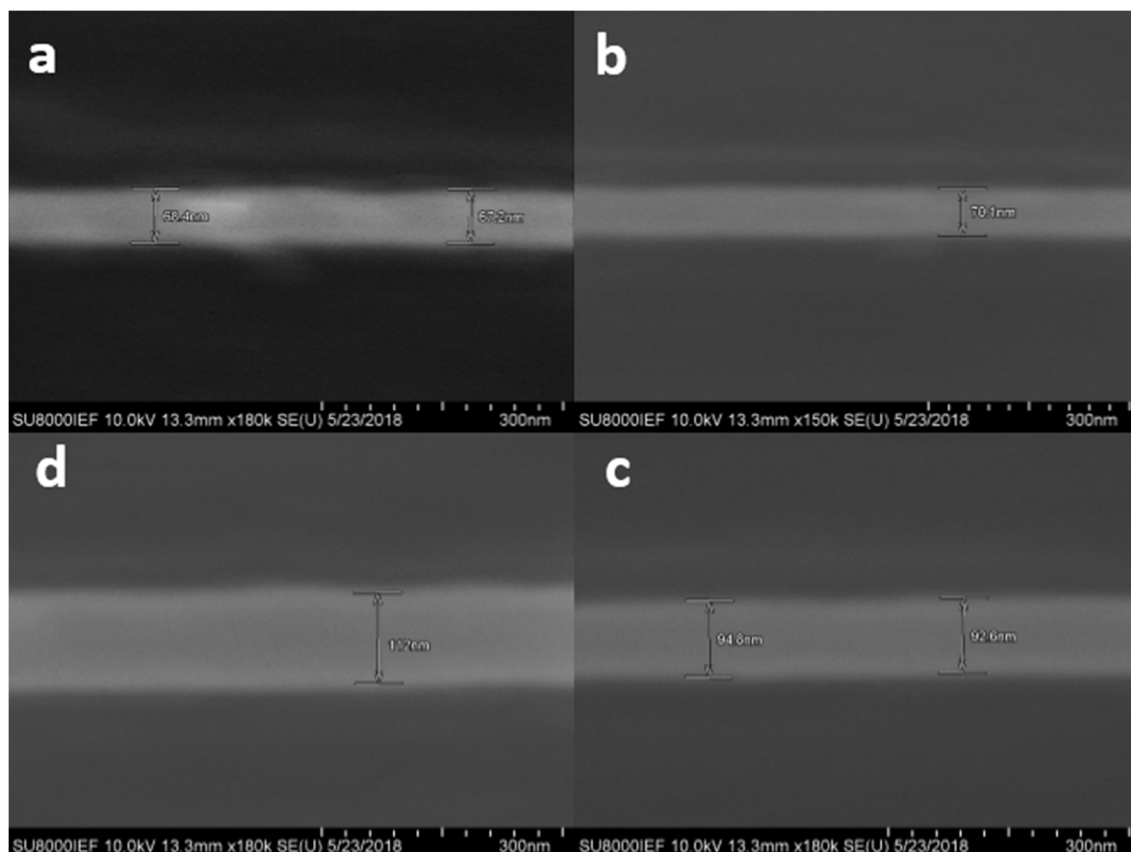


Figure 5.11 (a-d) SEM pictures for showing the width of strip via a dose variation from 4.2, 5.1, 6.0 and 7.5, respectively.

To develop the e-beam resist, the procedure includes: first, deionized water during 30s to remove the conductive layer and rinsing in IPA for 30s. Second, immersion of the sample in ZED-N50 for 90s to develop the e-beam resist. Third, the sample is put in a mixed developer (MIBK: IPA=1:3) for 30s to complete the development of e-beam resist at a relatively low speed; finally, the sample is rinsed in IPA for 30s and dried with a stream of N_2 . We then deposit 50nm of Au (together with 1nm of Cr, evaporation rate of 0.05nm/s, as a stick layer) with the e-beam evaporator using a deposition rate of 0.15nm/s. The final lift-off is performed with butanol for 3 hours.

To maintain a good pattern feature with a proper dose, a thinner resist thickness is suggested. Since we have 50nm of thickness for the Au top electrode, so a thinner e-beam film (around 200nm, three times bigger than 50nm, still easy to do the lift-off) can be used by a diluted ZEP (ZEP : anisole=1:1).

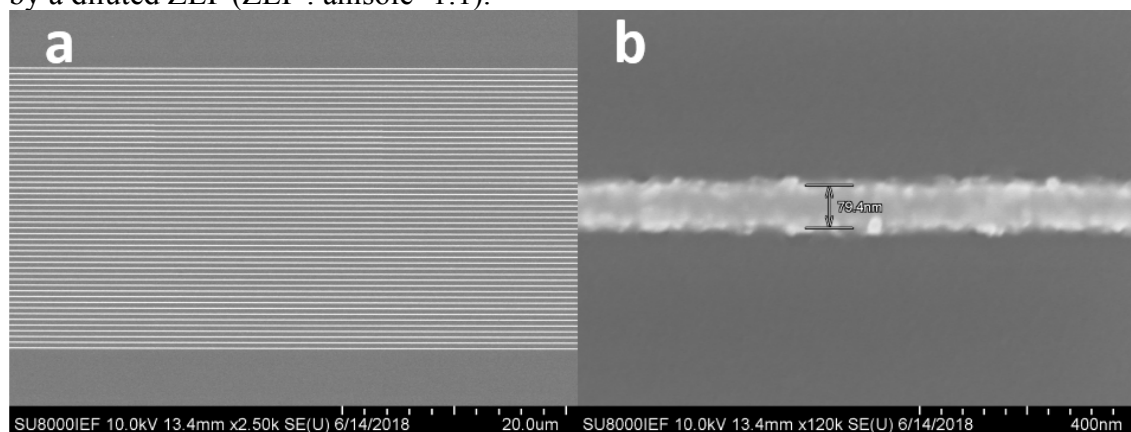


Figure 5.12 SEM pictures of the strip array by using a thinner resist (~200nm) with a dose of 4.5; (a) the

strip array with a period of 500nm; (b) the width of the 1D patch is around 80nm.

In Fig 5.12(a), a thinner resist is employed in a writing test. We can see a perfect strip array with no more subfield stitching issue, and the dose here is relatively ($\sim 4.5C/m^2$) low. The width of the strip is well controlled around 80nm, see Fig. 5.12(b).

Towards a realized sample, we fabricate two different widths of strip (85nm and 125nm) in order to emit a resonant light from 800nm to 1000nm. In Fig 4.15, we show an optical image of the arrayed strip (figure a) and two SEM pictures (figure b and c) for presenting the dimension of the strips. In Fig. 5.13a, a uniform strip array can be seen; in Fig .5.13 b-c, the widths of two different strips are read as 128nm and 85nm, respectively. Note: there is a width fluctuation along the wire edge, which takes a value around ± 10 nm.

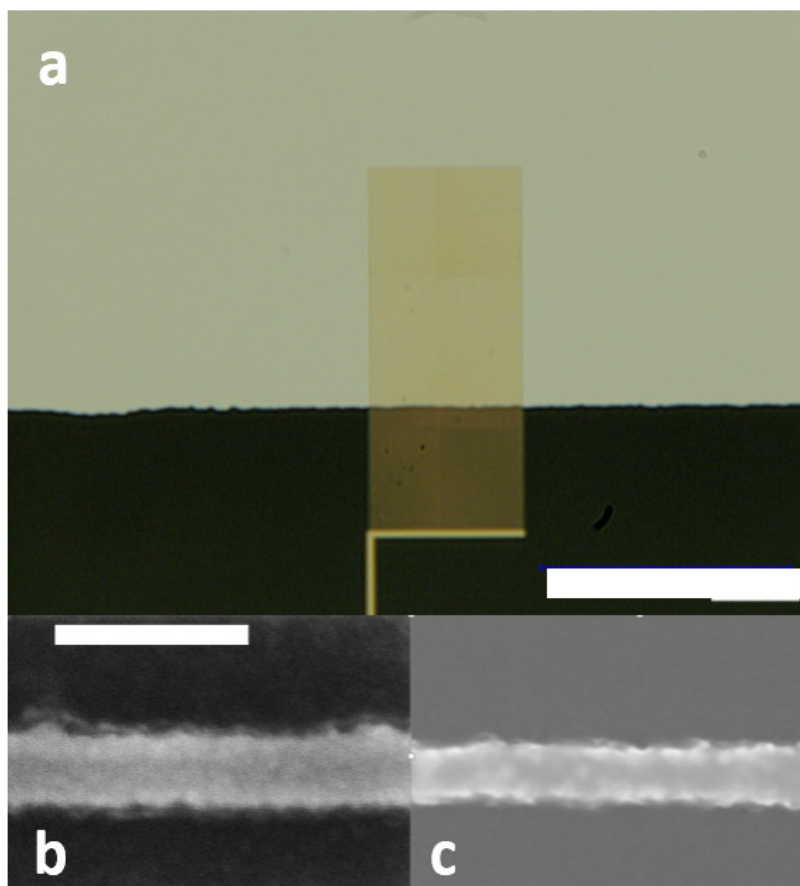


Figure. 5.13 (a) An optical image of one strip antenna array with a period of 400nm, the scale bar is 50 μ m; (b) A strip antenna with a width around 128nm; (c) A strip antenna with a width around 85nm, the scale bar is 300nm.

5.2.5. Au connection pads fabrication

Through the e-beam writing, we have defined the antenna junction. In order to complete a circuit to apply a voltage, we need an external macroscopic Au connection pad for a wire bonding. No matter the wedge bonding, ball bonding or other related techniques; it needs the connection pad to have a relatively big thickness (>200 nm) and large area. We fabricate the connection pads by laser lithography.

Direct laser writing, a kind of mask less lithography, similar to an e-beam writing, is to scan a programmable reflective photomask which is then imaged on to the photoresist. It offers rapid patterning at sub-micrometer resolutions. The laser writing is based on the

Heidelberg instruments DWL 66fs laser-writing tool. It has been equipped with four major elements: a diode laser with the wavelength of 405nm, the beam-shaping modulator, a fast deflector and writing lens. We use a writing head with a focal length of 20mm. Additionally, a camera is employed to help us for the mask alignment.

In order to deposit 200nm of Au film, the thickness of the photoresist is around 1.3 μm . The photoresist is the S1813, which has a good photosensitive from 400nm to 430nm. Note the developer of the S1813 is a kind of alkaline product, thus the Al pad can be etched away during a resist development. Based on this, we only deposit a connection pad for the Au electrodes. In Fig 5.14, we show the Au connection pad.

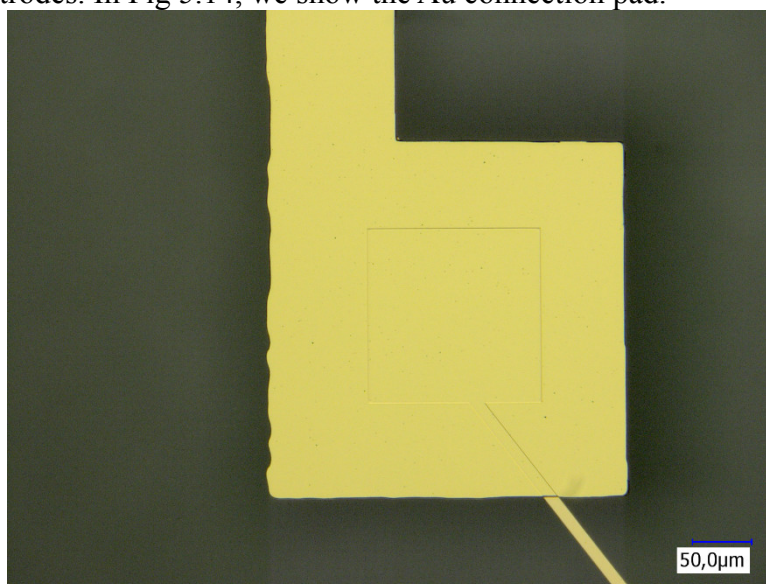


Figure 5.14 An optical image for showing the Au connection pad after the laser writing, the scale bar is 50 μm .

Notes for the recipe: (1) we spin coat the photoresist (S1813) with 4000rpm for 30s. We do a prebaking on a hotplate at 110 $^{\circ}\text{C}$ with 2 minutes. (2) The laser writing process. (3) We develop the sample in MF319 solution with 30s at room temperature. (4) Ti (10nm) and Au (200nm) deposition with evaporation rate of 0.05nm/s and 0.3nm/s. (5) lift-off is done in acetone with 30 minutes.

5.2.6. Wire-bonding

Wire bonding is a kind of solid state welding technique, and it consists of three bonding mechanisms: thermocompression bonding, thermosonic bonding and ultrasonic bonding. Thermocompression is the way using heat and force to deform the wire and make bonds. The diffusion reactions progress exponentially with temperature. Therefore, even small increases in temperature can improve bond process significantly. Usually, it needs high temperature (above 300 degrees) and high force, so it may damage the dies if it is quite sensitive. For thermosonic bonding, heat is applied by placing the package on a heated platform. Force is also applied by pressing the tool into the wire to force it in contact with the substrate surface. In ultrasonic bonding, the pressure and temperature are relatively lower than with the other two kinds of bonding techniques.

In general, there are two kinds of wire bonds: ball bonding and wedge bonding. Due to an oxidation for the Al wire during the electronic flame off process to form the ball, Al wire is not suggested in ball bonding. While for the wedge bonding, both Al and Au wires are suitable.

In order to perform a nice bonding, a few points need to be clarified:

* Effect from the substrate. Making a good bonding requires a good bond pad which includes pad metallization, surface thickness and pad cleanliness. Usually, the pad area should be at least 3~4 times bigger than the diameter of bond wire. A thicker gold bond pad is suggested, for instance around 200nm. It is also very important to keep the bond pad free from any contaminations.

* Bonding process variables. In bonding process, some variables should be paid attention with ultrasonic power, bonding force, bonding time and temperature. A good bond can be characterized as high pull strength and consistent tail length. There is a strong relationship between pull strength and wire deformation. Different pull strengths may lead to different bonding results. If the pull strength is too small and fast, it will make a nonstick with no bonding; while a higher pull strength may create a foot-lift. Only a proper strength with a proper time can give an optimal bonding result.

In our application, we have tried both the ball bonding and the wedge bonding. See the table below, all the process variables are shown as a comparison between the ball bonding and the wedge bonding. It is worth to mention that the first bond is on the gold pad from the sample, and the second bond is on the sample holder (copper surface).

	Wedge bonding	Ball bonding
Power(mW, 1 st /2 nd bond)	350/580	182/70
Force(mF, 1 st /2 nd bond)	29/39	50/21
Time (ms, 1 st /2 nd bond)	244/480	180/36

Table 5.1 available parameters for the ball bonding vs the wedge bonding

From table 5.1, we can clearly see that the wedge bonding requires a bigger power and longer process than the ball bonding.

To make an electrical bond on the Al electrode, we use a small droplet of silver conductive paste to merge between one end of a copper wire and one Al connection pad. A second droplet is applied between another end of the copper wire and one die from the sample holder. Note the resistivity of our silver paste is around $1 \times 10^{-4} \Omega/\text{m}$.

5.3. Cylindrical antenna MIM junction

Now we turn to study the fabrication of a cylindrical antenna assisted MIM tunnel junction. The process is schematically shown in Fig 5.15. Basically, step A, B and C are based on a general e-beam writing. Then, a piece of HSQ (Hydrogen silsesquioxane) layer is spin coated on the antenna array in step D. A wet etching or a reactive ions etching are employed to carry the planarization in step E. In step F, a thin ITO film is deposited on the PDMS substrate via a magnetic sputtering; then, the piece of ITO coated PDMS is transferred on the top of cylinder array to make the top contact.

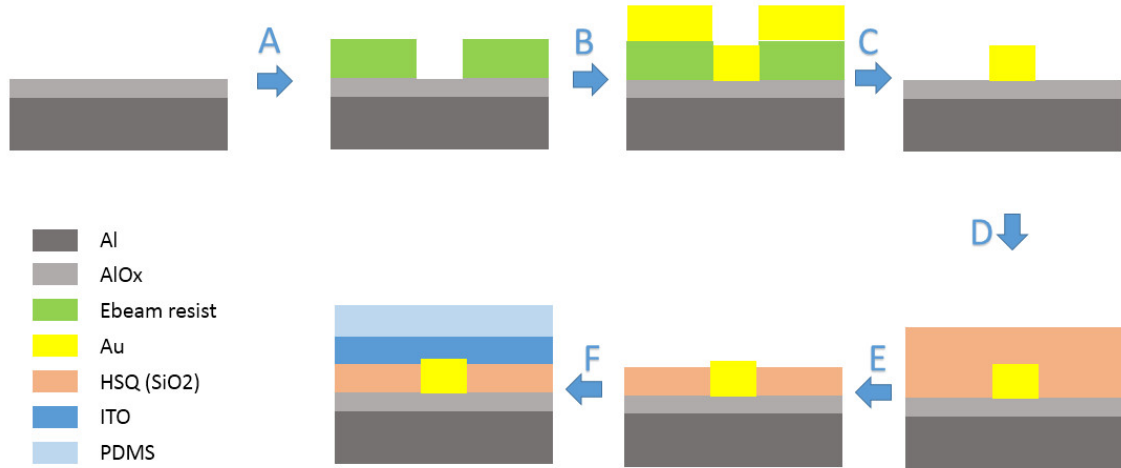


Figure 5.15 schematic of the cylinder array MIM junction fabrication procedure

As the step A to C have similar descriptions as the section 5.2, so in the following section we are going to only focus on the step D to F.

5.3.1. Planarization

There is technical difficulty to drive a nanoantenna array by inelastic tunneling electrons. The main obstacle is to make an effective electrical contact. Some related works are shown in[80, 81], nanoparticles have been placed on the top electrode of a planar junction, enhanced light emission is observed. However, the nanoantenna only affects a tiny fraction of the tunnel current so that the entire device is still inefficient. To tackle this issue, we need to figure out an effective electrical top contact in arrayed cylindrical antenna assisted tunnel junction.

In the configuration of a cylinder-arrayed junction, the integration of cylinder architecture remains constrained by the need to master thin layers including conductive and insulating. This kind of non-planar structure requires to build the electrical connection to each terminal of the component. Thus, the engineering of insulating layers in these nanostructure arrays is a critical issue. To this purpose, the material should have a low dielectric constant to minimize capacitances, should perfectly fill the gap between the cylinders with good flatness and low roughness, and should show a good mechanical and thermal stability. Several studies have started with the organic polymers (like S1808 and SU8) as filling materials to obtain planarization of nanowire array[82]. However, these materials have drawbacks, for instance, the appearance of voids between the layers and as well as thermal and mechanical instabilities.

Inorganic materials, such as silicon oxide[83] and spin-on-glass materials[84], can provide good results but have a large chance to have wave effects at the foot of the nanostructures. So far, one available method for circumventing the wave effect issue is to embed the nanostructure arrays in an insulator layer, as shown in the step D of Fig. 5.15. Then, the whole array network can be etched back to a desired thickness for decoupling the final thickness from the height of nanostructure, as shown in the step E of Fig. 5.15. Based on this idea, HSQ can be a good candidate. HSQ is widely used in the semiconductor industry as an interlayer dielectric in order to enhance the resistance capacitance and increase the signal propagation speed because of its low dielectric constant. Moreover, HSQ can sustain an excellent gap fill properties which is perfect for planarization.

The HSQ resist is a kind of inorganic polymer with a general formula $(\text{HSiO}_{3/2})_n$. Originally, it has a cage-like chemical structure, as shown in Fig. 5.16(a). The standard recipe for curing the HSQ is to spin coat a layer and then chemically stabilize the whole layer by thermal annealing[85] or reactive ion etching (RIE) with oxygen plasma[86]. After a curing, the cage-like structure can evolve to a SiO_2 -like network structure (see Fig 5.16(b)) through a scission of a Si-H bond to form a Si-O-Si bond.

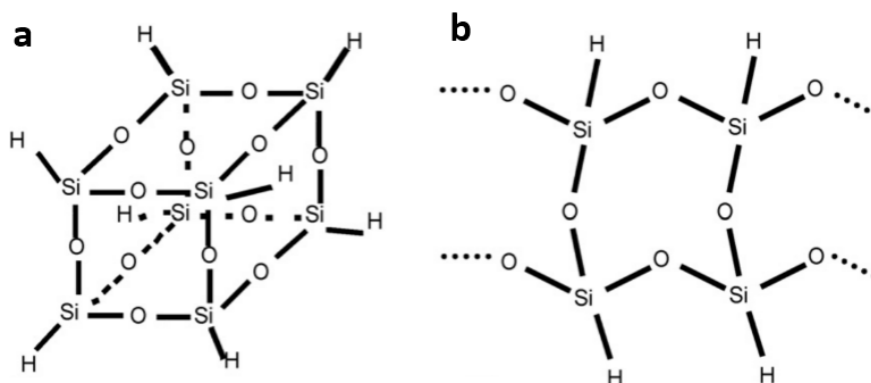


Figure 5.16. Chemical structure of two kinds of HSQ: (a) a cage structure of HSQ; (b) a network structure of HSQ.

We need to know the exact height of a cylinder in order to process a planarization. See the Fig. 5.17, thanks to a hybrid-coupling mode (based on calculation model in the chapter 4), an optimal light emission (wavelength range from 800nm to 1000nm) can be obtained with a cylinder height of 70nm and a diameter of 100nm. In order to benefit the hybridization effect, we fix the height of the cylinder at 70nm for the following fabrication procedures.

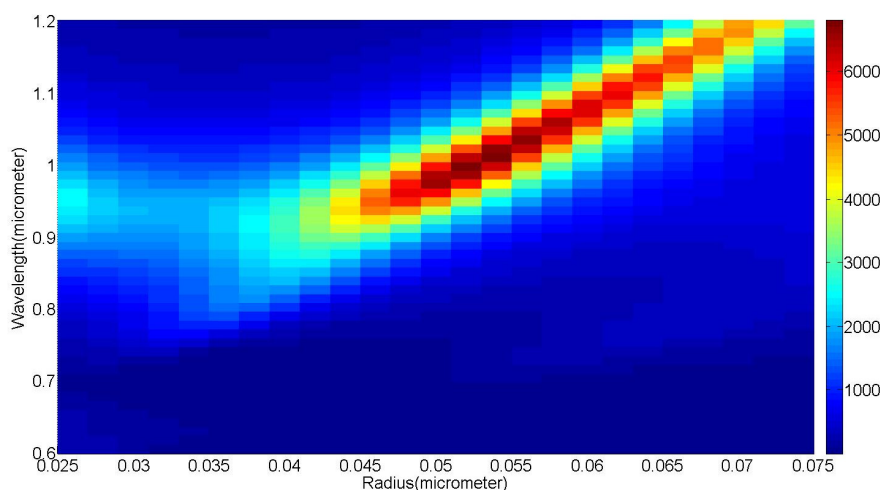


Figure 5.17 Normalized light emission intensity from a cylindrical patch antenna with a fixed height of 70nm, is plotted as a function of the wavelength and the radius of cylinder

We use Fox-15 (HSQ solution in MIBK) for the spin-on-glass material. Considering a nanostructure with 70nm height, a thicker HSQ layer is determined to have less wave-effect, while it needs a longer etch-back process time that might not sustain a flat surface. Thus, for a good planarization, we need carefully select a proper original HSQ film thickness.

See Fig 5.18, we spin coat two different thickness (430nm and 300nm) of HSQ layer

on two samples with a cylindrical array. Seen from the Fig. 5.18(a), there is no clear signal to show a wave effect with a thickness of 430nm HSQ. Whereas for the sample with 300nm of HSQ layer, we see a feeble wave effect with a height less than 5nm. Considering a 70nm of structure height, this small effect is negligible. Finally, we choose to use a HSQ layer with 300nm for the planarization.

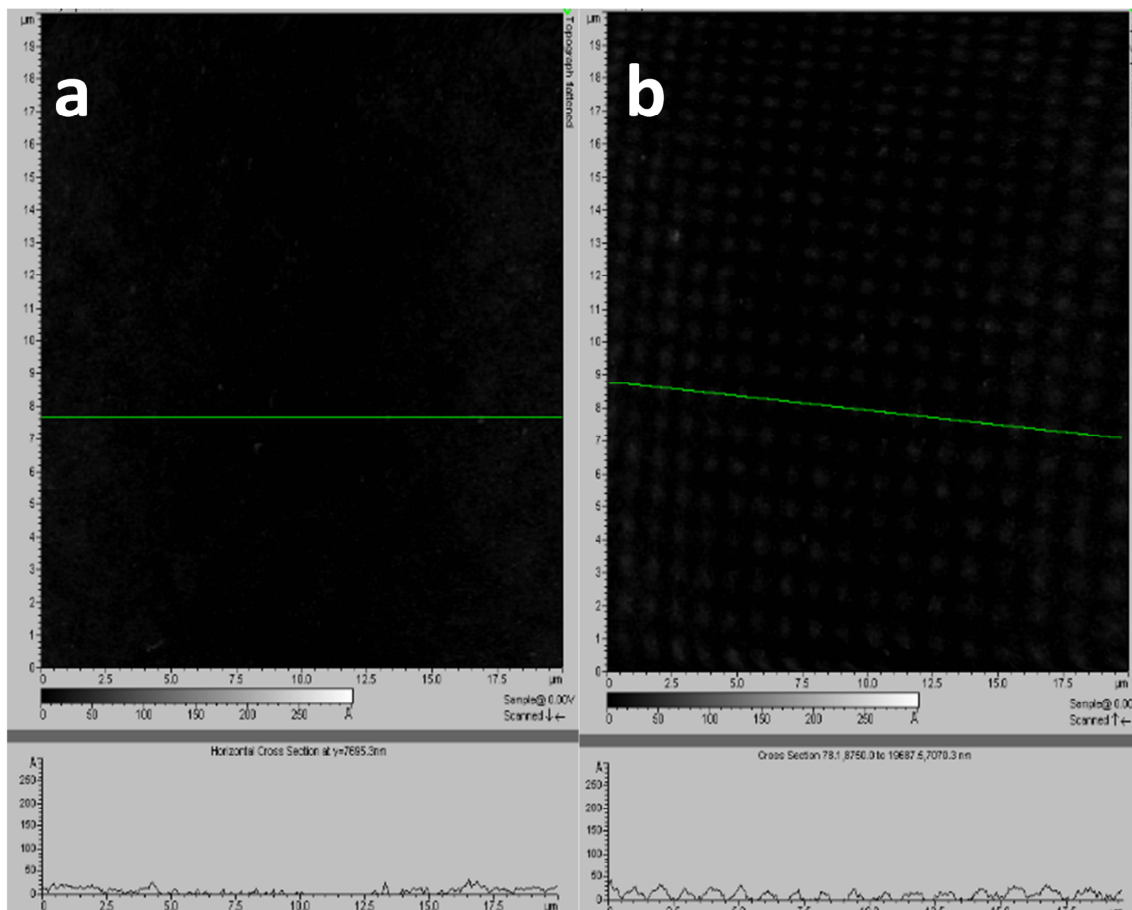


Figure 5.18. AFM images of the surface profile of antenna array embedded HSQ layer. (a) with a HSQ thickness of 430nm; (b) with a HSQ thickness of 300nm.

To proceed, for a thin HSQ layer curing, oxygen plasma or thermal curing can be used. In order to have a better SiO₂ network structure, a high RF power of plasma and a high temperature curing are suggested[86]. Due to a possible instability of temperature during the curing, the thin film may produce cracks, as shown in Fig. 5.19. In reference [86], the transformation rate of the HSQ structure is evaluated under different annealing temperatures and also plasma treatment conditions. Even with a high curing temperature (i.e., 800°C) and a high RF power of plasma, it is noted that the HSQ film is not completely transformed into a SiO₂-like network structure. Therefore, a better way to make a single-phase planarization layer is to spin coat a HSQ layer and to perform a curing after an etch-back procedure.

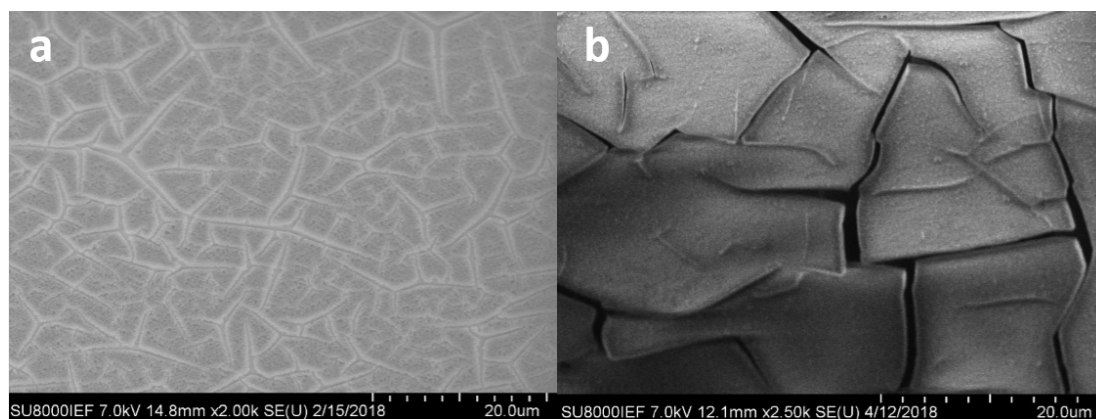


Figure 5.19 SEM images of the surface profile of the HSQ thin film after a curing process; (a) after an oxygen plasma treatment (gas pressure = 0.08mbar, RF power = 270W, curing time = 20 minutes); (b) after a thermal curing with 400°C in a nitrogen environment.

To perform the planarization, we try a wet etching, which is a common way for a SiO_x etching in industry. In order to sustain a flat surface after a wet etching, we use a diluted hydrofluoric acid (HF: water=1:450) to slow the etching rate down to 2nm/s. After 2 minutes of etching, see Fig 5.20, the surface morphology is hilly which corresponds to an isotropic wet-etching mechanism.

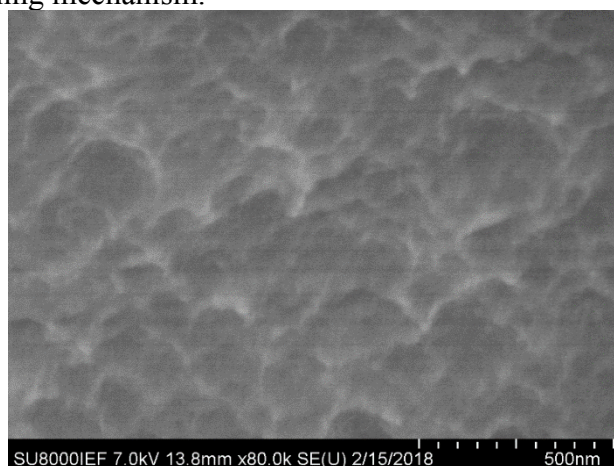


Figure 5.20 The surface profile of a HSQ thin film after 2 minutes of wet etching at room temperature.

In contrast to the wet etching, a dry etching is proposed to give an anisotropic etching profile due to its mostly vertical delivery of reactive ions. Regarding the RIE for etching silica, there are two possibilities, which are CHF₃-based and SF₆-based etchant gas. By using the CHF₃-based gas, some related species such as CF₄, HF, SiF₄, CH₂F₂, and CO₂ can be detected during the etching reaction. It has been reported that the rod-shape or dot-shape growth of fluorocarbon nanostructures are possible to appear under various RIE conditions[87]. As the surface roughness is more important, it is interesting to monitor any possible nanoparticles formation due to an etching reaction. In Fig 5.21, we see a continuous growth of ‘dust nanostructure’ by varying the RIE process time from 2 minutes to 8 minutes. Especially in Fig. 5.21(d), an array of gold antenna cylinder has been randomly decorated by fluorocarbon nanoparticles, which leaves us a message that it is rather difficult to make the top electrical contact on the cylinder array.

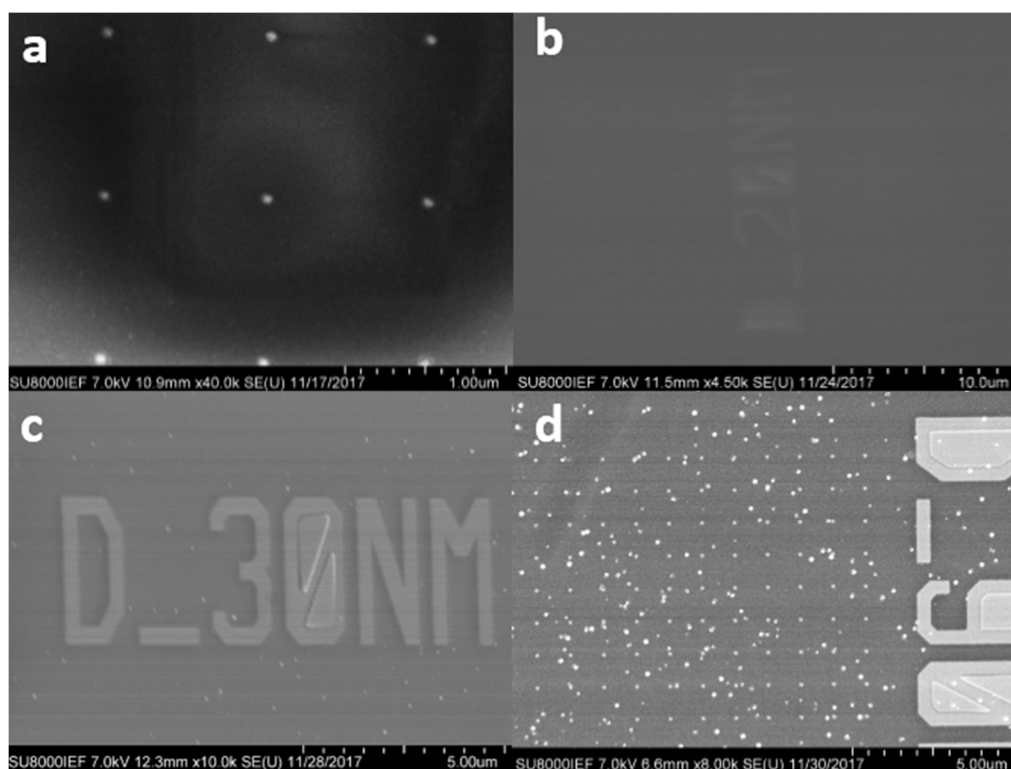


Figure 5.21 (a) SEM image of a cylinder array before the HSQ film deposition; surface profile after applying CHF_3 (20 sccm)+ O_2 (1sccm) with 20mtorr and RF power of 150W, (b) with a 2minutes of etching; (c) with a 5 minutes of etching; (d) with a 8 minutes of etching.

We have also tested a planarization by increasing up the RF power from 150W to 200W to reduce the processing time. As compared between Fig 5.22 (a) and (b), we get a much dense distribution of fluorocarbon particles which indicates the formation of the fluorocarbon particle has a link with the process time and the etching intensity.

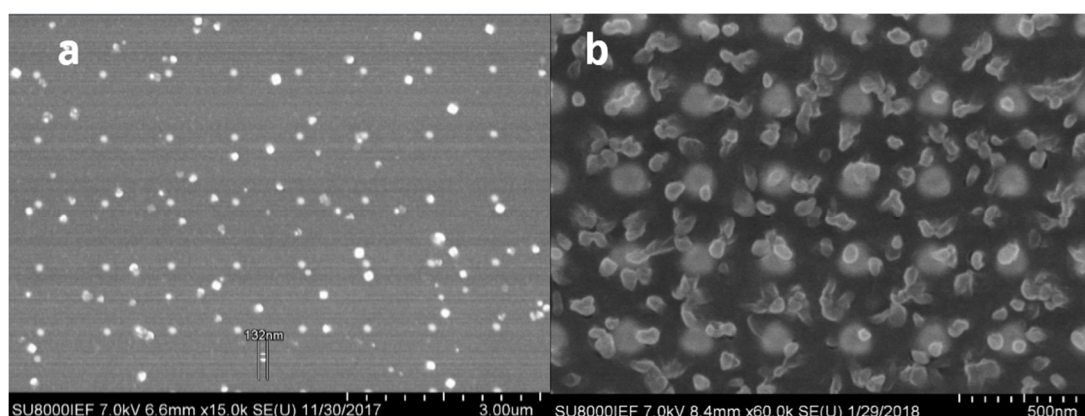


Figure 5.22 Comparison of the surface morphology after CHF_3 etching between two different RF power; (a) RF power of 150W with etching time of 8 minutes; (b) RF power of 200W with etching time of 5 minutes.

Since the CHF_3 -based etching is not suitable for the planarization in our case, we switch to SF_6 -based RIE. Therefore, we investigate the surface morphology of the planarized layers

by using different etching power, see Fig 5.23. Three different RF powers with 150W, 100W and 75W are employed respectively in Fig 5.23(a), (b) and (c); the gas pressure is 15 mTorr, the gas flow speed is 10sccm and the etching time is 5minutes. We see that a higher etching power produces a larger roughness. For the case with 75W, the surface is nearly perfect.

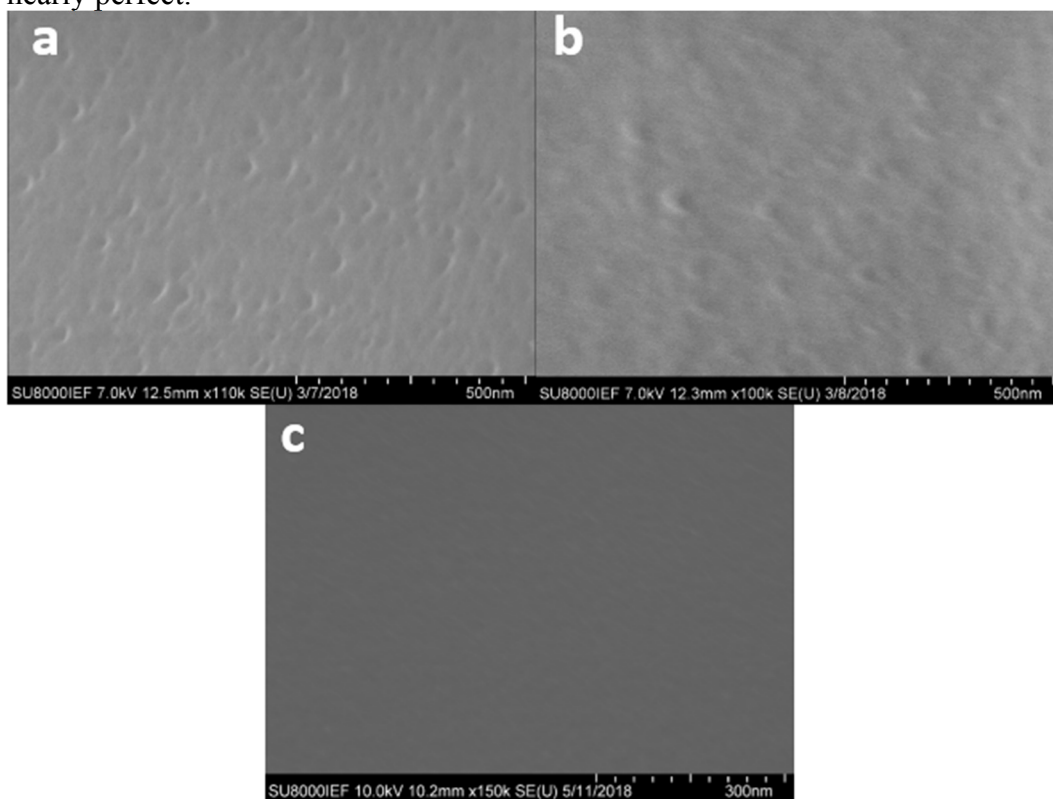


Figure 5.23 SEM images of the surface for varying different RF etching powers, (a) RF power of 150W, (b) RF power of 100W, (c) RF power of 75W.

To proceed, we keep using a RF power of 75W to finalize the planarization. See Fig 5.24, two SEM pictures show the cross section of the HSQ film before and after the RIE by SF_6 . A finalized planarization layer with a thickness of 40nm can be obtained. In order to ensure an intense planarization layer, a proper oxygen plasma curing (RF power 100W, gas pressure 0.08mbar and process time 2minutes) is applied.

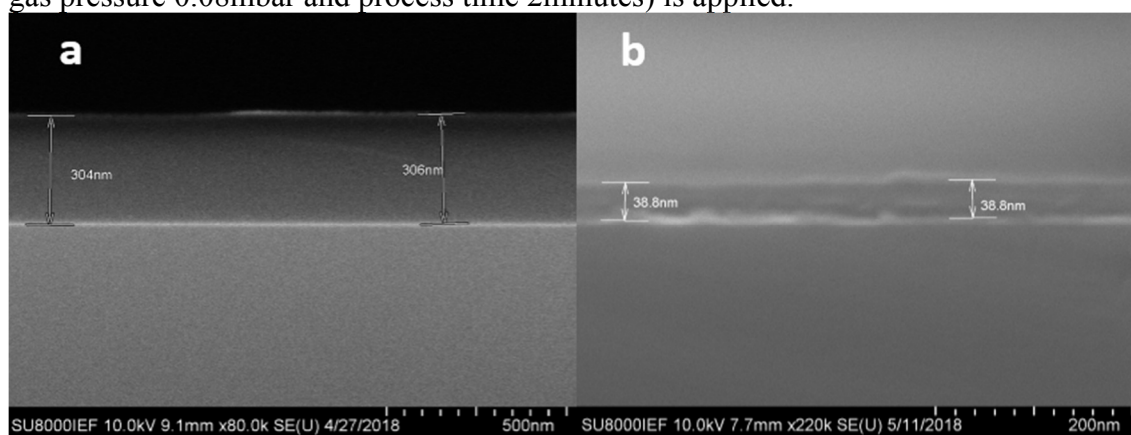


Fig 5.24 SEM images of the cross section of the HSQ film (a) before the RIE; (b) after the RIE.

We also use an AFM to characterize the quality of the planarization layer, see Fig 5.25. The surface profile has been measured to assess the height of the cylinder antenna after

RIE. It is seen that the planarization is perfect.

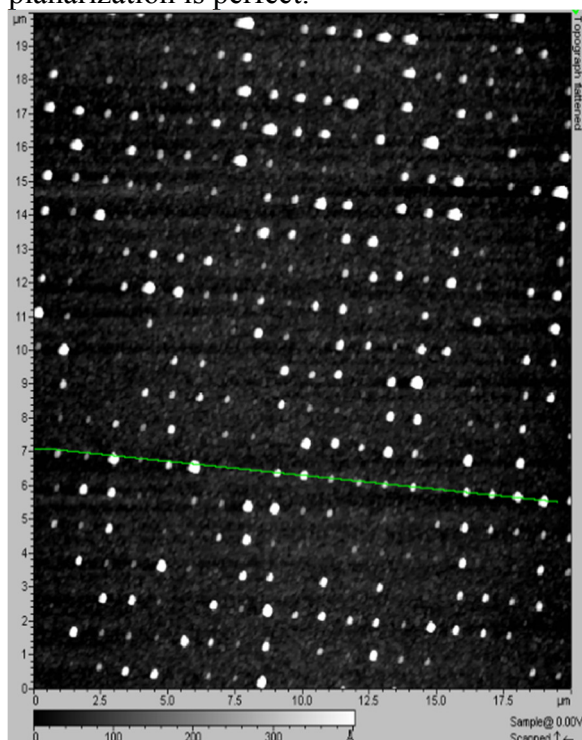


Figure 5.25 AFM image for character the surface profile of the cylinder array antenna after the planarization. The color bar is in unit of angstrom.

5.3.2. ITO deposition

Indium tin oxide (ITO) is a well-known metal oxide semiconductor which has been widely utilized as transparent conducting electrodes for various devices due to its high transmittance in the visible regime and good conductivity[88-90]. In our process, an ITO film is deposited by RF magnetic sputtering using an ITO target with a purity of 99.99% (weight percent of 10% SnO_2 and 90% In_2O_3). The reactive ions are generated by Ar plasma. For producing polycrystalline ITO film, a higher sputtering power will create a bigger grain size (normally refer to the width of a grain) which ensures a better conductivity. To avoid any possible delamination, a smaller sputtering power is suggested. Based on this purpose, we take a two steps ITO deposition. (1) We deposite a thin ITO film (around 10nm) with a small rate around 0.05 nm/s; (2) a second deposition (around 100nm) is applied with a higher rate around 0.25nm/s. In Fig 5.26, we show the surface profile of the ITO film. The average size(diameter) of the ITO grain is around 15nm, and the conductivity of the ITO film is around $1 \times 10^{-4} \Omega/\text{cm}$.

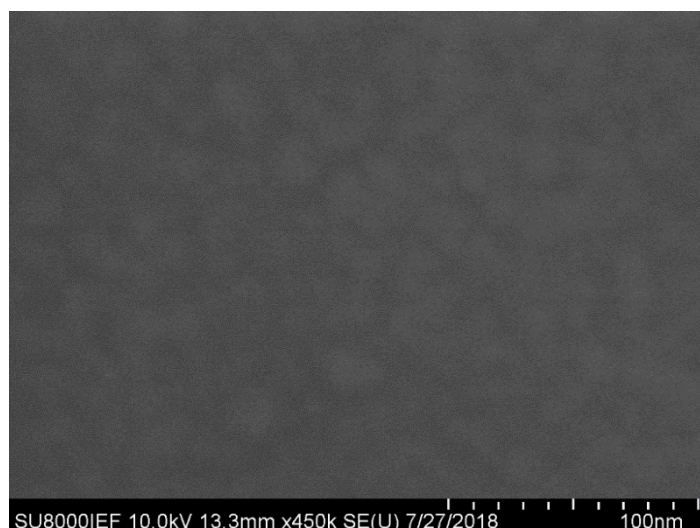


Figure 5.26 SEM image of an ITO film surface profile.

It is noticeable that the Ar plasma can be used as a common physical etching tool, for instance in ions beam etching. A strong ion plasma bombardment may yield defects or cracks which could short the circuit between the ITO and the Al electrode. Fig 5.27 shows cracks on the HSQ layer (more cracks can be seen on the Al strip) after we did the ITO deposition on a planarized junction. Because of the cracks, the device has been shorted.

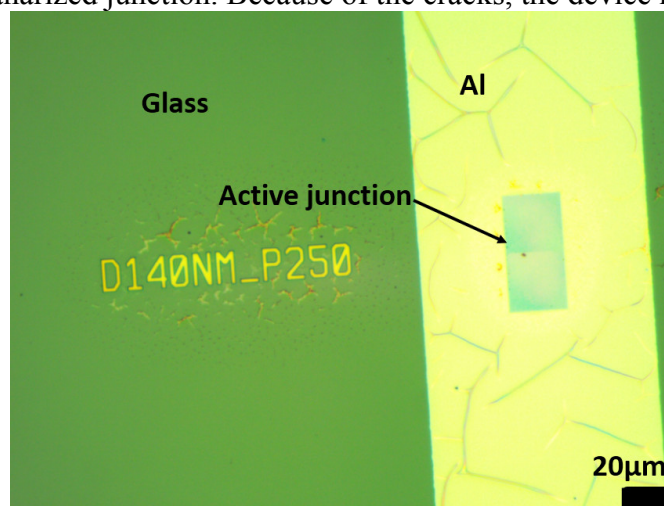


Figure 5.27 Optical image of a planarized junction after a direct ITO deposition.

To obtain a working top electrical contact for the cylinder antenna junction, a less ‘invasive’ way is suggested. PDMS elastomers have been widely adopted as a substrate material for producing lab-on-chip and microfluidic systems[91, 92]. A PDMS-based technique can be used to make a soft electrical contact as reported in reference [75, 93]. A PDMS substrate is prepared by a chemical synthesis between a base agent (sylgard 527) and a cross-linker agent (sylgard 184). To obtain a PDMS substrate with different elasticities, a ratio between the base and the curing agent should be modified. In principle, the elasticity increases and the viscosity decreases when the Young’s modulus of a PDMS substrate increases. In our case, we fabricate a more elastic PDMS stamp with a ratio of 10:1 (base agent: curing agent)[94]. To be composed with an ITO for an electrode, we deposit ITO on the PDMS surface.



Figure 5.28 A PDMS stamp is on a common glass slide

Thereafter, the basic arrangement of the top and the bottom electrode are shown in Fig 5.29, an ITO coated PDMS strip (1.5mm×18mm) is put directly on the active region. A droplet of silver paste has been permeated to one corner of the PDMS strip to connect the ITO electrode and the outlet connection wire.

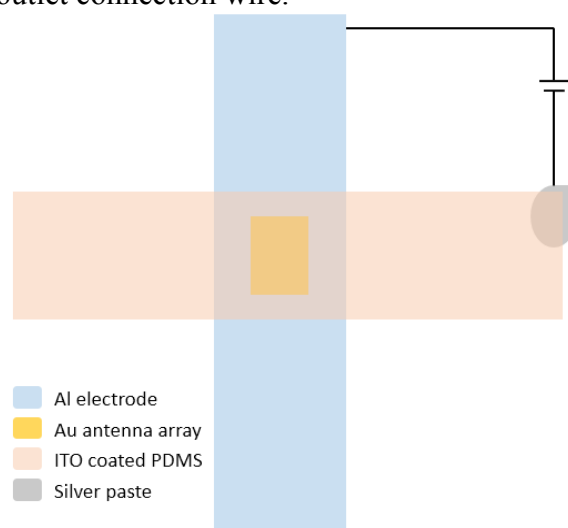


Figure 5.29 Schematic for showing the electrical connection of the cylindrical arrayed junction

Concerning a flexible PDMS substrate, the deposited ITO film on top might suffer some mechanical cracks. So we need carefully take care the ITO transfer for making a good contact; otherwise, the resistance of the top electrode could be significantly raised up (see Fig. 5.30). Herein, we suggest to put a piece of glass strip on the back side of the ITO coated PDMS for holding the substrate to avoid any big mechanical bending during the transfer.

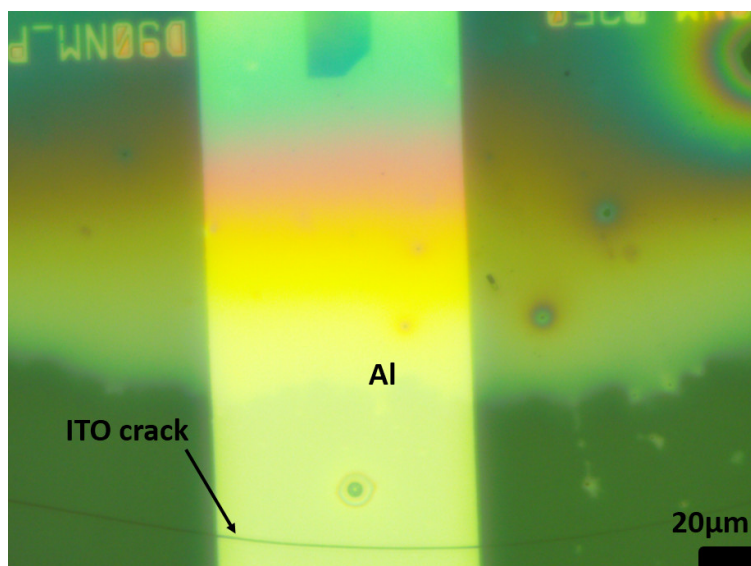


Figure 5.30 Optical image of the cylindrical antenna junction after applying a ‘soft’ ITO top contact. The narrow black line on the bottom is the crack pattern from the ITO film. The scale bar is 20 μm .

5.4. Conclusion

In this chapter, we have described the process for the fabrication of tunnel junctions with nanopatch antennas electrically connected. The goal was to obtain robust junctions operating at ambient temperature. Furthermore, fabricating a plasmonic resonator demanded a control of both the roughness and the geometrical width on the nanometer scale. Two different antenna, including a strip patch antenna and a cylindrical patch antenna, have been realized. We chose to use an AlOx barrier on Al. The Al bottom electrode is deposited by a standard UV photolithography. We thermally oxidize a thin Al film to generate 3 nm of AlOx layer to be used as a tunnel barrier. The top Au electrode is fabricated by e-beam lithography. To make an electrical contact for applying a voltage, we fabricate in-plane connection pads for the strip antenna junction; while for the cylindrical antenna junction, we use a planarization process to fabricate an insulating spacer and then put a ‘soft’ top contact by an ITO coated PDMS stamp. We have obtained a subnanometer roughness and we manage to fabricate a patch antenna with a width on the order of 100 nm over 60 μm length with a width fluctuation smaller than 10 nm. In the next chapter, we will show more details about the electrical and the optical characterization for these kinds of tunnel junctions. We have found that the junctions can be operated during several tens of hours at ambient temperature under 1.6V.

Chapter 6

SPP emission by inelastic tunneling with a resonant antenna

- 6.1. Introduction
 - 6.2. Experiment setup
 - 6.3. Electrical characteristic
 - 6.4. SPP emission characteristic
 - 6.5. Discussion and conclusion
-

6.1. Introduction

Electrical excitation a SPP can be done with a low energy of electrons. One possibility is using LED-based platforms[95-98]. However, the maximum modulation time scale of the device is limited by the spontaneous emission decay time which is on the order of 1 ns. Ultrafast emission can be achieved using light emission by inelastic tunneling (LEIT) through a tunnel junction. However, LEIT through a planar tunnel junction was proved to be an inefficient light emission procedure with a typical efficiency on the order of one photon per million electrons[1]. Despite this low efficiency, the signal can still be detected with standard detectors. Furthermore, LEIT has important advantages. Firstly, it is intrinsically fast. The fundamental limit is given by the tunneling time[34, 99] which is on the order of h/eV where e is the electron charge, V the applied voltage on the order of 1V and h is Planck's constant yielding a time limit on the order of 4 fs. In practice, the limit is given by the circuit time constant RC . Photon sources based on LEIT have been operated at 1 GHz[7]. Secondly, LEIT can be a highly localized source. The source current density can be confined in a nanoantenna or in a metallic tip enabling electromagnetic excitation localized at the nanometer scale. Both photon[22] and plasmon[18, 19, 100] emission have been reported using STM tips. More recently, surface plasmon emission has been reported with metallic microstructures[23] and molecular junctions[76]. Hence, antenna surface plasmon emission by inelastic tunneling (ASPEIT) appears to be a suitable candidate for ultrafast and highly localized plasmon emission.

However, several issues need to be addressed before ASPEIT can become a practical source. It is required to control the emission spectrum, the angular emission pattern and to increase significantly the emission efficiency. In order to tackle these issues, resonant nanoantennas can be used. The rationale for using an antenna is based on different properties. Firstly, a resonant antenna can select the frequency emission[38, 101, 102].

Secondly, with an antenna, the total emitted power can be increased by several orders of magnitude compared to a STM tip. Thirdly, a resonant antenna can be designed in order to control both the polarization and the angular emission pattern[31, 103]. Fourthly, a resonant plasmonic antenna contributes to the local density of states in the junction. If the contribution of the antenna mode is larger than the contribution of the non-radiative modes, it becomes possible to reduce quenching and therefore increase the radiative efficiency[38, 55, 104] in a controlled and deterministic way. It is important to stress that there is no fundamental limit to the LEIT efficiency. We note in particular that in the microwave regime the non-radiative modes can be suppressed using dissipation-less superconductors. Furthermore, impedance matching between the junction and a 50Ω line can be achieved by microwave engineering so that photon emission in a 50Ω line can reach very high efficiencies[105]. Photon emission in the visible by electrically driven optical antennas has been reported demonstrating a spectral control of the emission[26, 32] and also a directional control[33]. Spectral control of LEIT using resonant nanocubes has been demonstrated recently[81] although only a small fraction of the tunneling current was affected by the antenna. So far, surface plasmon emission by inelastic tunneling has received comparably less attention. Reported experiments are based on the use of a metallic tip[18, 19]. While it is known that a localized gap plasmon takes place between the tip and the surface, no control of this mode has been reported. It was proposed[38] to use antennas to engineer the plasmon mode in order to increase the efficiency and to control the emission spectrum. In this chapter, we report the characterization of antennas to emit surface plasmons propagating along an Al/air interface. The antenna produces a narrow emission spectrum, it provides a power in 10 pW regime which is 4 orders of magnitude larger than the typical fW power emitted by a STM tip and a more than 3 orders of magnitude enhancement of the efficiency compared to a planar junction.

6.2. Experiment setup

The electrical characterization of the ASPEIT junction is performed via a source-meter (Agilent B2902A). The IV measurements are conducted by a Quick IV Measurement software provided by keysight technologies website. For all experiments, the Au electrodes are grounded and the Al electrodes are biased. To avoid any possible dielectric breakdowns, the maximum voltage we applied is 1.8V. To avoid heating the junction, we use a pulsed voltage ($<1.7V$) with a time period of 3ms with 50% of duty cycle. When performing the electroluminescence (EL) measurement, we apply a lower voltage ($<1.6V$) to maintain a longlife measurement.

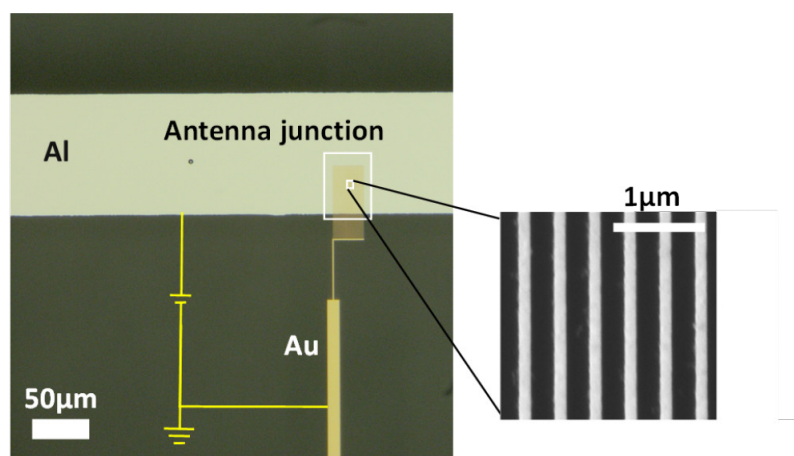


Figure 6.1. An optical microscope image shows the periodical antenna junction (inside the white square) and corresponding electrical circuit connection schematic. A SEM image shows a zoom of the array of linear antennas.

The optical characterization for the Al/AIOx/Au junction is based on leakage radiation microscopy (LRM) using an inverted optical microscope (Olympus X71). We use an oil objective (NA=1.3, X100) to collect the SPP emission through the glass substrate when the junctions are biased. The back focal plane imaging is schematically shown in Fig. 6.2(a). The real plane image can be captured by simply removing a lens. All the electroluminescence images are recorded with an electron multiplying CCD (EMCCD, Andor iXon 885) equipped with a water-cooling system. The integration time of the back focal plane and the real plane images of the antenna junction are 900s with an EM gain of 3. For the planar junction without antenna, we use an integration time of 3900 s with an EM gain of 200. Regarding the spectral measurement, the generated light is injected into a multimode fiber by an objective (NA=0.5) and then guided into a spectrometer (Shamrock 750i). The insert image in Fig. 6.2 (b) shows the quantum efficiency response of the spectrometer. It is seen the responsivity decreases when towards the infrared.

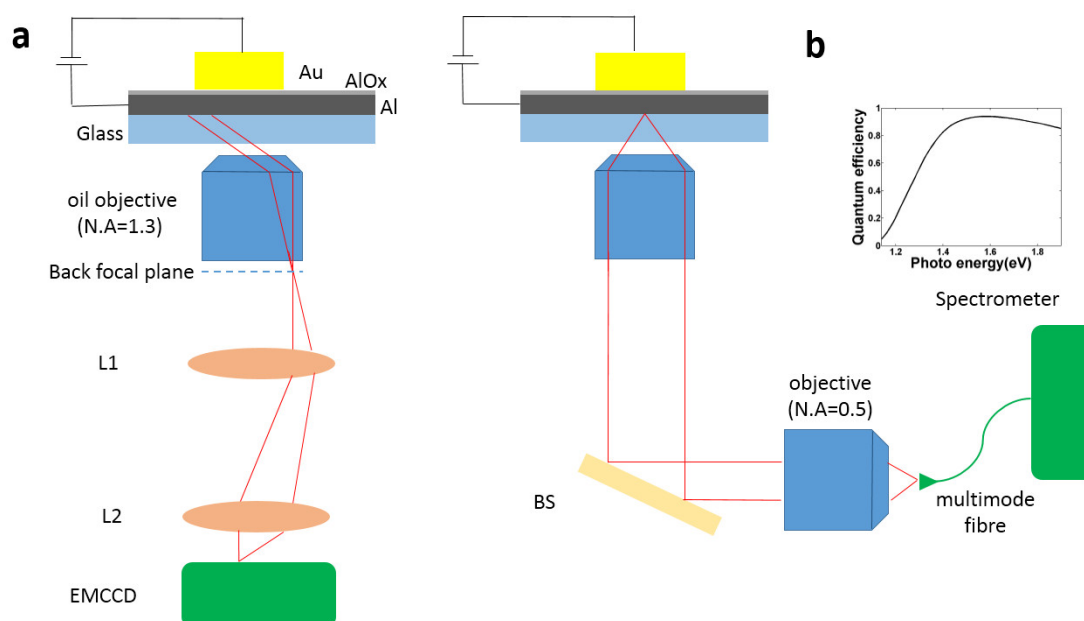


Figure 6.2. Schematic of the optical characterization setup. (a) Back focal plane imaging, the orange lines indicate the optical path. (for real plane imaging, lens L2 is removed). (b) Experimental setup for spectrum measurement. The insert shows the quantum efficiency of the spectrometer.

6.3. Electrical characteristic

The current-voltage characteristics are obtained at ambient conditions using the setup we described in the section 6.2. In order to check the device is operating in the tunnel regime, we have measured the current density (J) as a function of the applied voltage. As shown in Fig. 6.3, a non-linear curve displays in linear plot (Fig. 6.3a) and semi-log plot (Fig. 6.3b), which demonstrates the typical exponential dependence. To evaluate the width of the tunnel junction as well as the barrier height, we fit the data by using an analytical Simmons' model[40]. Seeing Fig. 6.3(a), a good fit can be obtained by using the following parameters: 3nm of the barrier thickness and mean barrier height with $2.01\text{eV}\pm 0.03\text{eV}$ by using an effective mass of the electron of $0.23 m_e$ [106]. Note that our antenna junction area is much bigger than a standard STM-based junction, so that the tunneling current is over three orders of magnitude larger than the STM-based junction (usually a few nA).

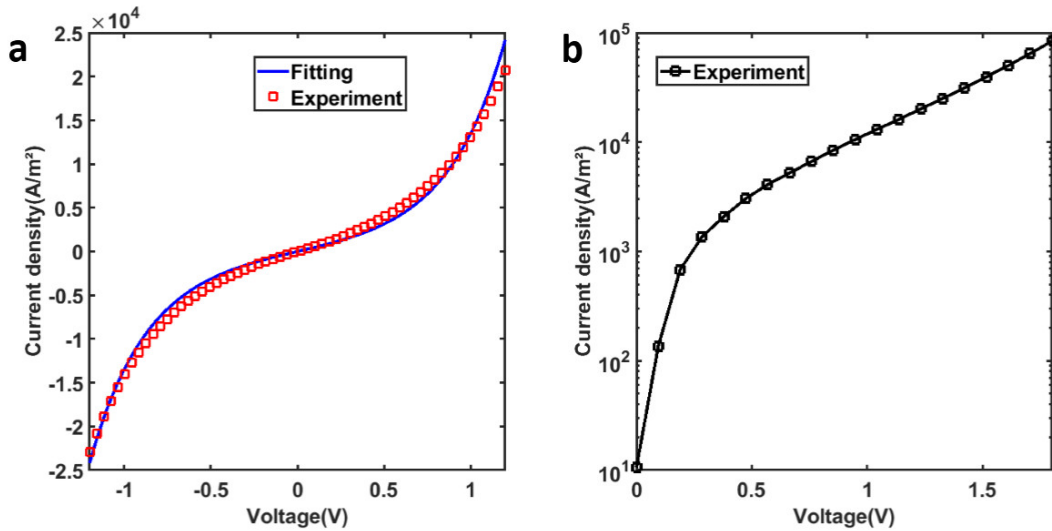


Figure 6.3. $J(V)$ characteristic of ASPEIT junction. (a) Red dots: $J(V)$ experimental data, blue line: fitted curve based on the Simmons model (Fitting parameters: barrier thickness of 3nm and mean barrier height of $2.01\text{eV}\pm 0.03\text{eV}$, effective electron mass $0.23m_e$). (b) Semi-log plot of $J(V)$ showing the exponential behaviour.

In order to further check that our ASPEIT junction is in the tunnel regime, we measured the characteristic $J(V)$ curve of the device by varying the a range of temperature from 60K to 300K. We put the device in a cryo system (Cryostat OptiDry 150) and made five measurements. As shown in Fig. 6.4, it is clearly seen that the $J(V)$ is weekly temperature dependent which confirms that the junction is in the tunnel regime with a good quality of barrier.

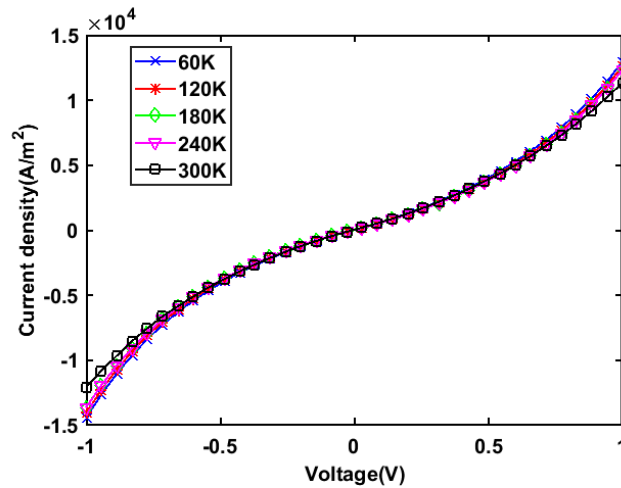


Figure 6.4. $J(V)$ characterization by varying the temperature. We recorded 5 $J(V)$ curves in a temperature range varying from 60K to 300K with a step of 60K.

Using a large-area Al/AlO_x/Au tunnel junction with a high bias voltage at ambient temperature is difficult because of the electrical breakdown[1, 107]. A poor heat dissipation efficiency decreases the lifetime of the junction. To avoid electrical breakdown at relatively high voltage, for instance at 1.6V, we used a pulsed voltage (1.5ms width and duty cycle of 50%) to bias the junction in order to let the system cool down.

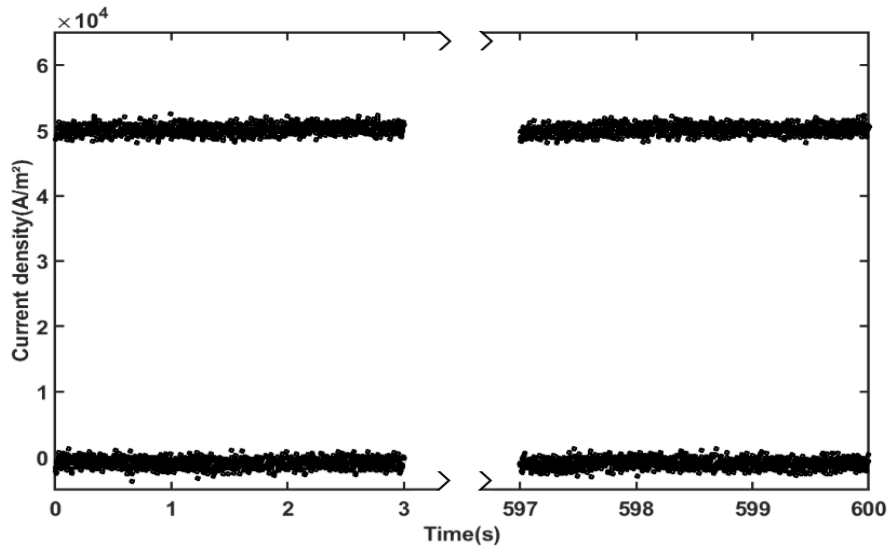


Figure 6.5. Current stability of the tunneling current density over 10 minutes when applying a square-shape pulsed voltage (peak value= 1.6V; base value=0V) with period 3 ms and duty cycle 50%.

We have studied the electrical stability of the junction by recording the tunneling current during 10 minutes with a bias voltage of 1.6 V. As seen in Fig. 6.5, the current density is stable around a value of $5 \times 10^4 \text{ A/m}^2$ (except small fluctuations at some points), showing that the junction is electrically stable.

6.4. SPP emission characterization

We now turn to the optical characterization of ASPEIT. The optical observation of the SPPs emitted by the Al/AlO_x/Au junction is based on leakage radiation microscopy (LRM) using an inverted optical microscope. We use an oil objective (NA=1.3) to collect the leakage of the emitted SPPs through the glass substrate when the junctions are biased. We show in Fig. 6.6a, an optical microscope image of the device taken through the glass substrate. The bright area in the center corresponds to the array of antennas with a width of 25 μm . The direction of the antennas is along the y-axis. It is seen that on both sides of the array of antennas, light is also collected. This is due to radiative leakage of surface plasmons propagating away from the antennas. To prove the plasmonic character of the emitted light, we averaged the intensity along y in the area indicated by the dashed rectangle shown in Fig. 3a. The result is plotted as a function of x in Fig. 6.6b in semi-log scale showing clearly an exponential decay with a decay length of 4.9 μm . It matches qualitatively by taking the theoretical value at 850nm which is 8.5 μm [108]. To further check the plasmonic character of the emitted light, we recorded the far-field angular spectrum in the back focal plane as displayed in Fig. 6.6c. It is clearly seen that light is predominantly emitted for wavevectors slightly larger than the vacuum wavevector $k_0=\omega/c$, a clear signature of surface plasmons propagating along an Al/air interface. Furthermore, an interesting non-uniform intensity pattern due to the antenna periodicity is observed as a function of the angle. In order to interpret this, we use the theoretical model developed in the section 2.2.

We compute the light emission due to the SPP leakage through the substrate side by using the reciprocity theorem. We consider the reciprocal situation and illuminate the ASPEIT junction by a plane wave through the substrate side. We consider one fixed position in the middle of the tunnel barrier (we assume the field along the z-direction of AlO_x layer is homogeneous). In order to compute the power emitted in a particular direction, we compute the corresponding enhancement factor. To proceed, we illuminate with a plane wave coming from this direction specified by a polar angle varying from 0° to 60° (with 70 points, which corresponds to the numerical aperture of the objective), and an azimuthal angle varying from 0° to 360° (with 200 points). Furthermore, we average the intensity enhancement factor over the width of the antenna using 15 points. In Fig. 6.6d, we calculate the angular emission pattern by the ASPEIT which is in good agreement with the experimental data.

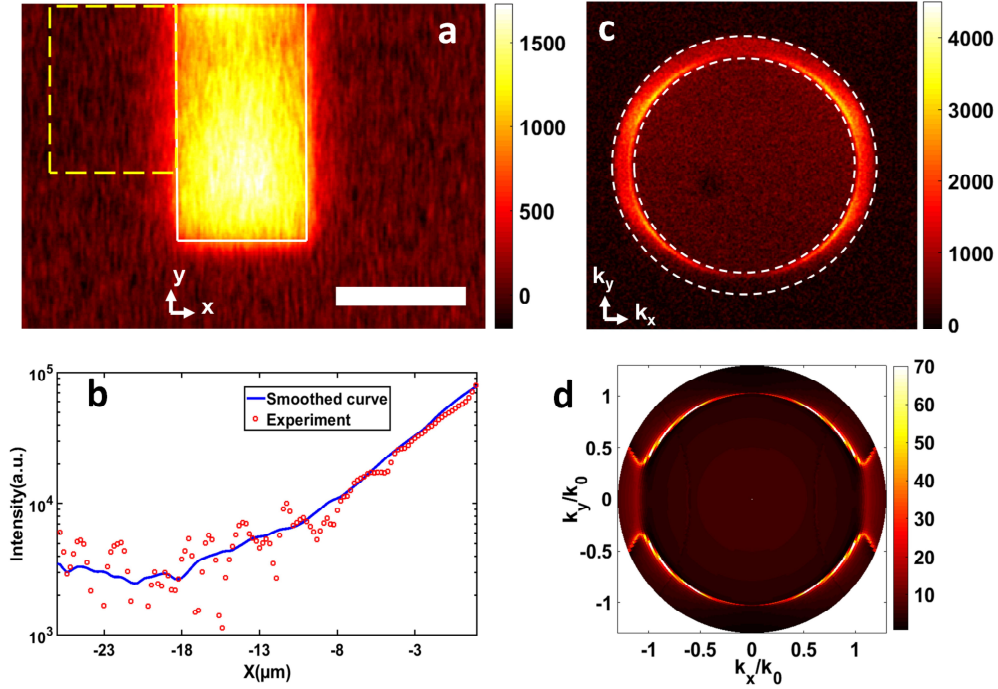


Figure 6.6. Plasmon emission. (a) Image of the source plane showing the electrical excitation of SPP (under a biased voltage of 1.6V). The white rectangle indicates the area of the array of antennas (the scale bar is $25\mu\text{m}$). (b) Cross-section profile along the x-axis in a semi-log plot is averaged over the y-axis in the yellow dashed line rectangle, (red dots are experiment data, the blue smoothed curve is a guide to the eye to see the SPP profile, the propagation length of the SPP is $4.9\mu\text{m}\pm 0.3\mu\text{m}$). (c) Experimental back focal plane image, the inner and outer dot circle correspond to $k/k_0=1.0$ (light cone in air) and $k/k_0=1.3$ (immersion objective numerical aperture), respectively; where $k_0=\omega/c$ and $k^2=k_x^2+k_y^2$, $k_x=n k_0 \sin\theta \cos\phi$ where $n=1.5$ is the refractive index of the substrate. (d) Simulated back focal plane image (at wavelength of 850 nm and the width of patch is 132nm).

We now study the spectrum of the ASPEIT. To proceed, we collect the signal emitted towards the substrate and send it to a spectrometer (Andor Shamrock 750i). The data are shown in Fig. 6.7(a-c) and the theoretical simulations are shown in Fig. 4 (d-f) for three different bias voltages 1.4, 1.5 and 1.6 V. Note that the calculations account for the detector responsivity, responsible for the decay of the signal at low energy. We observe two spectral peaks at 1.2 and 1.5 eV that are well recovered by the model. Here, we see the ability of the antenna to control the light emission spectrum. We note that to recover the spectrum shape and width, we had to average over different antenna widths in order to account for width fluctuations of the antenna (reported in chapter 5). The two peaks correspond to the two modes of the Fabry-Perot cavity shown in Fig. 6.7(g-h). A cutoff of light emission is expected around eV/h (indicated by a vertical dashed line in Fig. 6.7 a-f) for inelastic light emission but not observed. The spectrum is significantly broadened and shifted from the theoretical eV/h value by the finite temperature (300 K) and by the antenna resonance. For the sake of comparison, we plot in Fig. 6.7(d-f) the theoretical emission spectrum of a planar junction at three different voltages multiplied by a factor of 500. This shows the two roles of the antenna: spectral control and efficiency enhancement.

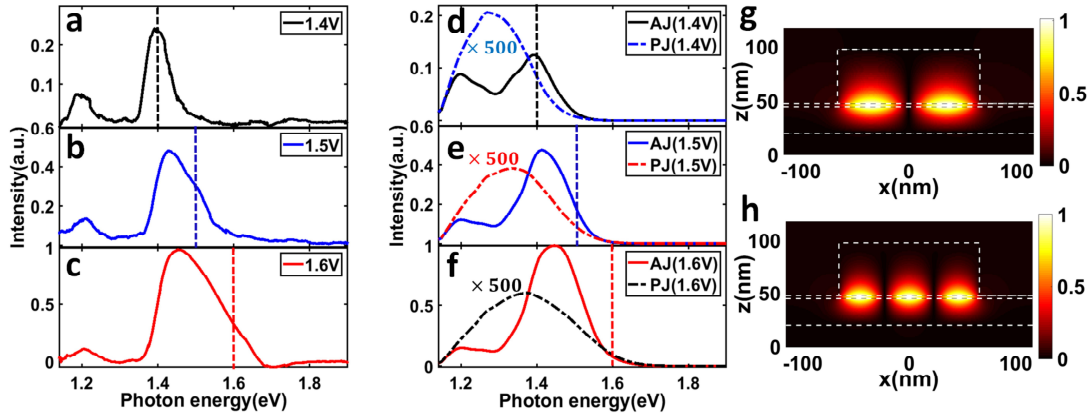


Figure 6.7. Controlling the emission spectrum. (a-c) Experimental SPP emission spectra at 3 different biases (1.4V to 1.6V, width of patch is around 128nm, period of patch is 400nm, Spectra intensity have been normalized by the maximum power with the bias of 1.6V); (d-f) Theoretical normalized SPP emission spectra with same bias voltage as the figures (a-c). The emission spectrum shows two spectral peaks due to the excitation of two resonant modes of the antenna. The peaks are broadened due to the inhomogeneity of the antenna width. The simulations result from an average over 7 different widths varying from 116 to 140 nm to account for width fluctuations along the wires in the experiments. The dotted line in each figure shows the corresponding normalized spectrum from a planar junction with the same voltage bias (intensity of the spectra has been multiplied by a factor of 500). All the theoretical emission spectra are corrected by the quantum efficiency of the spectrometer responsible for the decay at low energies (g-h) Theoretical magnetic field distribution [109] (H_y in the X-Z plane) of the two gap modes of a 132 nm wide antenna corresponding to the lower photon energy at 1.2eV, (g) and the higher photon energy at 1.5eV, (h).

A key property of LEIT is a temperature-dependent cutoff close to eV/h due to energy conservation. Since our experiments are performed at ambient temperature, the Fermi-Dirac distribution is broadened by an amount on the order of a few $k_B T$. In particular, the cutoff at eV/h is smoothed. In addition, the resonance of the antenna enhances the emission beyond the cutoff resulting in a low visibility of the cutoff. We show in Fig. 6.8 the calculated form of the spectrum at 0K where it is seen that the cutoff at high energy depends on the applied voltage. We conclude that the lack of clear cutoff in our experiments results from the enhancement due to the antenna of the spectral tail of the current fluctuation spectrum due to the finite temperature.

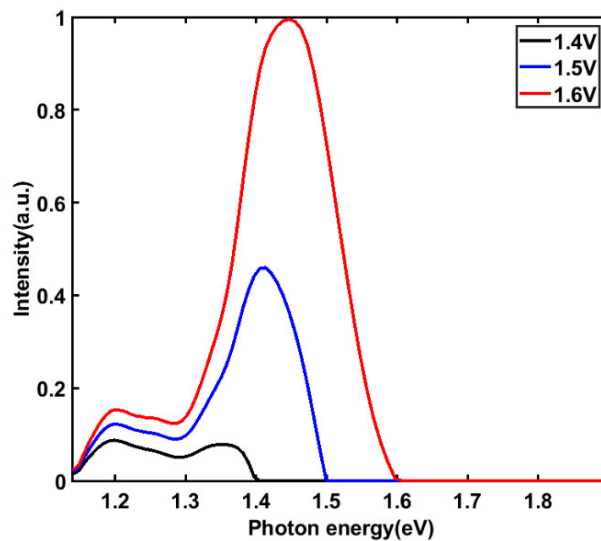


Figure 6.8 Theoretical electroluminescence spectra (the same spectra as the figure 6.6(a-c) with $k_B T \rightarrow 0$) are shown with 3 different biased voltages from 1.4V-1.6V.

It is well known that plasmonic patch antenna can be used to control the emission spectrum by simply modifying the parameters of the antenna[58, 59]. We show in Fig. 6.9, that the emission spectrum varies when the width of the patch antenna varies from 130nm to 220nm as expected from a Fabry-Perot cavity. A redshift is observed for the second order gap mode. Here, we show the spectra without averaging over different widths. It is clearly seen that the spectra are narrower than the spectra measured experimentally. As we have considered a voltage at 1.6V, the spectrum vanishes at energies larger than 1.6eV.

When comparing the three resonant peaks, we observe an amplitude variation. Close to the cutoff eV/h , the amplitude decreases as expected. At lower frequencies, the emitted signal decreases because spontaneous emission rate decays and also because aluminium has larger losses. Additionally, a small shoulder appears around 1.40eV. The position of the shoulder depends on the period of the antenna arrays so that we attribute it to a grating mode. Since the fabricated array of antennas is finite, this collective mode is too weak to be observed.

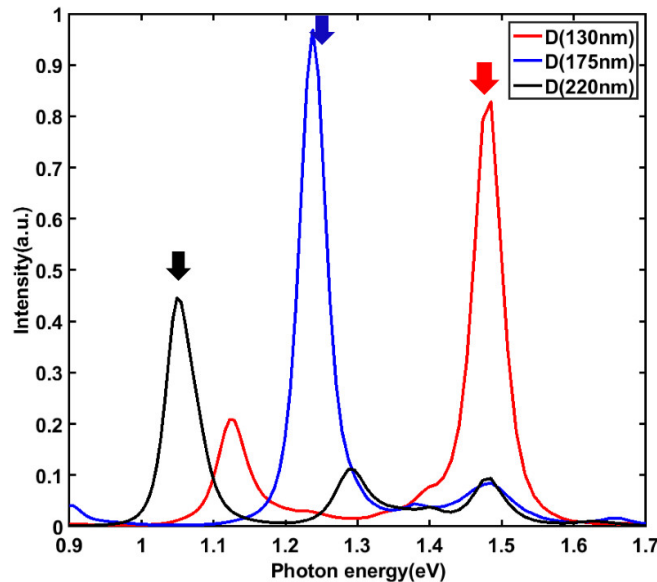


Figure 6.9. Simulated spectra at voltage bias of 1.6V for the ASPEIT junction by varying patch width from 130nm, 175nm to 220nm. The vertical arrows show the resonance position of the second-order gap modes.

We now move to the study of the polarization emission properties of the ASPEIT. Fig. 6.10 shows the far-field emission of the device when using an analyzer aligned perpendicular to the antennas (0°) or parallel to the antennas (90°). It is seen that the signal drops significantly at the emission peak showing that light emission by the antennas is polarized. The far-field emission pattern confirms that this polarization behavior is due to the plasmons. Fig. 6.10(b-c) show the back focal plane image for two orientations of the analyzer. Fig. 6.10(d-e) show the corresponding theoretical emission. we find good agreements except a discrepancy between Fig. 6.10 (c) and Fig. 6.10 (e) regarding the photon part of signal. Since our source in experiment has a finite size, the difference is observed not for leaky plasmon but for photons due to scattering of plasmons at the edge of the structure. Thus, it could reduce the contrast of photon signal part. However, in our model, the finite size of the source was not included.

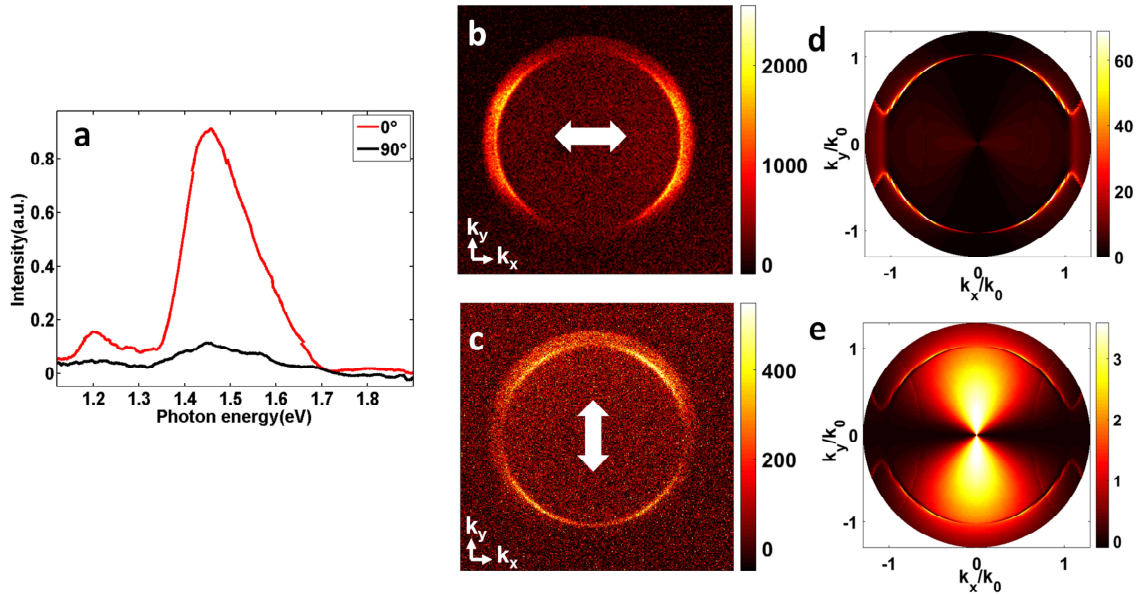


Figure 6.10. Polarization-dependence of the ASPEIT junction. (a) SPP emission spectra with 2 different polarized directions (0° stands for the direction which is perpendicular to the long wire patch antenna, while 90° stands for the direction which is parallel to the wire.) (b-c) Back focal plane image with two different polarization direction of 0° and 90° (the white arrows indicate the polarization direction). (d-e) simulated back focal plane images (at wavelength of 850nm) associated with the figure (b-c). Note that all the images in (b-e) are plotted at a log-scale.

6.5. Discussion and conclusion

An important figure of merit of an electrical surface plasmon source is the emitted power. Towards a practical source, we need the device to emit more plasmons. We detected 3.6×10^6 photons per second which is corresponding to 1×10^8 photons emitted per second after correcting for the collection efficiency of our optical system. This gives a power around 23 pW by using a photon energy of 1.45eV. We compare with a STM-based junction[18] (10^4 photons per second, corresponding to 3 fW), and a planar junction[23] (4.3×10^5 photons per second, corresponding to 100 fW). We note that the increased emitted power is both due to a larger size of our device ($25\mu\text{m} \times 45\mu\text{m}$) and to the efficiency enhancement of LEIT.

As already mentioned, the low efficiency of the inelastic tunneling is due to the fact that the photonic local density of states in a tunnel junction is dominated by non-radiative modes. The key to increase the efficiency is therefore to design a plasmonic antenna with a resonant plasmon mode fulfilling two conditions[38], i) it provides a contribution to the local density of states larger than the non-radiative modes, ii) its losses are dominated by radiative losses. We designed our antennas to fulfill these criteria. In order to measure the efficiency enhancement, we have compared the emission by the array of antennas with the emission of the same sample at a different position with no antennas. Light emission by a bare junction formed by the intersection between an Au stripe (width $10\mu\text{m}$, thickness 50nm) and an Al stripe (width $100\mu\text{m}$, thickness 25nm), under a bias of 1.6V, is shown in Fig. 6.11. It is seen that close to the edges, emission is largely enhanced compared to the central area due to plasmon scattering. In order to extract photon emission only, we measured the power emitted in the intersection excluding the edges $20\mu\text{m}$ from both

sides, see the yellow dashed rectangle in Fig. 6.11. We found an averaged efficiency of 6.0×10^{-10} photons per electron. This low efficiency is due to the low transmission of the 25 nm thick Al layer in the near infrared and also to the good quality of the surface, whose roughness is lower than 1 nm. Such a low roughness is required in order to fabricate a good plasmonic cavity. We now compare with the efficiency of light emitted by the area covered with antennas shown in Fig. 6.6a. The optical power is integrated over the array of antennas (dashed rectangular region in Fig. 6.6a) and normalized by the corresponding intensity assuming that the current density is uniform. We found 1.6×10^{-6} photons per electron indicating a 2700 efficiency enhancement compared to the planar junction.

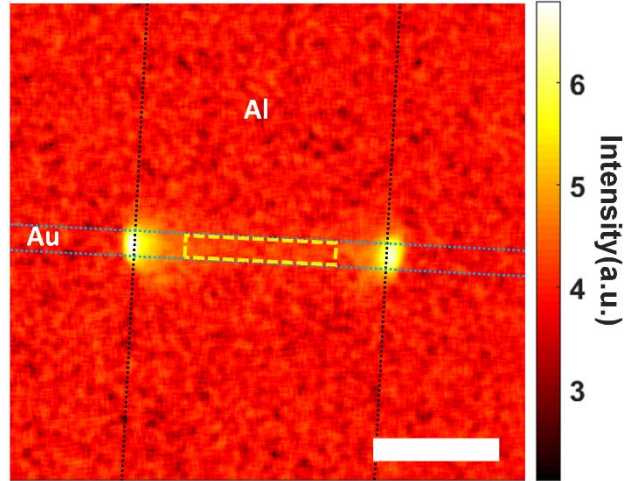


Figure 6.11. Light emission from a macroscopic planar junction. Microscope optical image of a rectangular ($10\mu\text{m} \times 100\mu\text{m}$) planar junction at the crossing of an Al stripe and an Au stripe. Black and blue dashed lines are showing the edge of Al and Au electrode respectively. Scale bar is $50\mu\text{m}$. Color bar is in log-scale.

To analyse what are the key factors playing a role in this enhancement, we use the theoretical model of light emission by an antenna developed in the section 2.2 of chapter 2. We compute the fields emitted by a fluctuating current density in the tunneling gap. The power spectral density of the current fluctuations is given by[35]:

$$\langle I^2 \rangle(\omega) = \frac{1}{1 - \exp(-\frac{eV}{k_B T} (1 - \frac{\hbar\omega}{eV}))} eI_0 (1 - \frac{\hbar\omega}{eV}), \quad (6-1)$$

where I_0 is the tunneling current, e is the electron charge, ω is the frequency, \hbar is the reduced Planck's constant, k_B is Boltzmann's constant, and T is temperature. To compute the emitted field, we use the reciprocity theorem[110]. The efficiency defined as the number of emitted photons due to plasmon leakage per electron can be cast in the form:

$$\eta_{e-p}(\omega_0) = \left[\frac{Z_0}{R_k} \right] \frac{\Delta\omega}{\omega_0} \frac{n}{4} \left(\frac{t}{\lambda_0} \right)^2 \overline{|K^l(\mathbf{u}, \omega_0)|^2} \frac{\langle I^2 \rangle(\omega_0)}{eI_0} \Delta\Omega, \quad (6-2)$$

where $R_K = h/e^2$ is the quantum of resistance, $Z_0 = \mu_0 c$ is the vacuum impedance, c is light

speed, t is the barrier thickness, λ_0 and ω_0 are the central wavelength and central frequency of a resonant antenna, $\Delta\Omega$ is the related solid angle, $\Delta\omega$ is the spectral width of the emitted peak, and $\overline{|K^l(\mathbf{u}, \omega_0)|^2}$ is the averaged field enhancement factor (with corresponding polarization and emission direction) over the whole junction barrier. It is defined as the ratio of the electric field in the junction and the electric field of an incident plane wave coming from the substrate in the emission direction. The quantity $nZ_0(t/\lambda)^2 \langle I^2 \rangle(\omega)$ is essentially the power radiated by a dipole with length t in a homogeneous medium with refractive index n . The role of the antenna appears in the spectrally dependent factor $\overline{|K^l(\mathbf{u}, \omega_0)|^2}$. For an angle, polarization and frequency corresponding to the resonant excitation of a plasmon, it takes the value 5×10^{-3} for a planar junction due to the low transmission through the 25nm thick aluminium layer. However, it is on the order of 70 in the presence of the resonant antenna. It is seen that this factor is the key to improve the efficiency by increasing the field in the junction using the antenna.

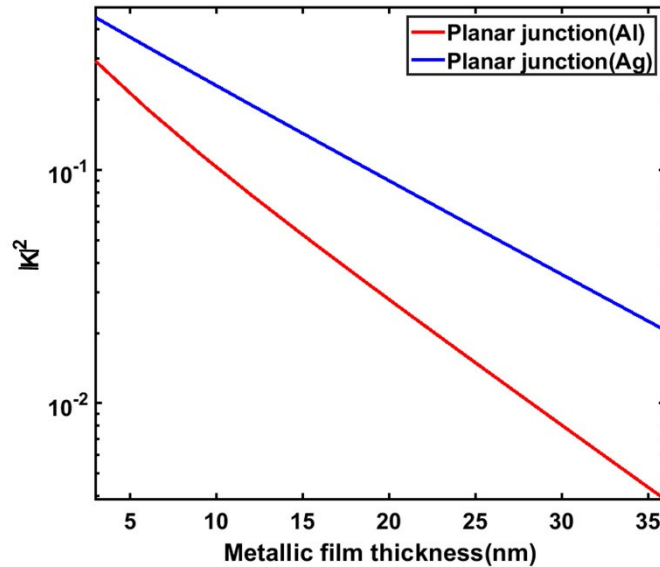


Figure 6.12. Semi-log plot of $|K|^2$ ($\lambda = 850\text{nm}$), inside the barrier layer of the Al/AlOx(3nm)/Au(50nm) planar junction (red curve) and the Ag/AlOx(3nm)/Ag(50nm) planar junction (blue curve), are expressed as a function of the thickness of bottom electrode. Note the $|K|^2$ has been integrated over the collection solid angle.

As we have mentioned, the efficiency can be improved by tailoring the enhancement factor $|K|^2$. Here we discuss the impact of the bottom electrode thickness on this factor.

The semi-log plot clearly shows the exponential dependence of $|K|^2$ as a function of the thickness. It is clearly seen that the electron to photon conversion efficiency decreases when increasing the bottom metal thickness. The relatively large thickness of aluminium explains the low photon output in our experiment. This plot shows that the plasmon to photon conversion decays exponentially with the metal thickness. This plot suggests that the electron to plasmon conversion is larger than the electron to photon conversion by at least one order of magnitude.

Replacing the electrode materials with a low-loss metal can reduce the intrinsic losses in the electrodes and thus increase the efficiency. We now study the photon emission of an

antenna junction based on the Ag/AlOx/Ag configuration. We use the dielectric function of Ag from the reference[24]. As shown in Fig. 6.13, the power emitted on resonance integrated over the collection solid angle is enhanced by a factor of roughly 50 with respect to the Al-based antenna mode. The linewidth of the Ag-based junction presents nearly 1/3 of the Al-based junction.

We now turn to estimate the electron to photon conversion efficiency with a silver antenna as follows. We compute theoretically the efficiency using either silver or aluminium and gold as in the experiment. Thus, we define an enhancement factor that is multiplied by the experimental efficiency. This procedure yields an estimated efficiency of 1.4×10^{-5} . We thus conclude that the electron to plasmon conversion can be larger than 10^{-4} for a silver antenna on silver substrate.

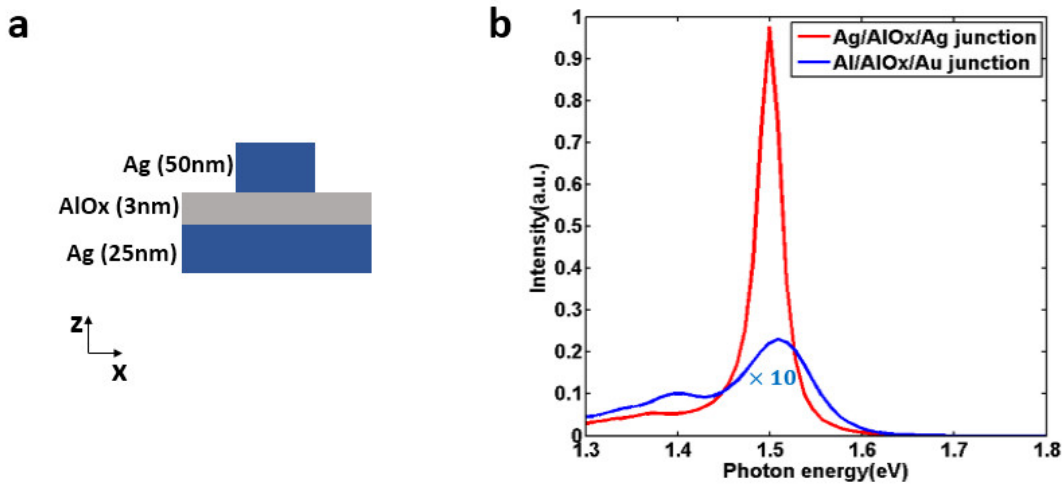


Figure 6.13. (a) Schematic of the Ag/AlOx/Ag antenna junction. (b) The normalized photon emission spectrum between the Ag/AlOx/Ag junction and the Al/AlOx/Au with the same geometry (width=124nm) at a voltage bias of 1.6V. The spectrum of Al-based junction has been multiplied by a factor of 10. Note: the period of arrayed antenna is fixed at 400nm, and the dielectric function of Ag is taken from reference[24].

As shown before, the theoretical model predicts correctly the emission spectrum, the angular emission pattern and the polarization. However, the photon per electron efficiency is only qualitatively predicted. The theoretical model predicts an antenna efficiency of 1.1×10^{-7} (under a voltage of 1.6V) which is one order magnitude lower than the experimental value 1.6×10^{-6} . We also find a difference for the antenna junction efficiency normalized by the planar junction efficiency. The experimental value is 2700 whereas the model predicts 400. We attribute this difference to the simplified model of the current fluctuation correlation function used. It has already been reported in the literature[17, 111] that this model underestimates the efficiency. In summary, the antenna appears to be a powerful tool to enhance the efficiency of LEIT, which has been known for decades to be an inefficient light emission process.

In conclusion, we have reported antenna surface plasmon emission by inelastic tunneling. We have shown that the emission spectrum can be tuned by varying the width of the antenna. An important feature of the antenna is its ability to enhance the efficiency of the coupling between electrons and plasmons. The emitted power of the ASPEIT is demonstrated to operate at 10 pW regime instead of a few fW for a STM-based junction. In terms of the efficiency, we have demonstrated a more than three orders of magnitude

enhancement by using ASPEIT. We have introduced a theoretical model of ASPEIT that accounts for the observed spectrum, polarization structure and is able to predict the efficiency enhancement. This model provides guidance to further improve the efficiency. Despite the use of an antenna, the electron to photon efficiency of source is only 1.6×10^{-6} , due to the large losses of aluminium in the near infrared. Using our model, we find that a silver/alumina/silver junction could reach an efficiency of 1.4×10^{-5} photons per electron. This raises the prospect of an efficient, ultrafast and highly localized electric surface plasmon source.

Chapter 7

Conclusion and outlook

7.1. Conclusion

7.2. Outlook

7.1. Conclusion

In this manuscript, we have studied both theoretically and experimentally SPP emission by inelastic tunneling electrons in an antenna tunnel junction. We briefly summarize the main results in this section.

In chapter 2, we have used two different presentations to describe the light emission in a tunnel junction. The first approach is based on the fluctuation dissipation theorem. We have shown that a large field enhancement $|K|^2$ in the barrier provides a larger light emission. We have also derived an explicit form of the electron to plasmon conversion efficiency. The second view is based on the Fermi golden rule for inelastic tunneling and put forward the local density of states and the antenna efficiency as key parameters. We have shown that the two approaches are equivalent by deriving the link between the local enhancement rate and the local density of states. More generally, this chapter points out why an antenna can be used to increase light emission and electron to plasmon efficiency.

In chapter 3, we have addressed the SPP emission in a STM configuration. We have theoretically demonstrated that the SPP emission can be enhanced by using a nanorod or a nanocone between a STM tip and a metallic film. The key difference with the STM tip is the presence of a localized gap mode with a large density of states. Furthermore, the antenna mode of the nanorod and the nanocone are coupled to the gap mode and radiate much more efficiently. Quantitatively, we find that two orders of magnitude SPP emission enhancement can be obtained by using a nanorod and almost three orders of magnitude SPP emission enhancement by using a nanocone.

In chapter 4, we present a theoretical study of SPP emission from MIM nanopatch antennas with sub-nm gaps. A major difference with the previous case (STM, nanocone, nanorod) is that the number of electronic channels is much larger and therefore, the total emitted power is much larger. Roughly speaking, there is only one channel for electrical conduction in a STM and there are A/λ_F^2 channels in a MIM patch antenna where A is the MIM area and λ_F is the Fermi wavelength on the order of 0.1 nm. The key message is the identification of a hybrid mode resulting from the strong coupling between a gap mode that yields a large contribution to the LDOS and an antenna mode that is able to efficiently couple to SPPs. We found that the total SPP emission can be largely enhanced.

Furthermore, we have shown that the antenna emits as many photons than plasmons when the surrounding medium is air. However, when increasing the refractive index of the surrounding medium, more power is emitted into plasmons and the plasmonic efficiency can be improved up to 30% with a gap of 1nm at a working wavelength around 800nm.

In chapter 5, we have summarized the process developed for the fabrication of tunnel junctions with nanopatch antennas electrically connected. The goal was to obtain robust junctions operating at ambient temperature. Furthermore, fabricating a plasmonic resonator demanded a control of both the roughness and the geometrical width on the nanometer scale. Two different types of antenna, a strip patch antenna and a cylindrical patch antenna, have been realized. We chose to use an AlO_x barrier on Al. The Al bottom electrode is deposited by a standard UV photolithography. We thermally oxidize a thin Al film to generate 3 nm of AlO_x layer to be used as a tunnel barrier. The top Au electrode is fabricated by e-beam lithography. To make an electrical contact for applying a voltage, we fabricate in-plane connection pads for the strip antenna junction; while for the cylindrical antenna junction, we use a planarization process to fabricate an insulating spacer and then put a ‘soft’ top contact by an ITO coated PDMS stamp. We have obtained a subnanometer roughness and we manage to fabricate a patch antenna with a width on the order of 100 nm over 60 μm length with a width fluctuation smaller than 10 nm.

In chapter 6, we have reported the experiments on antenna surface plasmon emission by inelastic tunneling (ASPEIT). We have shown that the emission spectrum can be tuned by varying the width of the antenna. An important feature of the antenna is its ability to enhance the emitted power and the efficiency of the coupling between electrons and plasmons. The emitted power of the ASPEIT is demonstrated to operate in the 10 pW regime instead of a few fW for a standard STM-based junction. In terms of efficiency, we have demonstrated a more than three orders of magnitude enhancement over a planar junction by using ASPEIT. Using the model developed in Chapter 2, we theoretically reproduce the observed spectrum, polarization structure and predict the efficiency enhancement. This model provides guidance to further improve the efficiency. Despite the use of an antenna, the electron to *photon* efficiency of source is only 1.6×10^{-6} , due to the large losses of aluminium in the near infrared. Using our model, we find that a silver/alumina/silver junction could reach an efficiency of 1.4×10^{-5} photons per electron. This raises the prospect of an efficient, ultrafast and highly localized electric surface plasmon source.

7.2. Outlook

SPP emission from the cylindrical antenna tunnel junction

We have fabricated two types of antenna junction. The strip antenna junction has been demonstrated to have stable electrical and optical properties in Chapter 6. However, for the cylindrical antenna junction, we find its electrical property (IV characteristic) is highly perturbed by the ‘flabby’ ITO top electrical contact. As shown in Fig. 7.1, the tunnel current oscillates when the voltage is larger than 1.7V. We attribute this instability to an unstable electrical contact between the ITO film and the antenna array when a bigger thermal heating dissipates through the ITO film. We also find the tunnel current decreases after a voltage bias with a long time (a few minutes).

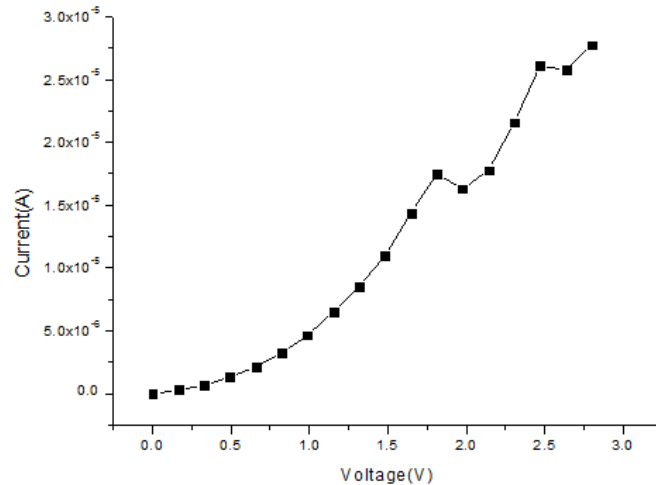


Figure 7.1. IV curve (0V~2.8V) for an arrayed cylinder tunnel junction. Note each voltage step takes 1.5ms.

A similar device has been reported by coating the EGaIn (so-called ‘liquid metal’) solution onto a PDMS stamp to be used as a top electrical contact[93]. This opens up an alternative way to electrically connect the cylindrical antenna junction. More fabrications and experiments are needed to solve this issue. We expect to observe a better electron-to-plasmon conversion efficiency with the cylindrical antenna thanks to the hybrid-coupling mode based on the mechanism reported in chapter 4.

Possible revision for the current correlation function in a tunnel junction

We have reported in chapter 6 that we find a theoretical efficiency one order of magnitude lower than the experimental data when we consider a simplified current correlation function in the tunnel barrier. A similar issue has been mentioned in the past [17, 111]. This discrepancy motivated the introduction of the hot electron mechanism as opposed to the inelastic tunneling picture. We stress that both in our work and in the experiments by Kirtley, a resonant plasmonic structure was used as opposed to a simple planar junction. In other words, the electromagnetic plasmonic mode is less confined close to the barrier in these two works. Since the thickness of the Au electrode is close to the Au electronic mean free path (around 40nm), it is reasonable to consider the current fluctuation in the electrodes. This raises the question of a proper description of the coupling between the antenna mode and the current fluctuation in the entire device. Our point of view is that the mechanism of radiation of current in the antenna and inelastic tunneling associated with radiation in the barrier should not be opposed. Rather, a new model is needed to account for the coupling between the current and the plasmonic mode in the device. This includes both the barrier and the antenna. Such a model requires a modified current correlation function which correctly account for the phase of the current throughout the device. Alternatively, it is possible to revisit the matrix element in the Fermi golden rule approach.

Possible correlated photon pairs generation from an antenna tunnel junction

Correlated photon pairs generation at the nanoscale is one of the key platforms to perform quantum computations. A MIM tunnel junction is an important light source that converts electric potential energy into photons. We have worked in a low bias regime where a single electron generates a single photon. However, these junctions may also involve other fundamental processes, where a single electron may emit more photons. In fact, to generate a photon pair with one inelastic tunneling electron, the emitted photon pair

should follow $\hbar\omega_1 + \hbar\omega_2 \leq eU_{\text{bias}}$, where U_{bias} is the voltage bias, $\hbar\omega_1$ and $\hbar\omega_2$ are the photon energy corresponding to the generated photon pair. This procedure can be observed experimentally by recording intensity coincidences on two detectors. This is called photon bunching. It has been reported using a STM tip-surface junction under a DC bias[112]. In practice, it requires a relatively high voltage bias (usually $> 2.5\text{V}$) in order to observe the photon bunching in the visible to near-infrared regime. Using an antenna resonant at ω_{ant} , we expect to observe the onset of bunching at $eU = 2\hbar\omega_{\text{ant}}$. This paves the way to electrical generation of plasmons pairs, using an antenna tunnel junction in ambient environment.

Résumé

Dans cette thèse, nous étudions à la fois théoriquement et expérimentalement l'émission de plasmons polaritons de surface (SPP) par effet tunnel inélastique dans une antenne résonnante. Nous énumérons brièvement les résultats principaux chapitre par chapitre ci-dessous.

Dans le chapitre 1, nous résumons les connaissances de base sur les jonctions tunnel métal-isolant-métal (MIM) et sur l'émission de lumière par effet tunnel qui peut être décrite à l'aide de deux points de vue différents. Nous avons par ailleurs introduit le concept de nanoantenne plasmonique qui permet d'améliorer l'émission de SPP.

Dans le chapitre 2, nous détaillons la modélisation théorique de l'émission de lumière dans une jonction à effet tunnel. La première approche est basée sur le rayonnement par des fluctuations de courant qui sont déduite du théorème de fluctuation-dissipation. Nous avons montré que l'exaltation d'intensité émise est décrite par l'augmentation de champ $|K|^2$ dans la barrière. Le modèle permet de déduire l'expression explicite du rendement de conversion électron-plasmon. La seconde approche est basée sur la règle d'or de Fermi pour les effet tunnels inélastiques et met en avant la densité d'états locale et le rendement radiatif de l'antenne comme paramètres clés. Nous avons montré que les deux approches sont équivalentes en établissant le lien entre le facteur $|K|^2$ et la densité locale d'états (LDOS). Plus généralement, ce chapitre explique pourquoi une antenne peut être utilisée pour augmenter l'émission de lumière et le rendement de conversion électron-plasmon.

Dans le chapitre 3, nous avons abordé l'émission de SPP dans une configuration de microscope à effet tunnel (STM). Nous avons théoriquement démontré que l'émission de SPP peut être améliorée en utilisant un nanobâtonnet ou un nanocône entre une pointe STM et un film métallique. La principale différence avec le cas du STM est la présence d'un mode de plasmon MIM fortement localisé produisant une grande densité d'états. De plus, le mode antenne du nanobâtonnet et du nanocône est couplé au mode MIM et émet beaucoup plus efficacement. Sur le plan quantitatif, nous trouvons qu'une augmentation des émissions de SPP de deux ordres de grandeur peut être obtenue en utilisant un nanobâtonnet et une augmentation des émissions de SPP de près de trois ordres de grandeur en utilisant un nanocône.

Dans le chapitre 4, nous présentons une étude théorique de l'émission de SPP par des antennes MIM en forme de disque (nanopatch) avec un gap d'environ 1 nm. Une différence majeure avec le cas précédent (STM, nanocône, nanobâtonnet) est que le nombre de canaux électroniques est beaucoup plus grand et que, par conséquent, la puissance émise totale est beaucoup plus grande. Le principal résultat est la mise en évidence d'un mode hybride résultant du couplage fort entre un mode MIM qui apporte une contribution importante à la LDOS et un mode d'antenne capable de se coupler efficacement à des SPP. Nous avons constaté que les émissions totales de SPP peuvent être améliorées de plus de trois ordres de grandeur. De plus, nous avons montré que l'antenne émet autant de photons que de plasmons lorsque le milieu environnant est l'air. Cependant, il est possible de favoriser l'émission de plasmons de surface en augmentant l'indice optique du milieu environnant. Il est possible d'atteindre un rendement radiatif de l'émission d'un dipôle inséré au centre du disque MIM de 30% avec une épaisseur d'isolant de 1 nm à une longueur d'onde de travail d'environ 800 nm.

Dans le chapitre 5, nous décrivons le processus mis au point pour la fabrication de jonctions à effet tunnel avec des antennes nanopatch connectées électriquement. L'objectif est d'obtenir des jonctions robustes fonctionnant à la température ambiante. De plus, la fabrication d'un résonateur plasmonique exigeait un contrôle à la fois de la rugosité et de la largeur géométrique à l'échelle nanométrique. Deux types d'antenne différents, une antenne patch à bandes et une antenne patch cylindrique, ont été réalisés. Nous avons

choisi d'utiliser une barrière AlOx sur Al. L'électrode du bas en Al est déposée par photolithographie UV standard. Nous oxydons thermiquement un film mince d'Al pour générer 3 nm de couche d'AlOx à utiliser comme barrière tunnel. L'électrode en haut en Au est fabriquée par lithographie par faisceau d'électrons. Pour établir un contact électrique afin d'appliquer une tension, nous fabriquons des plots de connexion dans le plan pour la jonction de l'antenne à bande; tandis que pour la jonction cylindrique de l'antenne, nous utilisons un processus de planarisation pour fabriquer un espaceur isolant, puis nous plaçons un contact «souple» sur le dessus avec un tampon PDMS revêtu d'ITO. Nous avons obtenu une rugosité inférieure au nanomètre et nous parvenons à fabriquer une antenne patch d'une largeur de l'ordre de 100 nm sur une longueur de 60 μm avec une fluctuation de largeur inférieure à 10 nm.

Dans le chapitre 6, nous présentons les expériences sur l'émission de plasmon de surface d'antenne par effet tunnel inélastique (ASPEIT). Nous avons montré que le spectre d'émission peut être modifier en faisant varier la largeur de l'antenne. Une caractéristique importante de l'antenne est sa capacité à accroître la puissance émise et le rendement de conversion électron-plasmon. Nous démontrons que la puissance émise par ASPEIT est de l'ordre de 10 pW au lieu de quelques fW pour une jonction standard à base de STM. En termes de rendement, nous avons montré une augmentation de plus de trois ordres de grandeur par rapport à une jonction plane en utilisant ASPEIT. En utilisant le modèle développé au chapitre 2, nous reproduisons théoriquement le spectre observé, la structure de polarisation et prédisons l'augmentation de l'efficacité. Ce modèle fournit des indications pour augmenter encore l'efficacité. Malgré l'utilisation d'une antenne, le rendement de conversion photon-électron n'est que de 1.6×10^{-6} , en raison des fortes pertes de l'aluminium dans le proche infrarouge. En utilisant notre modèle, nous trouvons qu'une jonction argent / alumine / argent pourrait atteindre une efficacité de 1.4×10^{-5} photons par électron. Cela ouvre la perspective d'une source de plasmons de surface électrique efficace, ultra-rapide et très localisée.

Dans le chapitre 7, nous avons résumé les principaux résultats obtenus du chapitre 2 au chapitre 6. En outre, nous avons présenté quelques perspectives pour les travaux futurs. Tout d'abord, concernant l'émission de SPP par une jonction à antenne cylindrique 2D, nous proposons d'émettre une onde SPP cylindrique. Deuxièmement, la différence de rendement de conversion électron-plasmon décrite au chapitre 6 entre le modèle théorique et l'expérience montre la nécessité de modifier le modèle de la fonction de corrélation du courant utilisé actuellement. Troisièmement, nous proposons d'observer une éventuelle génération de paires de plasmons par une jonction d'antenne avec une tension relativement élevée ($> 2\text{V}$).

References

1. Lambe, J. and S.L. McCarthy, *Light Emission from Inelastic Electron Tunneling*. Physical Review Letters, 1976. **37**(14): p. 923-925.
2. Coombs, J., et al., *Photon emission experiments with the scanning tunnelling microscope*. Journal of Microscopy, 1988. **152**(2): p. 325-336.
3. McCarthy, S. and J. Lambe, *Enhancement of light emission from metal - insulator - metal tunnel junctions*. Applied Physics Letters, 1977. **30**(8): p. 427-429.
4. Kroo, N., Z. Szentirmay, and J. Felszerfalvi, *On the origin of light emission by tunnel junctions*. Physics Letters A, 1981. **81**(7): p. 399-401.
5. Kirtley, J., T. Theis, and J. Tsang, *Diffraction - grating - enhanced light emission from tunnel junctions*. Applied Physics Letters, 1980. **37**(5): p. 435-437.
6. Dathe, A., et al., *Electrically Excited Plasmonic Nanoruler for Biomolecule Detection*. Nano Letters, 2016. **16**(9): p. 5728-5736.
7. Parzefall, M., et al., *Antenna-coupled photon emission from hexagonal boron nitride tunnel junctions*. Nature Nanotechnology, 2015. **10**(12): p. 1058-1063.
8. Abelson, L.A. and G.L. Kerber, *Superconductor integrated circuit fabrication technology*. Proceedings of the IEEE, 2004. **92**(10): p. 1517-1533.
9. Maier, S.A., *Plasmonics: fundamentals and applications*. 2007: Springer Science & Business Media.
10. Kretschmann, E. and H. Raether, *Radiative decay of non radiative surface plasmons excited by light*. Zeitschrift für Naturforschung A, 1968. **23**(12): p. 2135-2136.
11. Raether, H., *Surface plasmons on gratings*, in *Surface plasmons on smooth and rough surfaces and on gratings*. 1988, Springer. p. 91-116.
12. Zayats, A.V., I.I. Smolyaninov, and A.A. Maradudin, *Nano-optics of surface plasmon polaritons*. Physics Reports, 2005. **408**(3-4): p. 131-314.
13. De Abajo, F.G., *Optical excitations in electron microscopy*. Reviews of Modern Physics, 2010. **82**(1): p. 209.
14. Parzefall, M., P. Bharadwaj, and L. Novotny, *Antenna-Coupled Tunnel Junctions*, in *Quantum Plasmonics*. 2017, Springer. p. 211-236.
15. Rendell, R. and D. Scalapino, *Surface plasmons confined by microstructures on tunnel junctions*. Physical Review B, 1981. **24**(6): p. 3276.
16. Rogovin, D. and D. Scalapino, *Fluctuation phenomena in tunnel junctions*. Annals of Physics, 1974. **86**(1): p. 1-90.
17. Laks, B. and D. Mills, *Photon emission from slightly roughened tunnel junctions*. Physical Review B, 1979. **20**(12): p. 4962.
18. Bharadwaj, P., A. Bouhelier, and L. Novotny, *Electrical excitation of surface plasmons*. Physical Review Letters, 2011. **106**(22): p. 226802.
19. Wang, T., et al., *Excitation of propagating surface plasmons with a scanning tunnelling microscope*. Nanotechnology, 2011. **22**(17): p. 175201.
20. Drezet, A., et al., *Leakage radiation microscopy of surface plasmon polaritons*. Materials Science and Engineering: B, 2008. **149**(3): p. 220-229.
21. Rossel, F., M. Pivetta, and W.-D. Schneider, *Luminescence experiments on supported molecules with the scanning tunneling microscope*. Surface Science Reports, 2010. **65**(5): p. 129-144.
22. Berndt, R., et al., *Photon emission at molecular resolution induced by a scanning tunneling microscope*. Science, 1993. **262**(5138): p. 1425-1427.
23. Du, W., et al., *Highly efficient on-chip direct electronic-plasmonic transducers*. Nature Photonics, 2017. **11**(10): p. 623.
24. Zeman, E.J. and G.C. Schatz, *An accurate electromagnetic theory study of surface enhancement factors for silver, gold, copper, lithium, sodium, aluminum, gallium, indium, zinc, and cadmium*. Journal of Physical Chemistry, 1987. **91**(3): p. 634-643.
25. Malitson, I.H., *Refraction and Dispersion of Synthetic Sapphire*. Journal of the Optical Society of America, 1962. **52**(12): p. 1377-1379.

References

26. Kern, J., et al., *Electrically driven optical antennas*. Nature Photonics, 2015. **9**(9): p. 582.
27. Kelly, K.L., et al., *The optical properties of metal nanoparticles: the influence of size, shape, and dielectric environment*. 2003, ACS Publications.
28. Miller, M.M. and A.A. Lazarides, *Sensitivity of metal nanoparticle surface plasmon resonance to the dielectric environment*. The Journal of Physical Chemistry B, 2005. **109**(46): p. 21556-21565.
29. Novotny, L. and B. Hecht, *Principles of nano-optics*. 2012: Cambridge university press. 2nd edition.
30. Nerkararyan, K.V., *Superfocusing of a surface polariton in a wedge-like structure*. Physics Letters A, 1997. **237**(1-2): p. 103-105.
31. Novotny, L. and N. Van Hulst, *Antennas for light*. Nature Photonics, 2011. **5**(2): p. 83.
32. Qian, H., et al., *Efficient light generation from enhanced inelastic electron tunnelling*. Nature Photonics, 2018. **12**: p. 485-488.
33. Gurunaryanan, S.P., et al., *Electrically driven unidirectional optical nanoantennas*. Nano Letters, 2017. **17**(12): p. 7433-7439.
34. Février, P. and J. Gabelli, *Tunneling time probed by quantum shot noise*. Nature Communications, 2018. **9**(1): p. 4940.
35. Hone, D., B. Mühlischlegel, and D. Scalapino, *Theory of light emission from small particle tunnel junctions*. Applied Physics Letters, 1978. **33**(2): p. 203-204.
36. Lee, H. and L. Levitov, *Current fluctuations in a single tunnel junction*. Physical Review B, 1996. **53**(11): p. 7383.
37. Roussel, B., P. Degiovanni, and I. Safi, *Perturbative fluctuation dissipation relation for nonequilibrium finite-frequency noise in quantum circuits*. Physical Review B, 2016. **93**(4): p. 045102.
38. Bigourdan, F., et al., *Nanoantenna for Electrical Generation of Surface Plasmon Polaritons*. Physical Review Letters, 2016. **116**(10): p. 106803.
39. Persson, B. and A. Baratoff, *Theory of photon emission in electron tunneling to metallic particles*. Physical Review Letters, 1992. **68**(21): p. 3224.
40. Simmons, J.G., *Electric tunnel effect between dissimilar electrodes separated by a thin insulating film*. Journal of Applied Physics, 1963. **34**(9): p. 2581-2590.
41. Simmons, J.G., *Generalized formula for the electric tunnel effect between similar electrodes separated by a thin insulating film*. Journal of Applied Physics, 1963. **34**(6): p. 1793-1803.
42. Staelin, D.H., A.W. Morgenthaler, and J.A. Kong, *Electromagnetic waves*. 1994: Pearson Education India.
43. Stipe, B.C., M.A. Rezaei, and W. Ho, *Single-Molecule Vibrational Spectroscopy and Microscopy*. Science, 1998. **280**(5370): p. 1732.
44. Xu, C., et al., *Nature of Asymmetry in the Vibrational Line Shape of Single-Molecule Inelastic Electron Tunneling Spectroscopy with the STM*. Physical Review Letters, 2016. **116**(16): p. 166101.
45. Berndt, R., J.K. Gimzewski, and P. Johansson, *Inelastic tunneling excitation of tip-induced plasmon modes on noble-metal surfaces*. Physical Review Letters, 1991. **67**(27): p. 3796-3799.
46. Johansson, P., R. Monreal, and P. Apell, *Theory for light emission from a scanning tunneling microscope*. Physical Review B, 1990. **42**(14): p. 9210.
47. Anger, P., P. Bharadwaj, and L. Novotny, *Enhancement and quenching of single-molecule fluorescence*. Physical Review Letters, 2006. **96**(11): p. 113002.
48. Bigourdan, F., J.-P. Hugonin, and P. Lalanne, *Aperiodic-Fourier modal method for analysis of body-of-revolution photonic structures*. JOSA A, 2014. **31**(6): p. 1303-1311.
49. Yang, J., J.-P. Hugonin, and P. Lalanne, *Near-to-Far Field Transformations for Radiative and Guided Waves*. ACS Photonics, 2016. **3**(3): p. 395-402.
50. Snyder, A.W. and J. Love, *Optical waveguide theory*. 2012: Springer Science & Business Media.
51. Lozan, O., et al., *Anomalous Light Absorption around Subwavelength Apertures in Metal Films*. Physical Review Letters, 2014. **112**(19): p. 193903.
52. Smith, D., et al., *Handbook of optical constants of solids*. Handbook of Optical Constants of Solids, 1985. **1**: p. 369-406.
53. Vial, A., et al., *Improved analytical fit of gold dispersion: Application to the modeling of extinction spectra with a finite-difference time-domain method*. Physical Review B, 2005. **71**(8): p. 085416.
54. Bohren, C.F. and D.R. Huffman, *Absorption and scattering of light by small particles*. 2008: John Wiley & Sons.

References

55. Faggiani, R.M., J. Yang, and P. Lalanne, *Quenching, plasmonic, and radiative decays in nanogap emitting devices*. ACS photonics, 2015. **2**(12): p. 1739-1744.
56. Chen, X.-W., M. Agio, and V. Sandoghdar, *Metalldielectric Hybrid Antennas for Ultrastrong Enhancement of Spontaneous Emission*. Physical Review Letters, 2012. **108**(23): p. 233001.
57. Matsuzaki, K., et al., *Strong plasmonic enhancement of biexciton emission: controlled coupling of a single quantum dot to a gold nanocone antenna*. Scientific Reports, 2017. **7**: p. 42307.
58. Belacel, C., et al., *Controlling Spontaneous Emission with Plasmonic Optical Patch Antennas*. Nano Letters, 2013. **13**(4): p. 1516-1521.
59. Rose, A., et al., *Control of Radiative Processes Using Tunable Plasmonic Nanopatch Antennas*. Nano Letters, 2014. **14**(8): p. 4797-4802.
60. Thang B. Hoang, G.M., et al., *Ultrafast Room-temperature single photon emission from quantum dots coupled to plasmonic nanocavities*. Nano Letters, 2016. **16**(1): p. 270-275.
61. Akselrod, G.M., et al., *Probing the mechanisms of large Purcell enhancement in plasmonic nanoantennas*. Nature Photonics, 2014. **8**(11): p. 835.
62. Sauvan, C., et al., *Theory of the Spontaneous Optical Emission of Nanosize Photonic and Plasmon Resonators*. Physical Review Letters, 2013. **110**(23): p. 237401.
63. Olmon, R.L., et al., *Optical dielectric function of gold*. Physical Review B, 2012. **86**(23): p. 235147.
64. Tserkezis, C., et al., *Hybridization of plasmonic antenna and cavity modes: Extreme optics of nanoparticle-on-mirror nanogaps*. Physical Review A, 2015. **92**(5): p. 053811.
65. Choo, H., et al., *Nanofocusing in a metal-insulator-metal gap plasmon waveguide with a three-dimensional linear taper*. Nature Photonics, 2012. **6**(12): p. 838.
66. Kurokawa, Y. and H.T. Miyazaki, *Metal-insulator-metal plasmon nanocavities: Analysis of optical properties*. Physical Review B, 2007. **75**(3): p. 035411.
67. Bozhevolnyi, S.I. and T. Søndergaard, *General properties of slow-plasmon resonant nanostructures: nano-antennas and resonators*. Optics express, 2007. **15**(17): p. 10869-10877.
68. Yang, J., et al., *Ultras-small metal-insulator-metal nanoresonators: impact of slow-wave effects on the quality factor*. Optics Express, 2012. **20**(15): p. 16880-16891.
69. Lalanne, P., et al., *Light interaction with photonic and plasmonic resonances*. Laser & Photonics Reviews, 2018. **12**(5): p. 1700113.
70. Yan, W., R. Faggiani, and P. Lalanne, *Rigorous modal analysis of plasmonic nanoresonators*. Physical Review B, 2018. **97**(20): p. 205422.
71. Gerard, J.-M., *Solid-state cavity-quantum electrodynamics with self-assembled quantum dots*, in *Single Quantum Dots*. 2003, Springer. p. 269-314.
72. Kiraz, A., M. Atatüre, and A. Imamoglu, *Quantum-dot single-photon sources: Prospects for applications in linear optics quantum-information processing*. Physical Review A, 2004. **69**(3): p. 032305.
73. Hoang, T.B., et al., *Ultrafast spontaneous emission source using plasmonic nanoantennas*. Nature communications, 2015. **6**: p. 7788.
74. Adato, R., et al., *Engineered Absorption Enhancement and Induced Transparency in Coupled Molecular and Plasmonic Resonator Systems*. Nano Letters, 2013. **13**(6): p. 2584-2591.
75. Mahapatro, A.K., et al., *Gold surface with sub-nm roughness realized by evaporation on a molecular adhesion monolayer*. Applied Physics Letters, 2006. **88**(15): p. 151917.
76. Du, W., et al., *On-chip molecular electronic plasmon sources based on self-assembled monolayer tunnel junctions*. Nature Photonics, 2016. **10**(4): p. 274.
77. Hass, G. and J.E. Waylonis, *Optical Constants and Reflectance and Transmittance of Evaporated Aluminum in the Visible and Ultraviolet**. Journal of the Optical Society of America, 1961. **51**(7): p. 719-722.
78. Gloos, K., P. Koppinen, and J. Pekola, *Properties of native ultrathin aluminium oxide tunnel barriers*. Journal of Physics: Condensed Matter, 2003. **15**(10): p. 1733.
79. Lin, H., et al., *Thermal and Electrical Conduction in Ultrathin Metallic Films: 7 nm down to Sub - Nanometer Thickness*. Small, 2013. **9**(15): p. 2585-2594.
80. Dathe, A., et al., *Electrically Excited Plasmonic Nanoruler for Biomolecule Detection*. Nano Letters, 2016. **16**(9): p. 5728-5736.
81. Parzefall, M., et al., *Light from Van der Waals quantum tunneling devices*. arXiv preprint arXiv:1804.06163, 2018.

References

82. Chia, A. and R. LaPierre, *Contact planarization of ensemble nanowires*. Nanotechnology, 2011. **22**(24): p. 245304.
83. Ng, H.T., et al., *Single crystal nanowire vertical surround-gate field-effect transistor*. Nano Letters, 2004. **4**(7): p. 1247-1252.
84. Persson, K.-M., et al., *Extrinsic and intrinsic performance of vertical InAs nanowire MOSFETs on Si substrates*. IEEE Transactions on Electron Devices, 2013. **60**(9): p. 2761-2767.
85. Choi, S., et al., *Comparative study of thermally cured and electron-beam-exposed hydrogen silsesquioxane resists*. Journal of Vacuum Science & Technology B: Microelectronics and Nanometer Structures Processing, Measurement, and Phenomena, 2008. **26**(5): p. 1654-1659.
86. Penaud, J., F. Fruleux, and E. Dubois, *Transformation of hydrogen silsesquioxane properties with RIE plasma treatment for advanced multiple-gate MOSFETs*. Applied surface science, 2006. **253**(1): p. 395-399.
87. Lee, S.H. and J.-Q. Lu, *Nano-ring-shape growth of fluorocarbon macromolecules during SiO₂ etching*. Nanotechnology, 2010. **21**(15): p. 155303.
88. Li, G., et al., *Efficient inverted polymer solar cells*. Applied Physics Letters, 2006. **88**(25): p. 253503.
89. Tang, C.W. and S.A. VanSlyke, *Organic electroluminescent diodes*. Applied physics letters, 1987. **51**(12): p. 913-915.
90. Zhao, L., et al., *Indium tin oxide thin films by bias magnetron rf sputtering for heterojunction solar cells application*. Applied Surface Science, 2005. **252**(2): p. 385-392.
91. Qin, D., Y. Xia, and G.M. Whitesides, *Soft lithography for micro-and nanoscale patterning*. Nature protocols, 2010. **5**(3): p. 491.
92. McDonald, J.C. and G.M. Whitesides, *Poly (dimethylsiloxane) as a material for fabricating microfluidic devices*. Accounts of chemical research, 2002. **35**(7): p. 491-499.
93. Wang, P., et al., *Reactive tunnel junctions in electrically driven plasmonic nanorod metamaterials*. Nature nanotechnology, 2018. **13**(2): p. 159.
94. Wang, Z., A.A. Volinsky, and N.D. Gallant, *Crosslinking effect on polydimethylsiloxane elastic modulus measured by custom - built compression instrument*. Journal of Applied Polymer Science, 2014. **131**(22).
95. Fan, P., et al., *An electrically-driven GaAs nanowire surface plasmon source*. Nano letters, 2012. **12**(9): p. 4943-4947.
96. Koller, D., et al., *Organic plasmon-emitting diode*. Nature Photonics, 2008. **2**(11): p. 684.
97. Huang, K.C., et al., *Electrically driven subwavelength optical nanocircuits*. Nature Photonics, 2014. **8**(3): p. 244.
98. Neutens, P., et al., *Electrical excitation of confined surface plasmon polaritons in metallic slot waveguides*. Nano letters, 2010. **10**(4): p. 1429-1432.
99. Büttiker, M. and R. Landauer, *Traversal time for tunneling*. Physical Review Letters, 1982. **49**(23): p. 1739.
100. Zhang, Y., et al., *Edge scattering of surface plasmons excited by scanning tunneling microscopy*. Optics express, 2013. **21**(12): p. 13938-13948.
101. Muehlschlegel, P., et al., *Resonant optical antennas*. science, 2005. **308**(5728): p. 1607-1609.
102. Biagioni, P., J.-S. Huang, and B. Hecht, *Nanoantennas for visible and infrared radiation*. Reports on Progress in Physics, 2012. **75**(2): p. 024402.
103. Curto, A.G., et al., *Unidirectional emission of a quantum dot coupled to a nanoantenna*. Science, 2010. **329**(5994): p. 930-933.
104. Yang, J., R. Faggiani, and P. Lalanne, *Light emission in nanogaps: overcoming quenching*. Nanoscale Horizons, 2016. **1**(1): p. 11-13.
105. Grabert, H. and M.H. Devoret, *Single charge tunneling: Coulomb blockade phenomena in nanostructures*. Vol. 294. 2013: Springer Science & Business Media.
106. Groner, M., et al., *Electrical characterization of thin Al₂O₃ films grown by atomic layer deposition on silicon and various metal substrates*. Thin Solid Films, 2002. **413**(1-2): p. 186-197.
107. Kirtley, J., T. Theis, and J. Tsang, *Light emission from tunnel junctions on gratings*. Physical Review B, 1981. **24**(10): p. 5650.
108. McPeak, K.M., et al., *Plasmonic films can easily be better: rules and recipes*. ACS photonics, 2015. **2**(3): p. 326-333.
109. Bai, Q., et al., *Efficient and intuitive method for the analysis of light scattering by a resonant nanostructure*. Optics express, 2013. **21**(22): p. 27371-27382.

References

110. Aizpurua, J., S.P. Apell, and R. Berndt, *Role of tip shape in light emission from the scanning tunneling microscope*. Physical Review B, 2000. **62**(3): p. 2065.
111. Kirtley, J., et al., *Hot-electron picture of light emission from tunnel junctions*. Physical Review B, 1983. **27**(8): p. 4601.
112. Leon, C., et al., *Photon super-bunching from a generic tunnel junction*. arXiv preprint arXiv:1805.10234, 2018.

Titre : Excitation électrique de plasmons polaritons de surface par effet tunnel inélastique avec des nanoantennes résonnantes

Mots clés : plasmons polaritons de surface, Excitation électrique, nanoantennes résonnantes, électrons inélastiques à effet tunnel, fluctuations du courant

Résumé : L'excitation électrique des plasmons polaritons de surface par effet tunnel inélastique peut être ultrarapide et localisée, ce qui permet de développer une nanosource pour la nanophotonique intégrée. Pourtant, ce processus est très inefficace avec un rendement de conversion typique de 10^{-7} ~ 10^{-5} plasmon par électron. Dans ce manuscrit de thèse, nous présentons une étude théorique et expérimentale qui vise à augmenter l'émission de plasmons de surface par effet tunnel inélastique avec une nanoantenne résonnante. Nous avons développé un modèle

théorique pour décrire l'émission de lumière à partir d'une jonction à effet tunnel en utilisant le théorème de fluctuation-dissipation. Nous proposons deux stratégies pour augmenter le rendement de conversion électron-plasmon. Nous avons développé les processus de fabrication pour réaliser les antennes à effet tunnel en utilisant la configuration Al/AIOx/Au. Nous montrons l'antenne permet de contrôler le spectre d'émission SPP, la polarisation d'émission SPP et renforcer l'efficacité des émissions de SPP de plus de 3 ordres de grandeur.

Title : Electrical excitation of surface plasmon polaritons by inelastic tunneling electrons with resonant nanoantennas

Keywords : Electrical excitation, surface plasmon polaritons, inelastic tunneling, current fluctuations, resonant nanoantennas

Abstract: Electrical excitation of surface plasmon polaritons by inelastic tunneling electrons has the potential to be fast and localized so that it offers the opportunity to develop a nanosource for on-chip nanophotonics. However, inelastic tunneling is rather inefficient with a typical electron-to-plasmon conversion efficiency of 10^{-7} ~ 10^{-5} . In this thesis manuscript, we present a study for enhancing surface plasmon emission by inelastic tunneling electrons with a resonant nanoantenna. It consists of theoretical and experimental investigations. First, we have developed a theoretical model

to describe the light emission from a tunnel junction based on the fluctuation-dissipation theorem. Second, we have theoretically demonstrated two strategies to improve the antenna SPP efficiency thus aiming to enhance electron-to-plasmon conversion efficiency. Third, we have developed the fabrication procedures to realize antenna tunnel junctions based on the Al/AIOx/Au configuration. The antenna junction is demonstrated to control the SPP emission spectrum, the SPP emission polarization and enhance the SPP emission efficiency by over 3 orders of magnitude.

